

ARMY RESEARCH LABORATORY



**A Visual Library of Stability in Binary Metallic Systems:
The Stabilization of Nanocrystalline Grain Size by Solute
Addition: Part 1**

by Mark A. Atwater and Kris A. Darling

ARL-TR-6007

May 2012

NOTICES

Disclaimers

The findings in this report are not to be construed as an official Department of the Army position unless so designated by other authorized documents.

Citation of manufacturer's or trade names does not constitute an official endorsement or approval of the use thereof.

Destroy this report when it is no longer needed. Do not return it to the originator.

Army Research Laboratory

Aberdeen Proving Ground, MD 21005-5069

ARL-TR-6007

May 2012

A Visual Library of Stability in Binary Metallic Systems: The Stabilization of Nanocrystalline Grain Size by Solute Addition: Part 1

**Mark A. Atwater and Kris A. Darling
Weapons and Materials Research Directorate, ARL**

REPORT DOCUMENTATION PAGE				Form Approved OMB No. 0704-0188	
<p>Public reporting burden for this collection of information is estimated to average 1 hour per response, including the time for reviewing instructions, searching existing data sources, gathering and maintaining the data needed, and completing and reviewing the collection information. Send comments regarding this burden estimate or any other aspect of this collection of information, including suggestions for reducing the burden, to Department of Defense, Washington Headquarters Services, Directorate for Information Operations and Reports (0704-0188), 1215 Jefferson Davis Highway, Suite 1204, Arlington, VA 22202-4302. Respondents should be aware that notwithstanding any other provision of law, no person shall be subject to any penalty for failing to comply with a collection of information if it does not display a currently valid OMB control number.</p> <p>PLEASE DO NOT RETURN YOUR FORM TO THE ABOVE ADDRESS.</p>					
1. REPORT DATE (DD-MM-YYYY)	2. REPORT TYPE		3. DATES COVERED (From - To)		
May 2012	Final		February 2012–September 2012		
4. TITLE AND SUBTITLE					
A Visual Library of Stability in Binary Metallic Systems: The Stabilization of Nanocrystalline Grain Size by Solute Addition: Part 1					
6. AUTHOR(S)					
Mark A. Atwater and Kris A. Darling					
7. PERFORMING ORGANIZATION NAME(S) AND ADDRESS(ES)					
U.S. Army Research Laboratory ATTN: RDRL-WMM-F Aberdeen Proving Ground, MD 21005-5069					
9. SPONSORING/MONITORING AGENCY NAME(S) AND ADDRESS(ES)					
10. SPONSOR/MONITOR'S ACRONYM(S)					
11. SPONSOR/MONITOR'S REPORT NUMBER(S)					
12. DISTRIBUTION/AVAILABILITY STATEMENT					
Approved for public release; distribution is unlimited.					
13. SUPPLEMENTARY NOTES					
14. ABSTRACT					
In part 1, a visual library is reported for predicting stabilization in nanocrystalline binary alloys. A free energy model for grain boundary segregation and grain size stability has been applied for assessing the stability in 2288 distinct binary systems. The model incorporates accessible information that allows a more universal application. For each alloy pair, the values for elastic enthalpy, mixing enthalpy, minimum normalized grain-boundary energy, and the boundary concentration at the free energy minimum are reported. This data is presented in a periodic table format for each base solvent, where the pertinent parameters are reported numerically, and by color-coding to facilitate quick identification of stable alloys. The free energy of each system is dependent on the solvent, grain size, solute content, and temperature. In forthcoming work (part 2), the stabilization behavior of select alloys will be experimentally compared to the predictions reported here.					
15. SUBJECT TERMS					
nanocrystalline, thermodynamic stabilization, enthalpy, entropy, grain size, solute, boundary energy, periodic table, binary, visual library					
16. SECURITY CLASSIFICATION OF:		17. LIMITATION OF ABSTRACT	18. NUMBER OF PAGES	19a. NAME OF RESPONSIBLE PERSON	
a. REPORT Unclassified	b. ABSTRACT Unclassified	c. THIS PAGE Unclassified	UU	80	Mark Atwater
					19b. TELEPHONE NUMBER (Include area code) 410-306-0862

Contents

List of Figures	iv
List of Tables	vi
Acknowledgments	vii
1. Introduction	1
2. Grain Growth and Stability	1
3. Preface to the Visual Library: Appendix	4
4. Influence of Variables	5
5. Conclusions	18
6. References	19
Appendix. Solvent Stability Tables	21
List of Symbols, Abbreviations, and Acronyms	67
Distribution List	69

List of Figures

Figure 1. Explanation of tabulated data.	6
Figure 2. Desirable characteristics for stabilization.....	7
Figure 3. Explanation of comparisons. (See text for descriptions of symbols).	10
Figure 4. The variation of normalized grain boundary energy as a function of grain size for (a) Cu-Ti, (b) Cu-Zr, and (c) Cu-Hf. All variables are listed in the legend.	11
Figure 5. The variation of normalized grain boundary energy as a function of grain size for (a) Cu-V, (b) Cu-Nb, and (c) Cu-Ta. All variables are listed in the legend.	12
Figure 6. The variation of normalized grain boundary energy as a function of solute concentration for (a) Cu-Ti, (b) Cu-Zr, and (c) Cu-Hf. All variables are listed in the legend.	14
Figure 7. The variation of normalized grain boundary energy as a function of solute concentration for (a) Cu-V, (b) Cu-Nb, and (c) Cu-Ta. All variables are listed in the legend.	15
Figure 8. The variation of normalized grain boundary energy as a function of temperature for (a) Cu-Ti, (b) Cu-Zr, and (c) Cu-Hf. All variables are listed in the legend.	16
Figure 9. The variation of normalized grain boundary energy as a function of temperature for (a) Cu-V, (b) Cu-Nb, and (c) Cu-Ta. All variables are listed in the legend.	17
Figure A-1. Lithium.	23
Figure A-2. Beryllium.	24
Figure A-3. Boron.	25
Figure A-4. Sodium.	26
Figure A-5. Magnesium.	27
Figure A-6. Aluminum.	28
Figure A-7. Potassium.	29
Figure A-8. Calcium.	30
Figure A-9. Scandium.	31
Figure A-10. Titanium.	32
Figure A-11. Vanadium.	33
Figure A-12. Chromium.	34
Figure A-13. Manganese.	35
Figure A-14. Iron.	36
Figure A-15. Cobalt.	37
Figure A-16. Nickel.	38

Figure A-17. Copper.....	39
Figure A-18. Zinc.....	40
Figure A-19. Rubidium.....	41
Figure A-20. Strontium.....	42
Figure A-21. Yttrium.....	43
Figure A-22. Zirconium.....	44
Figure A-23. Niobium.....	45
Figure A-24. Molybdenum.....	46
Figure A-25. Ruthenium.....	47
Figure A-26. Rhodium.....	48
Figure A-27. Palladium.....	49
Figure A-28. Silver.....	50
Figure A-29. Cadmium.....	51
Figure A-30. Indium.....	52
Figure A-31. Tin.....	53
Figure A-32. Barium.....	54
Figure A-33. Hafnium.....	55
Figure A-34. Tantalum.....	56
Figure A-35. Tungsten.....	57
Figure A-36. Rhenium.....	58
Figure A-37. Osmium.....	59
Figure A-38. Iridium.....	60
Figure A-39. Platinum.....	61
Figure A-40. Gold.....	62
Figure A-41. Thallium.....	63
Figure A-42. Lead.....	64
Figure A-43. Thorium.....	65
Figure A-44. Uranium.....	66

List of Tables

Table 1. General data pertaining to the Cu alloy systems discussed. The solubility limit assumes Cu as the solvent. A zero value indicates negligible solubility with no equilibrium value listed in the phase diagram. Enthalpies are calculated with Cu as the solvent.....	9
---	---

Acknowledgments

The authors would like to thank the following for intellectual conversations on the reported topic:

- Brian VanLeeuwen, Pennsylvania State University
- Professor Ronald Scattergood, North Carolina State University
- Professor Carl Koch, North Carolina State University

INTENTIONALLY LEFT BLANK.

1. Introduction

In recent years, nanocrystalline metals and alloys have captured the attention of the scientific community, primarily due to the intriguing mechanical properties with which they are associated. Numerous reports now indicate that an order of magnitude increase in strength is possible in metals and alloys that exhibit grain sizes approaching the lower limit of nanocrystallinity (1–4). While achieving high strength has never been a problem, the ability to achieve any amount of uniform elongation, the prerequisite for appreciable ductility, has been a challenge in the past (5–7). Recently, numerous reports of improved ductility indicate that 10s of percent of elongation may be possible in nanocrystalline metals (8–10). The combined possibility of ultra-high strength and improved ductility make nanocrystalline metals and alloys the future of advanced metallurgy.

There are several methods for producing nanocrystalline (<100-nm grain size) metals and alloys; however, none produces samples suitable for bulk mechanical applications. Many methods, such as mechanical milling techniques, can produce metallic particulates (average diameter of 10–100 μm) with an internal nanocrystalline microstructure <50 nm. The most convenient way to consolidate the metal particles is through powder metallurgy techniques such as sintering. Sintering allows the production of useful parts of almost limitless geometry. However, since this method involves the application of heat and pressure, the microstructure of nanocrystalline metals that gives rise to the advanced physical properties is in jeopardy of coarsening and weakening. Thus, the technological aspects of the thermal stability in nanocrystalline materials must be realized if steps are to be made toward large-scale applications.

2. Grain Growth and Stability

Conceptually, the perturbations between grains in a polycrystal, also known as grain boundaries, are regions of disturbed lattice only a few atomic diameters wide, and generally account for an insignificant fraction of the microstructure. As the grain size decreases below 10 nm in a nanocrystalline material, the percentage of microstructure constituted by grain boundaries increases, and can be in excess of 50%. Thus, grain boundaries in nanocrystalline materials can account for a large increase of the total free energy of the system. The reduction of this excess free energy, via the removal of grain boundary area, represents a large driving force for grain growth. The driving pressure, P , for grain growth, based on the expansion of a curved interface, is (11):

$$P = \frac{C\gamma_b}{r} , \quad (1)$$

where C is a constant, γ_b is the grain boundary free energy per unit area, and r is the radius of the curvature of a grain, which is proportional to the grain size. When r is in the range of several nanometers, the driving pressure for grain growth is large (~ 0.5 GPa). It has been demonstrated that pure nanocrystalline metals (Al, Sn, Pb, Zn, and Mg [12–14]) exhibit extensive grain growth at room temperature. Metals with higher melting points, such as Co, Ni, and Fe, are not exceptions to this phenomenon and show rapid grain growth over moderate temperature ranges (220–450 °C), resulting in grain sizes in the micron range at $\sim 50\%$ of their respective melting temperatures (15–17). It is this thermal instability that limits the overall processing and applications of nanocrystalline metals and alloys. Therefore, it becomes imperative to create alloys that are resistant to grain growth at elevated temperatures.

The thermal stability of these microstructures is essential for adopting nanocrystalline materials in commercial processes and applications. A number of investigations on the thermal stability of nanocrystalline materials have been conducted based on controlling the parameters for the velocity, v , of a grain boundary undergoing curvature-driven grain growth (18, 19):

$$v = MP = M_o \exp\left[\frac{-Q_m}{RT}\right] \frac{2\gamma_b}{r} , \quad (2)$$

where M is the mobility, M_o is the pre-exponential factor for the mobility term, Q_m is the activation energy for grain boundary mobility, R is the ideal gas constant, and T is the absolute temperature. The pressure is entirely curvature-driven and therefore related to γ_b , the interfacial energy per unit area, and the radius r of the grain. There are generally two approaches used to reduce the velocity of a moving grain boundary—modifying either the kinetic parameter (M) or the driving force (P), the latter containing the thermodynamic parameter (γ_b).

Reduction in grain boundary mobility has been successful experimentally; however, because mobility follows the Arrhenius law, the pinning pressure on grain boundaries by any obstacles will eventually be overcome with the application of enough thermal energy (1). A more promising approach could be to modify the thermodynamic parameter in the pressure term (γ_b), which shows only a slight temperature dependence (20).

The grain boundary energy can be calculated by solving the Gibbs adsorption equation in the dilute limit to yield the following (21, 22):

$$\gamma = \gamma_b + \Gamma \left[\Delta H_{seg} - T \Delta S_{seg} \right] , \quad (3)$$

where γ_b is the interfacial energy of the solvent, Γ_s is the specific solute excess at the interface, T is the absolute temperature, and ΔH_{seg} and ΔS_{seg} are the change in enthalpy and entropy by solute segregation, respectively. ΔH_{seg} consists of chemical (ΔH_{chem} , as described by Defay et al. [23]) and elastic (ΔH_{el} , as described by McLean [24]) terms that were combined by Wynblatt and Ku in accounting for surface segregation [25, 26]. The enthalpy of segregation is given in the original Wynblatt-Ku model [25] as $\Delta H_{seg} = \Delta H_{chem} + \Delta H_{el}$, where the chemical contribution is given by

$$\Delta H_{chem} = (\gamma_A - \gamma_B)\sigma + 2\omega \left[z_{in} \left(X_A^b - X_A^s \right) + z_{out} \left(X_A^b - \frac{1}{2} \right) \right], \quad (4)$$

where γ_A and γ_B are the surface energies for the solute and solvent, respectively; X_A^b and X_A^s are the atom fraction segregant of solute in the bulk and surface, respectively; σ is the surface area per mole; ω is the regular solution parameter; and z_{in} and z_{out} are the in-plane and half-of-the-out-of-plane bonds of an atom in the surface plane. The regular solution parameter is given by

$$\omega = \varepsilon_{AB} - \frac{1}{2}(\varepsilon_{AA} - \varepsilon_{BB}) = \frac{\Delta H_m}{ZX_A^b X_B^b}, \quad (5)$$

where the bond energies between atoms of the solute, A , and the solvent, B , are given by the corresponding ε values, ΔH_m is the enthalpy of mixing; and Z is the coordination number ($Z = z_{in} + 2z_{out}$). The elastic enthalpy is (27)

$$\Delta H_{el} = -\Delta E_{el} = -\frac{2K_B G_A (V_B - V_A)^2}{3K_B V_A + 4G_A V_B}, \quad (6)$$

where ΔE_{el} is the change in elastic energy, K is the bulk modulus, G is the shear modulus, and V is the molar volume.

A new thermodynamic stabilization model has been developed [28] using the Wynblatt-Ku model as its basis. This modified approach better accounts for grain boundary segregation where some bonding across the boundary exists and also accounts for mass balance. The formula is fully derived by VanLeeuwen et al. [28] and the reader is directed there for a more in-depth treatment. Here we provide the most pertinent equations. The free energy change due to solute segregation to a grain boundary can be expressed by

$$\Delta G_{seg} = (\gamma_A - \gamma_B)(1-\alpha)\sigma - \frac{8\Delta H_m}{Z} \left[z_{in} \left(X_A^s - X_A^b \right) - z_{out} \left[\left(X_A^b - \frac{1}{2} \right) - \alpha \left(X_A^s - \frac{1}{2} \right) \right] \right] + \Delta H_{el} - RT \ln \left[\frac{X_A^b (1-X_A^s)}{X_A^s (1-X_A^b)} \right], \quad (7)$$

where $\alpha = 5/6$ to account for cross-boundary bonding, X_A^b and X_A^s represent the bulk and grain boundary concentrations of the solute, respectively, and ΔH_m is the enthalpy of mixing of an equimolar liquid of A and B. The last term in equation 7 is the entropy of segregation, which can be represented by ΔS_{seg} . Given that $\Delta G_{seg} = \Delta H_{seg} - T\Delta S_{seg}$, rearranging of equation 3 gives the normalized grain boundary energy as

$$\frac{\gamma}{\gamma_b} = 1 + \Gamma_s \frac{\Delta G_{seg}}{\gamma_b}, \quad (8)$$

where the grain boundary surface excess for the bilayer model is given by $\Gamma_s = 2(X_A^s - X_A^b)/\sigma$, and the interfacial energy for a grain boundary, γ_b , can be estimated as one-third the solvent surface energy (29). The grain boundary energy is based on the *pure* solvent, not for the mixture, as the alloy is assumed to be dilute and strongly segregating. Alloys for which these two assumptions are not satisfied may deviate from the predicted behavior.

Results for the grain size stability as a function of temperature and total solute content requires a mass balance equation such that the bulk concentration of solute is given by

$$X_A^b = \frac{\frac{6(V_b)^{\frac{1}{3}}}{d} X_A^s - X_o}{\frac{6(V_b)^{\frac{1}{3}}}{d} - 1}, \quad (9)$$

where X_o is the global solute content (bulk and boundary concentrations together) and d is the grain size. Equation 9 can be substituted into equation 7 to calculate the free energy as a function of total solute concentration, grain size, and temperature, making it a powerful tool for predicting the microstructural stability of a nanocrystalline metal.

This resulting equation is particularly useful considering its use of readily available elemental data. Information such as surface energy, atomic volume, and elastic moduli are tabulated in literature. The mixing enthalpy is also tabulated for nearly every element pair by Takeuchi and Inoue (30), using Miedema's model (31). The simplicity of the analysis makes it quite user-friendly, but it imposes certain limitations as well. These include application to dilute solutions, strongly segregating mixtures, and those with negligible solubility throughout the annealing range. Therefore, this treatment must be judiciously applied. It is of great value to consult phase diagrams for alloys before deciding on an element pair because the model assumes segregation to grain boundaries, which will be weak in highly miscible systems. This is commonly accounted for in the elastic enthalpy term but should not be taken for granted.

3. Preface to the Visual Library: Appendix

A comprehensive library (see the appendix) was developed to display the stabilization capabilities of 44 solvents, each with 52 possible solutes, for a total of 2288 combinations. Some elements were limited to use as solutes due to complex crystal structure, incomplete structural or physical data, or impracticality as a realistic solvent (i.e., Hg). The model has been found to agree qualitatively with a variety of experimental findings in literature for the following systems:

Fe-Ta (32), Fe-Zr (32), Fe-Ni (32), Fe-Cr (33), Fe-Ti (34), Cu-Nb (35, 36), Cu-Ta (37), Cu-Zr (38), Ni-W (39, 40), and Pd-Zr (41).

The data presented in the appendix table section is dense, with a variety of informational boxes present for each atom pair (see figure 1 for explanation of the tables). The solute is indicated in the large box at the top of the periodic table. The variables of grain size, global solute content, and temperature are located in the yellow box to the right of the solvent. The values for these variables are 30 nm, 0.010 solute fraction (1%), and 273 K, respectively. In section 4 there is a demonstration of the effect of changing these values for Cu alloyed with group IV and group V elements. When viewing the tables, note that more-intense colors indicate better stabilization tendencies except for mixing enthalpy. A dark-green bottom left corner is the most important indicator, as zero grain boundary energy is the hallmark of stability. The criteria for stability are presented in context in figure 2.

4. Influence of Variables

The intention of this model is to provide a practical approach for calculating the reduction in grain boundary energy to assess possible solutes for stabilizing nanocrystalline alloys. The approach presented in this work should provide a qualitative method of selecting grain growth inhibiting solutes while still being relatively easy to apply. To evaluate the applicability of this model to a specific problem or system, it may be useful to consider the phenomena it captures and those it neglects.

This model captures the following:

- boundary energy reduction upon segregation (equation 3)
- chemical enthalpy (equation 4)
- solvent-solute interaction (equation 5)
- elastic enthalpy (equation 6)
- changes in configurational entropy (last term in equation 7)
- temperature effects (last term of equation 7)
- reduction in the strength of intergranular bonds compared to the intragranular bonds (first term of equation 7)
- grain size effects (equation 9)

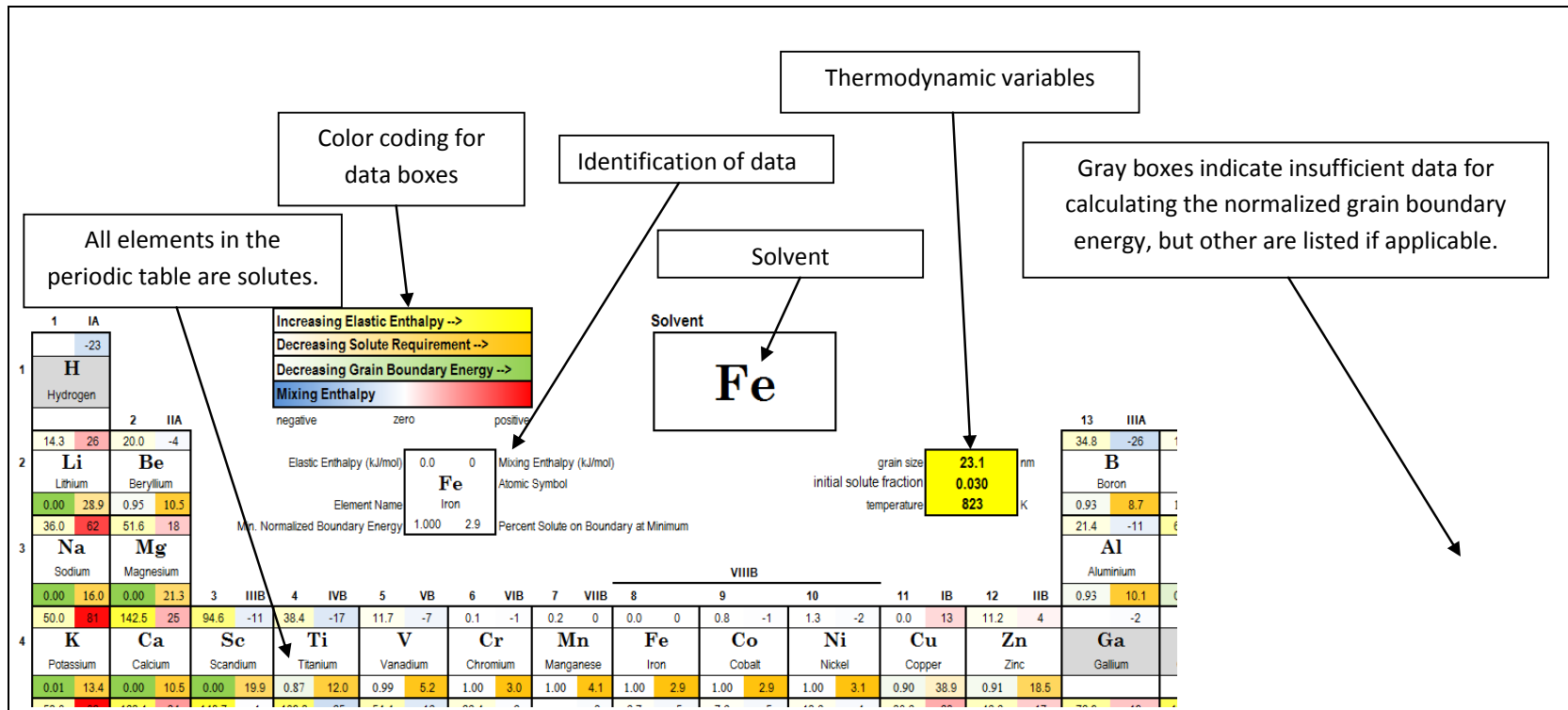


Figure 1. Explanation of tabulated data.

L

The **elastic enthalpy** should be large to drive segregation. This is indicated by a bold yellow color.

The **mixing enthalpy** should be near zero to prevent strong phase separation or intermetallic formation. Intermetallics tend to form when bold blue, and phase separation occurs when bold red. Ideally, this box should be white.

109.3	-25
Zr	
Zirconium	

The **normalized grain boundary energy** should be zero for complete stabilization. This is indicated by a dark green box.

This is the **percentage of solute** that is required to reach the minimum energy whether that energy is zero or not. This box should be dark orange.

Figure 2. Desirable characteristics for stabilization.

This model does not account for the following:

- the formation of secondary phases
- the retained elastic misfit of segregated solute
- change in the regular solution interaction parameter and elastic misfit due to changes in composition temperature or strain
- excess entropy contributions
- multispecie co-segregation effects
- electronic contributions
- relaxation effects

Grain boundary segregation is an extremely complex phenomenon and, as such, the utility of any model that allows for greater accuracy needs to be weighed against the cost of the complexity of said model. Furthermore, the precision with which parameters are known, or can be experimentally determined, is important for the practical application of any model. A model that is more consistent with the physical nature of segregation cannot be used to make predictions that are more accurate if there is a lack of precision in the additional parameters required. This work attempts to strike a reasonable compromise between greater physical accuracy and increased complexity, but it is not meant to replace the thermodynamically rigorous and more complex models for interfacial segregation.

To demonstrate the utility of the model (equation 7) with respect to grain size, global solute content, and temperature, we have applied it to Cu with solutes of group IVB elements (i.e., Ti, Zr, and Hf) and group VB elements (i.e., V, Nb, and Ta). Consulting the Cu data (table 1) reveals that these two groups show negative and positive enthalpies of mixing (positive and negative ΔH_m), respectively. The variables used are detailed in the legends of the comparison graphs.

Table 1. General data pertaining to the Cu alloy systems discussed. The solubility limit assumes Cu as the solvent. A zero value indicates negligible solubility with no equilibrium value listed in the phase diagram. Enthalpies are calculated with Cu as the solvent.

	Cu	Group IVB			Group VB		
		Ti	Zr	Hf	V	Nb	Ta
Atomic No.	29	22	40	72	23	41	73
Atomic mass (g/mol)	63.546	47.88	91.224	178.49	50.9415	92.90638	180.9479
Solubility Limit (at%)	100	5	0.12	0	0	0	0
Enthalpy of Mixing (kJ/mol)	0	-9	-23	-17	5	3	2
Elastic Enthalpy (kJ/mol)	0	30.1	90.8	85.3	8.5	40.2	43.6
Surface Energy (J/mol ²)	1.8075	2.0445	1.9545	2.1715	2.586	2.6775	3.026
Atomic Radius (Å)	1.57	2	2.16	2.16	1.92	2.08	2.09
Atomic Volume (cm ³ /mol)	7.1	10.64	14.06	13.41	8.78	10.84	10.9
Bulk Modulus (GPa)	137.8	108.4	89.8	109	158	170.3	196.3
Shear Modulus (GPa)	48.3	45.6	35	56	46.7	37.5	69.2
Elastic Modulus (GPa)	129.8	120.2	98	141	127.6	104.9	185.7
Crystal Structure	fcc	hcp	hcp	hcp	bcc	bcc	bcc

An example of the comparisons is shown in figure 3. Each curve indicates the normalized grain boundary energy for a single grain size, global solute concentration, and temperature as a function of solute segregation (see concentration on the abscissa). For any temperature above 0 K, the curves pass through a minimum determined by the relative magnitudes of ΔH_{seg} and ΔS_{seg} . Discontinuities (denoted by asterisks) are observed where the solute has been totally exhausted from the bulk. This boundary concentration is the maximum allowed by the global solute concentration. Any solute concentration above this limit implies that a negative bulk concentration exists, which is physically impossible.

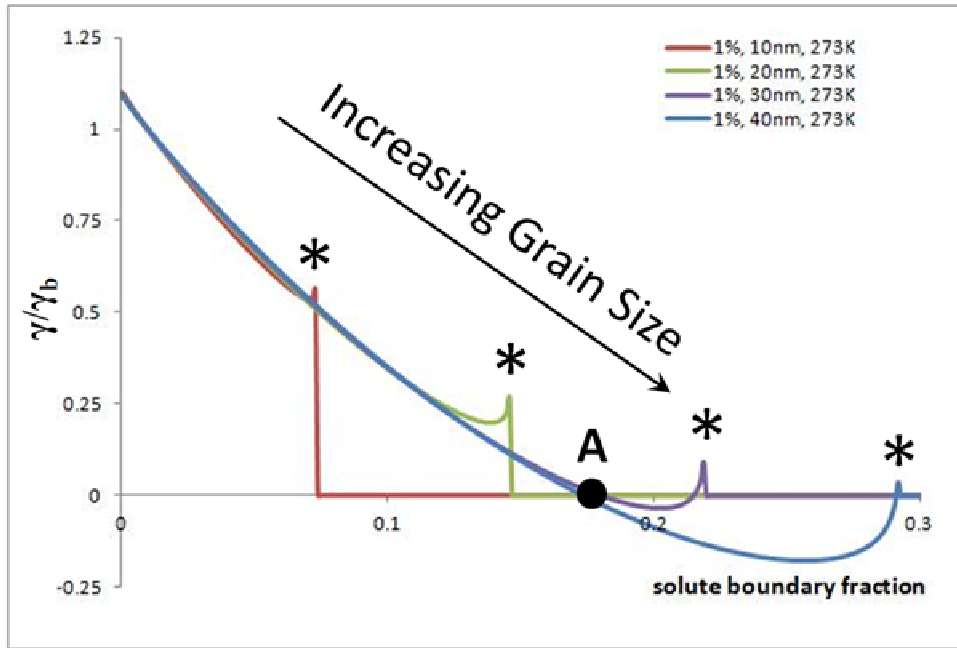


Figure 3. Explanation of comparisons. (See text for descriptions of symbols).

If the curves cross the abscissa with a negative slope (labeled as point “A” in figure 3), system stability is expected at the concentration where it intersects. Any concentration greater than this initial zero point is not of practical importance, as it predicts a negative interfacial energy that is not reasonable to expect in such systems. The general trend shown is that as grain size increases from 10 to 40 nm the normalized boundary energy decreases for a given concentration, and the solute boundary concentration needed for stabilization decreases with increasing grain size. When increasing from 20 to 30 nm, the zero boundary condition is satisfied. This is interpreted to mean that the grain size is unstable below 30 nm (or near that value) and will grow until the appropriate size is reached because the solute available is a fixed value.

For the negative ΔH_m solutes, an increase of grain size and global solute concentration shifts the curves down and to higher grain boundary solute fractions. The same was observed with the positive ΔH_m , but the variation is more dramatic. For the temperature effect, the curves for both negative and positive ΔH_m systems shifted up and to lower concentrations. Again, the positive ΔH_m systems are more sensitive. Therefore, the model indicates that positive ΔH_m systems are easier to stabilize at lower temperatures where segregation is more likely, as bonding with the solvent is not favorable.

By varying the grain size (see figures 4 and 5), it is evident that as the grain size is increased, the potential to achieve a zero energy boundary condition (stability) is improved. The fourth-row elements (i.e., Ti and V) do not achieve stability for any size up to 90 nm, whereas the others do benefit from an increased grain size. After 100 nm, the grain size has a much less pronounced effect.

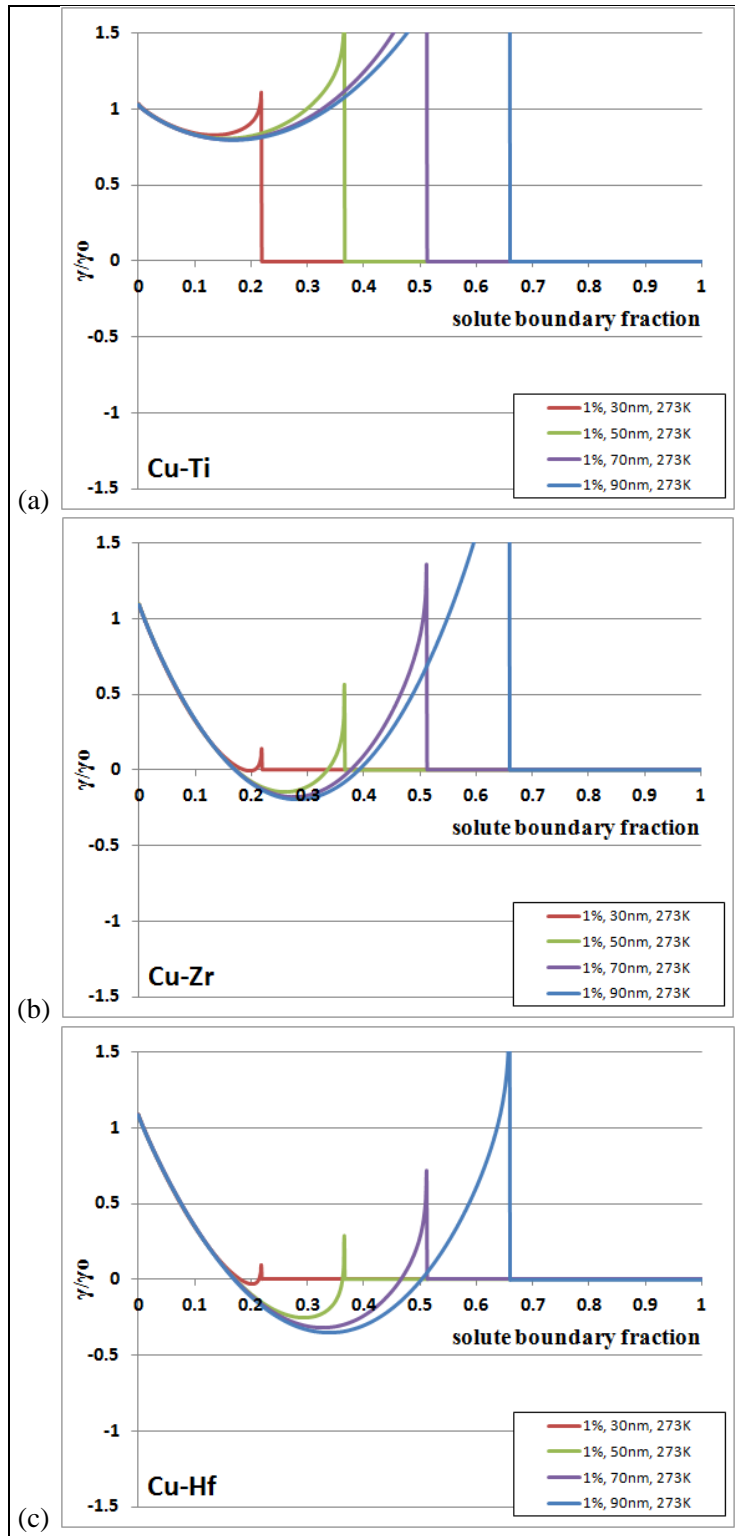


Figure 4. The variation of normalized grain boundary energy as a function of grain size for (a) Cu-Ti, (b) Cu-Zr, and (c) Cu-Hf. All variables are listed in the legend.

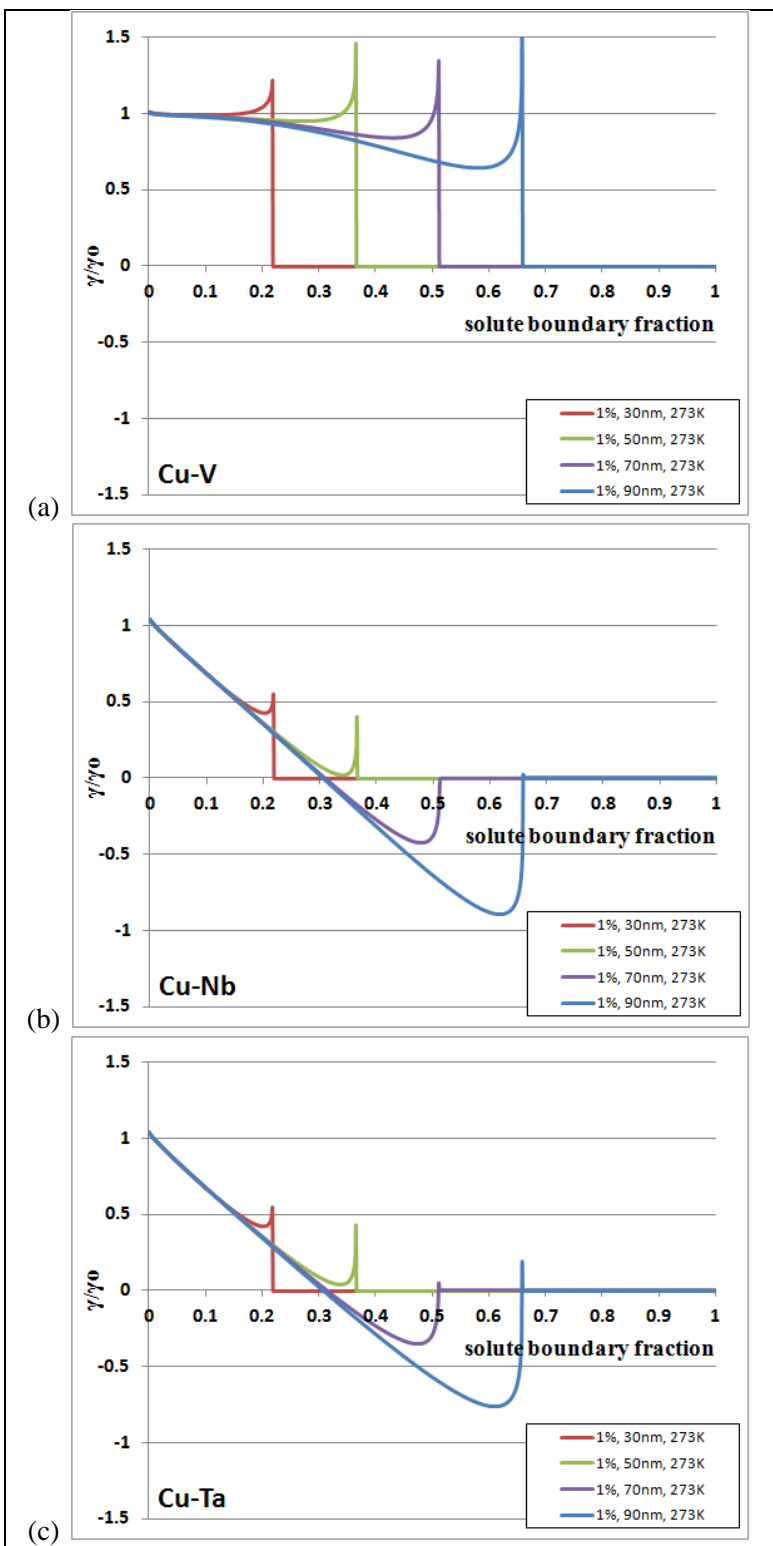


Figure 5. The variation of normalized grain boundary energy as a function of grain size for (a) Cu-V, (b) Cu-Nb, and (c) Cu-Ta. All variables are listed in the legend.

When the global solute content is adjusted (see figures 6 and 7), the stability is also improved by an increase. Cu-V can now achieve a zero boundary energy, but it is also important to note that it requires ~77% boundary coverage, which is likely to lead to precipitation and/or phase separation. Increasing the solute content is not always a good practice, as unfavorable factors such as precipitate formation can be exacerbated by a higher content. It is generally observed, experimentally, that secondary phases must be kinetically hindered (33) from forming, as they provide competition for the available solute, causing destabilization of the boundaries and rapid grain coarsening.

The temperature also has a significant influence on stability, as shown in figures 8 and 9. When the temperature is raised, stability is quickly lost, even for alloys that achieve it at low concentrations. A notable change in the variables is that the grain size was increased to 100 nm to help accent the effect of temperature, as smaller sizes quickly went off the chart.

The free energy curves displayed in these comparisons are an example of the type used as the basis for the periodic table data in the appendix. The periodic table values are calculated using equation 7 for the fixed temperature, solute concentration, and grain size. The minimum, or zero point, of the calculated curves is reported in the periodic table for each solvent-solute system, with the corresponding solute percentage at which they occur. The elastic and mixing enthalpies are calculated independently and are not dependent on the variables.

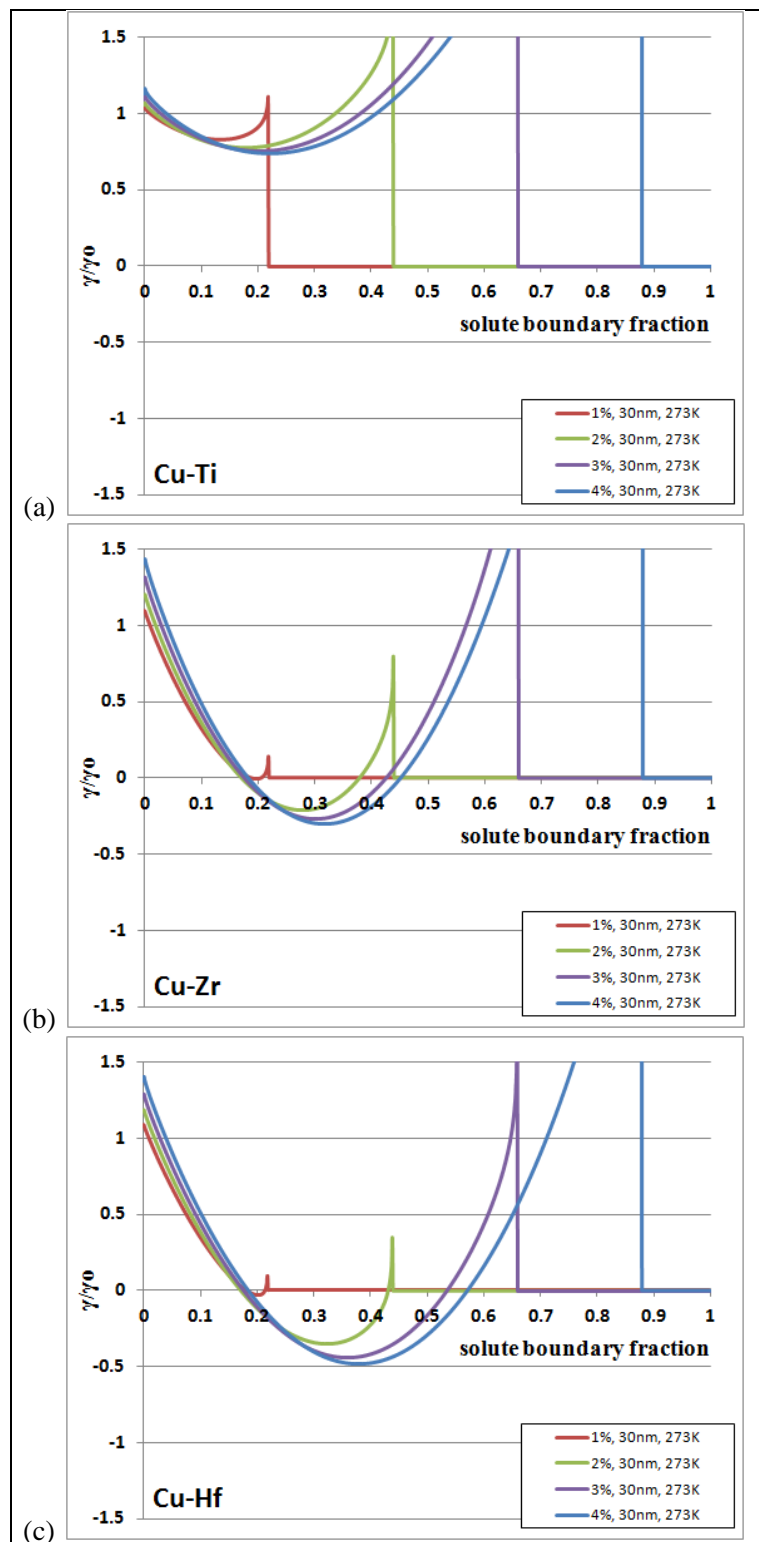


Figure 6. The variation of normalized grain boundary energy as a function of solute concentration for (a) Cu-Ti, (b) Cu-Zr, and (c) Cu-Hf. All variables are listed in the legend.

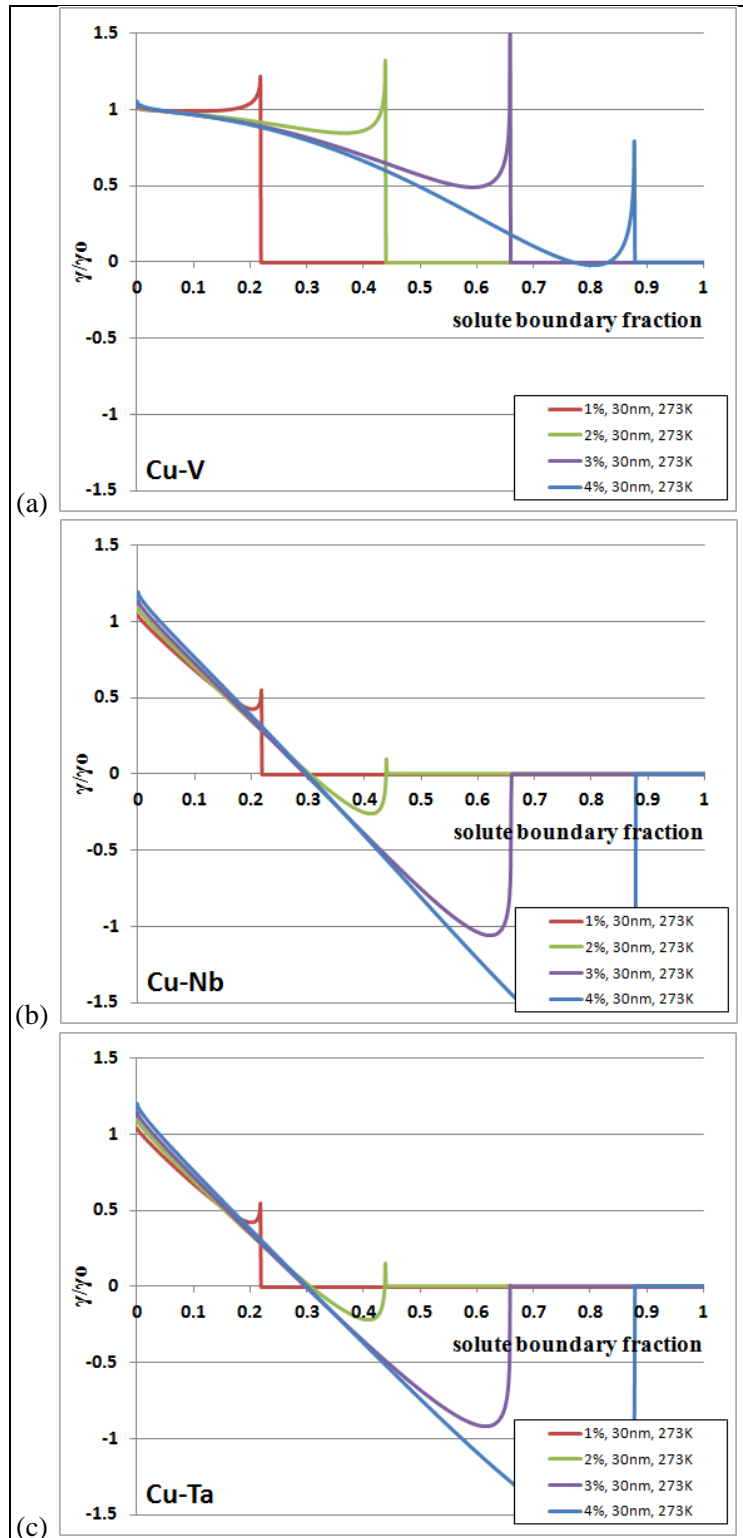


Figure 7. The variation of normalized grain boundary energy as a function of solute concentration for (a) Cu-V, (b) Cu-Nb, and (c) Cu-Ta. All variables are listed in the legend.

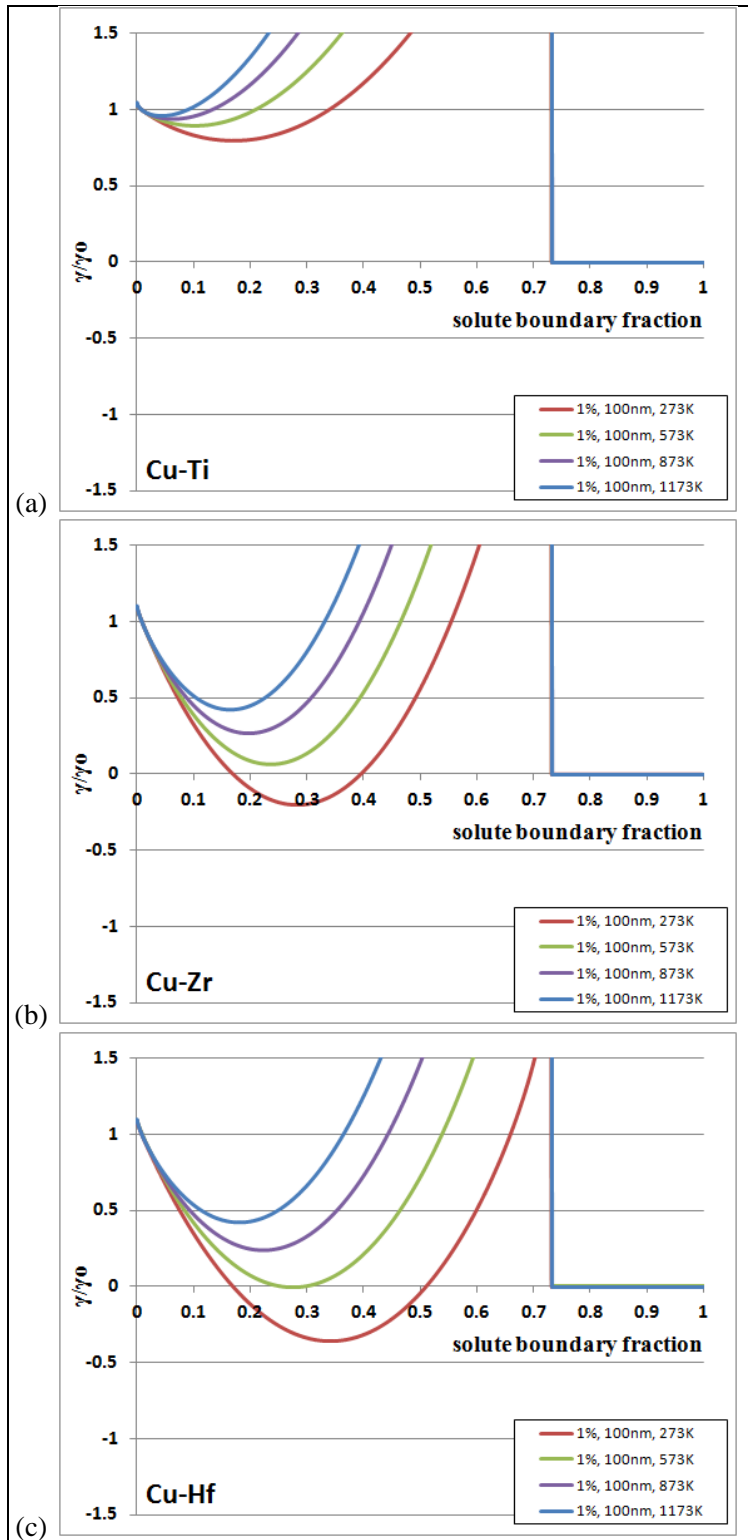


Figure 8. The variation of normalized grain boundary energy as a function of temperature for (a) Cu-Ti, (b) Cu-Zr, and (c) Cu-Hf. All variables are listed in the legend.

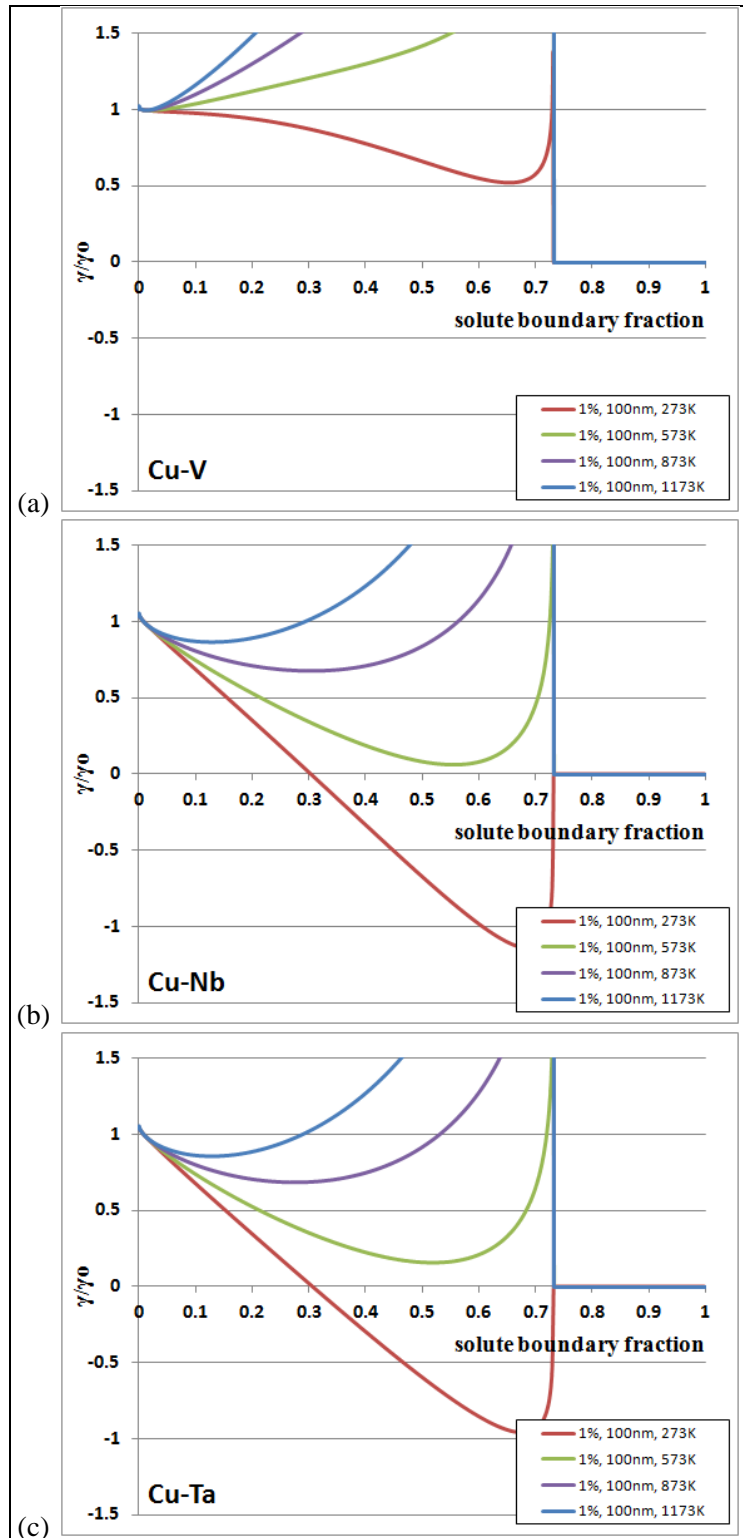


Figure 9. The variation of normalized grain boundary energy as a function of temperature for (a) Cu-V, (b) Cu-Nb, and (c) Cu-Ta. All variables are listed in the legend.

The variables displayed here are instructive when considered individually, but system stability is dependent on all simultaneously. The free energy of the system must be minimized with respect to grain size and solute content at any given temperature. Therefore, if plotted three-dimensionally, the optimum conditions would be located, at the minimum, in a free energy surface, not simply the minimum for a single curve. In forthcoming work (part 2), the stabilization behavior of select alloys will be experimentally compared to the predictions reported here. Though this model has been found to be qualitatively correct with commonly studied systems available in literature, we plan to extend it to new systems.

5. Conclusions

A predictive free energy model for grain boundary segregation and grain-size stability in nanocrystalline alloys was used for assessing the stability in 2288 distinct alloys with base elements of lithium, beryllium, boron, sodium, magnesium, aluminum, potassium, calcium, scandium, titanium, vanadium, chromium, manganese, iron, cobalt, nickel, copper, zinc, rubidium, strontium, yttrium, zirconium, niobium, molybdenum, ruthenium, rhodium, palladium, silver, cadmium, indium, tin, barium, hafnium, tantalum, tungsten, rhenium, osmium, iridium, platinum, gold, thallium, lead, thorium, and uranium. The model incorporated easily accessible information, which allowed a more universal application. For each alloy pair, the values for elastic enthalpy, mixing enthalpy, minimum normalized grain boundary energy, and the boundary concentration at the free energy minimum were reported. The use of color coding allowed determination of the best solute(s), which can drastically reduce development time for stabilizing alloys. The free energy of each system was shown to be dependent on the solvent, grain size, solute content, and temperature. The model was demonstrated on Cu alloys having both positive and negative enthalpies of mixing. The current library was developed using readily available information and can be extended to include all of the elements where the appropriate data is available for calculation. In forthcoming work (part 2), the stabilization behavior of select alloys will be experimentally compared to the predictions reported here.

6. References

1. Meyers, M. A.; Mishra, A.; Benson, D. J. *Prog. Mat. Sci.* **2006**, *51*, 427.
2. Kumar, K. S.; Van Swygenhoven, H.; Suresh, S. *Acta Mater.* **2003**, *51*, 5743.
3. Weertman, J. Mechanical Behavior of Nanocrystalline Metals. In *Nanostructured Materials*; Koch, C. C., Ed.; Noyes Publications: Norwich, NY, 2002, p 397.
4. Weertman, J. R.; Farkas, D.; Kung, H.; Mayo, M.; Mitra, R.; Swygenhoven, H. *MRS Bull.* **1999**, *24*, 44.
5. Koch, C. C. *Scr. Mat.* **2003**, *49*, 657.
6. Ma, E. *Scr. Mat.* **2003**, *49*, 663.
7. Zhu, Y. T.; Liao, X. *Nat. Mat.* **2004**, *3*, 351.
8. Youssef, K. M.; Scattergood, R. O.; Murty, K. L.; Horton, J. A.; Koch, C. C. *Appl. Phys. Lett.* **2005**, *87*, 091904-1.
9. Youssef, K. M.; Scattergood, R. O.; Murty, K. L.; Koch, C. C. *Scr. Mat.* **2006**, *54*, 251.
10. Zhao, Y.; Liao, X.; Cheng, S.; Ma, E.; Zhu, Y. T. *Adv. Mater.* **2006**, *18*, 2280.
11. Chen, L. C.; Spaepen, F. *J. Appl. Phys.* **1991**, *69*, 679.
12. Gleiter, H. *Prog. Mat. Sci.* **1989**, *33*, 223.
13. Birringer, R. *Mater. Sci. Eng. A.* **1989**, *33*, 117.
14. Gunther, B.; Kumpmann, A.; Kunze, H. D. *Scr. Mater.* **1992**, *833*, 27.
15. Hibbard, G.; Aust, K. T.; Palumbo, G.; Erb, U. *Scr. Metall.* **2001**, *44*, 513.
16. Klement, U.; Erb, U.; ElSherik, A. M.; Aust, K. T. *Mater. Sci. Eng. A.* **1995**, *203*, 177.
17. Malow, T. R.; Koch, C. C. *Acta Mater.* **1997**, *45*, 2177.
18. Humphreys, F. J.; Hatherly, M. *Recrystallization and Related Annealing Phenomena*; Elsevier Science, Inc.: Tarrytown, NY, 1996, pp 289–295.
19. Krill, C. E.; Ehrhardt, H.; Birringer, R. *Z. Metallkd.* **2005**, *96*, 1134.
20. Murr, L. E. *Interfacial Phenomena in Metals and Alloys*; Boston, MA, Addison-Wesley: 1975, pp 130–133.

21. Weissmuller, J. *J. Mater. Res.* **1994**, *9*, 4.
22. Weissmuller, J. *Nanostruct. Mater.* **1993**, *3*, 261.
23. Defay, R.; Prigogine, I.; Bellmans, A.; Everett, D. H. *Surface Tension and Adsorption*; Wiley: New York, NY, 1966.
24. McLean, D. *Grain Boundaries in Metals*; Oxford Press: London, England, 1957.
25. Wynblatt, P.; Ku, R. C. *Surf. Sci.* **1977**, *65*, 511.
26. Wynblatt, P.; Chatain, D. *Metall. Mater. Trans. A.* **2006**, *37*, 2595.
27. Friedel, J. *Adv Phys.* **1954**, *3*, 446.
28. VanLeeuwen, B. K.; Darling, K. A.; Liu, Z. K.; Koch, C. C.; Scattergood, R. O. *Acta Mater.* (submitted) **2012**.
29. Porter, D. A.; Easterling, E. E. *Phase Transformations in Metals and Alloys*; 2nd ed.; Chapman Hall: London, 1992.
30. Takeuchi, A.; Inoue, A. *Mater. Trans.* **2005**, *46*, 2817.
31. Miedema, A. R. P. Fd.; Chatel, F. Rd. *Boer. Phys. B+C*, **1980**, *100*, 1.
32. Darling, K. A.; VanLeewen, B. K.; Semones, J. E.; Kocch, C. C.; Scattergood, R. O. *Mater. Sci. Eng. A.* **2011**, *528*, 4365.
33. Koch, C. C.; Scattergood, R. O.; Darling, K. A.; Semones, J. E. *J. Mater. Sci.* **2008**, *43*, 7264.
34. Dake, J. M.; Krill, C. E. *Scr. Mater.* **2012**, *66*, 390.
35. Botcharova, E.; Freudenberg, J.; Schultz, L. *Acta Mater.* **2006**, *54*, 3333.
36. Mula, S.; Bahmanpour, H.; Mal, S.; Kang, P. C.; Atwater, M.; Jian, W.; Scattergood, R. O.; Koch, C. C. *Mater. Sci. and Eng. A.* **2012**, *539*, 330–336.
37. Frolov, T.; Darling, K. A.; Kecske, L. J.; Mishin, Y. *Acta Mater.* **2012**, *60*, 2158.
38. Atwater, M. A.; Scattergood, R. O.; Koch, C. C. *Mater. Sci. and Eng. A* (submitted), **2012**.
39. Detor, A. J.; Schuh, C. A. *Acta Mater.* **2007**, *55*, 371.
40. Detor, A. J.; Schuh, C. A. *Acta Mater.* **2007**, *55*, 4221.
41. VanLeeuwen, B. K.; Darling, K. A.; Koch, C. C.; Scattergood, R. O. *Acta Mater.* **2010**, *58*, 4292.

Appendix. Solvent Stability Tables

Systems based on the following solvents are presented in this section:

1. Lithium
2. Beryllium
3. Boron
4. Sodium
5. Magnesium
6. Aluminum
7. Potassium
8. Calcium
9. Scandium
10. Titanium
11. Vanadium
12. Chromium
13. Manganese
14. Iron
15. Cobalt
16. Nickel
17. Copper
18. Zinc
19. Rubidium
20. Strontium
21. Yttrium
22. Zirconium
23. Niobium

24. Molybdenum

25. Ruthenium

26. Rhodium

27. Palladium

28. Silver

29. Cadmium

30. Indium

31. Tin

32. Barium

33. Hafnium

34. Tantalum

35. Tungsten

36. Rhenium

37. Osmium

38. Iridium

39. Platinum

40. Gold

41. Thallium

42. Lead

43. Thorium

44. Uranium

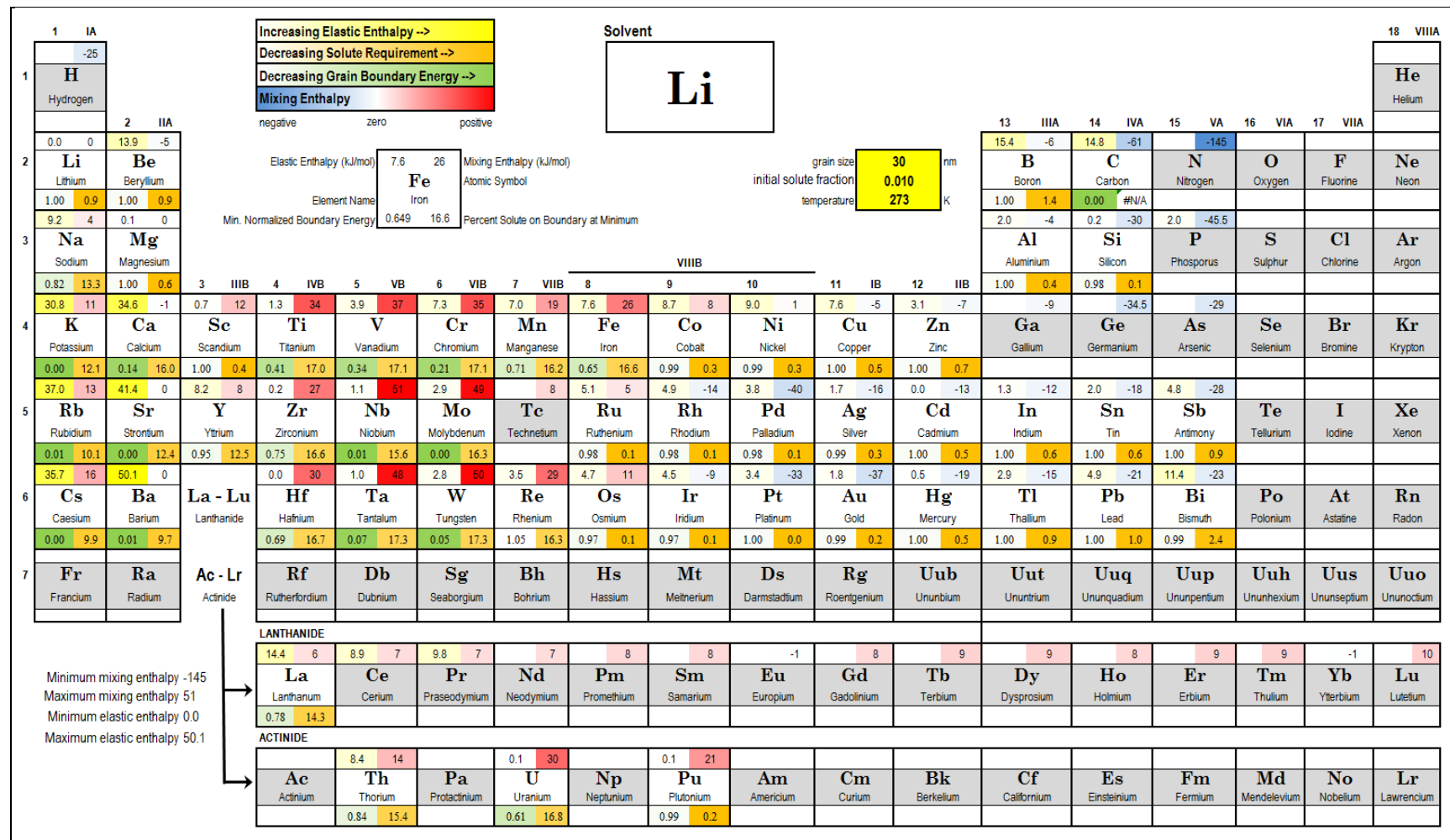


Figure A-1. Lithium.

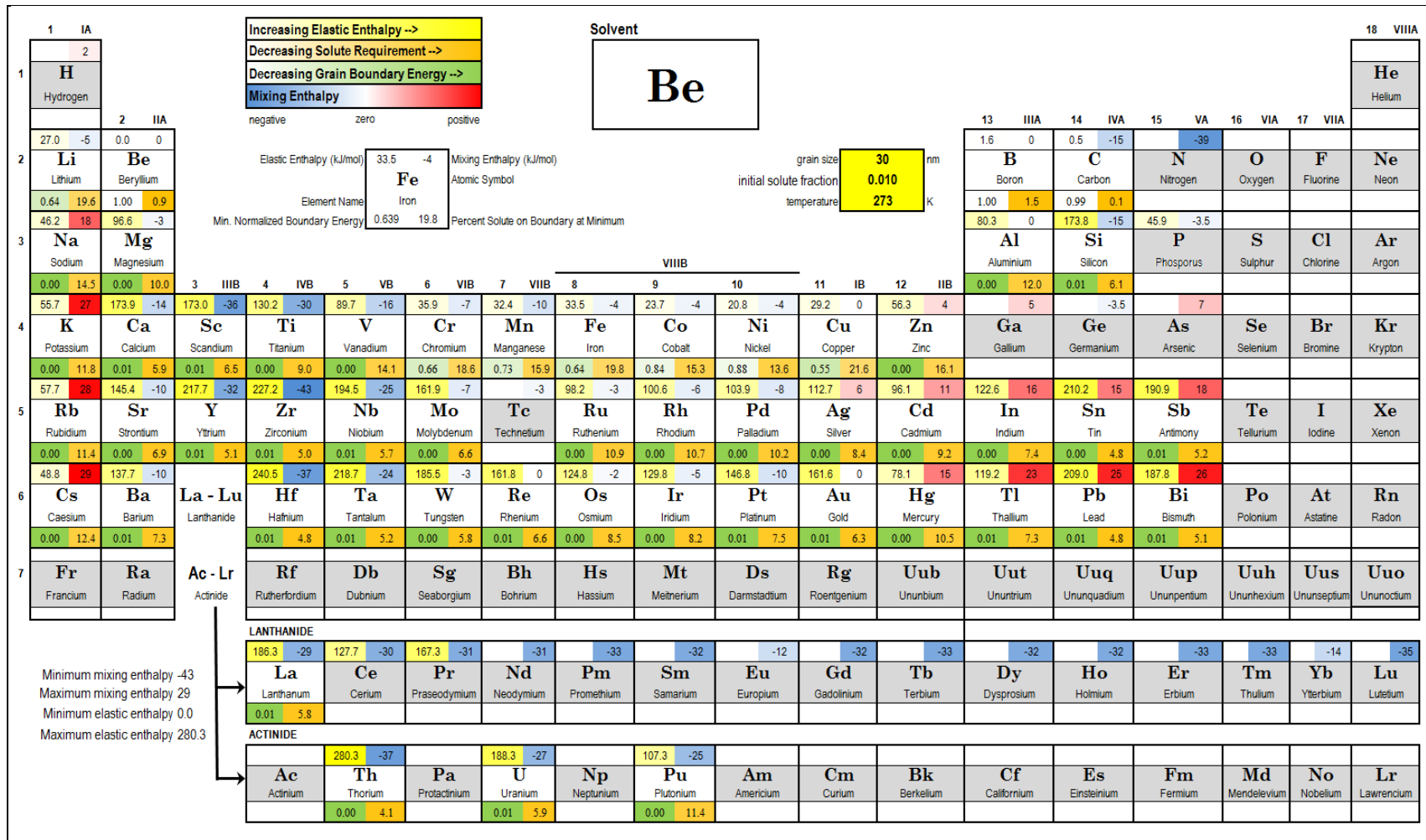


Figure A-2. Beryllium.

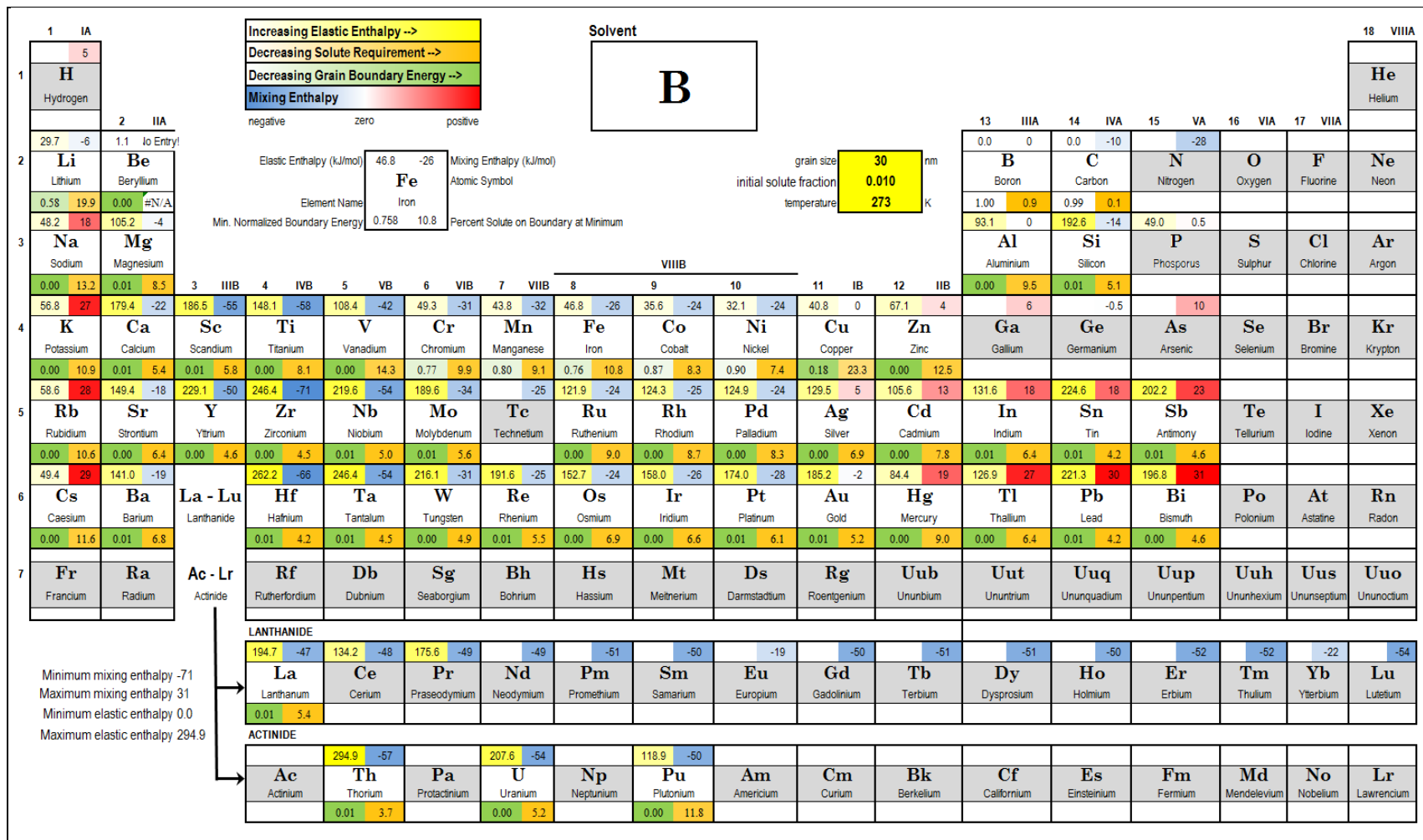


Figure A-3. Boron.

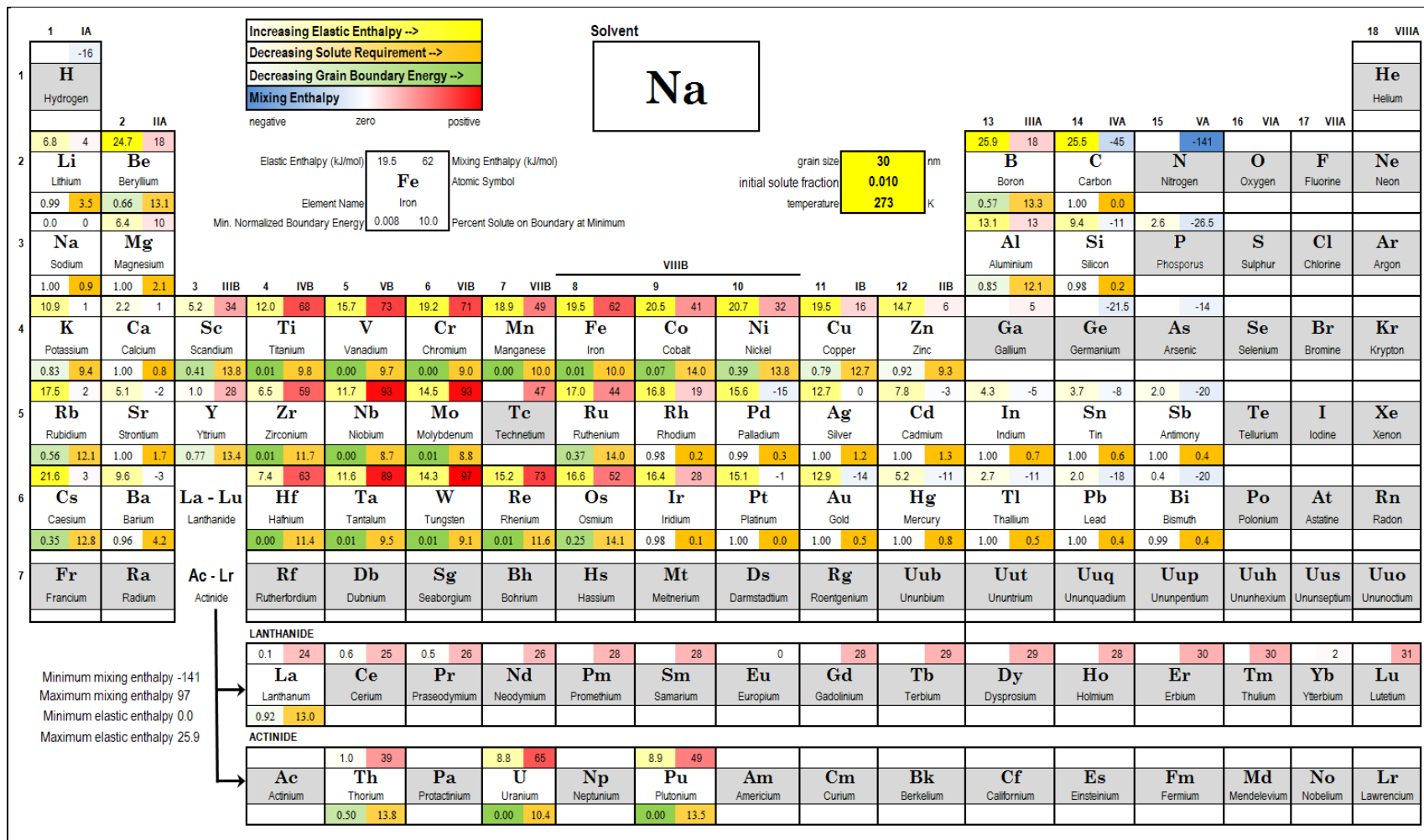


Figure A-4. Sodium.

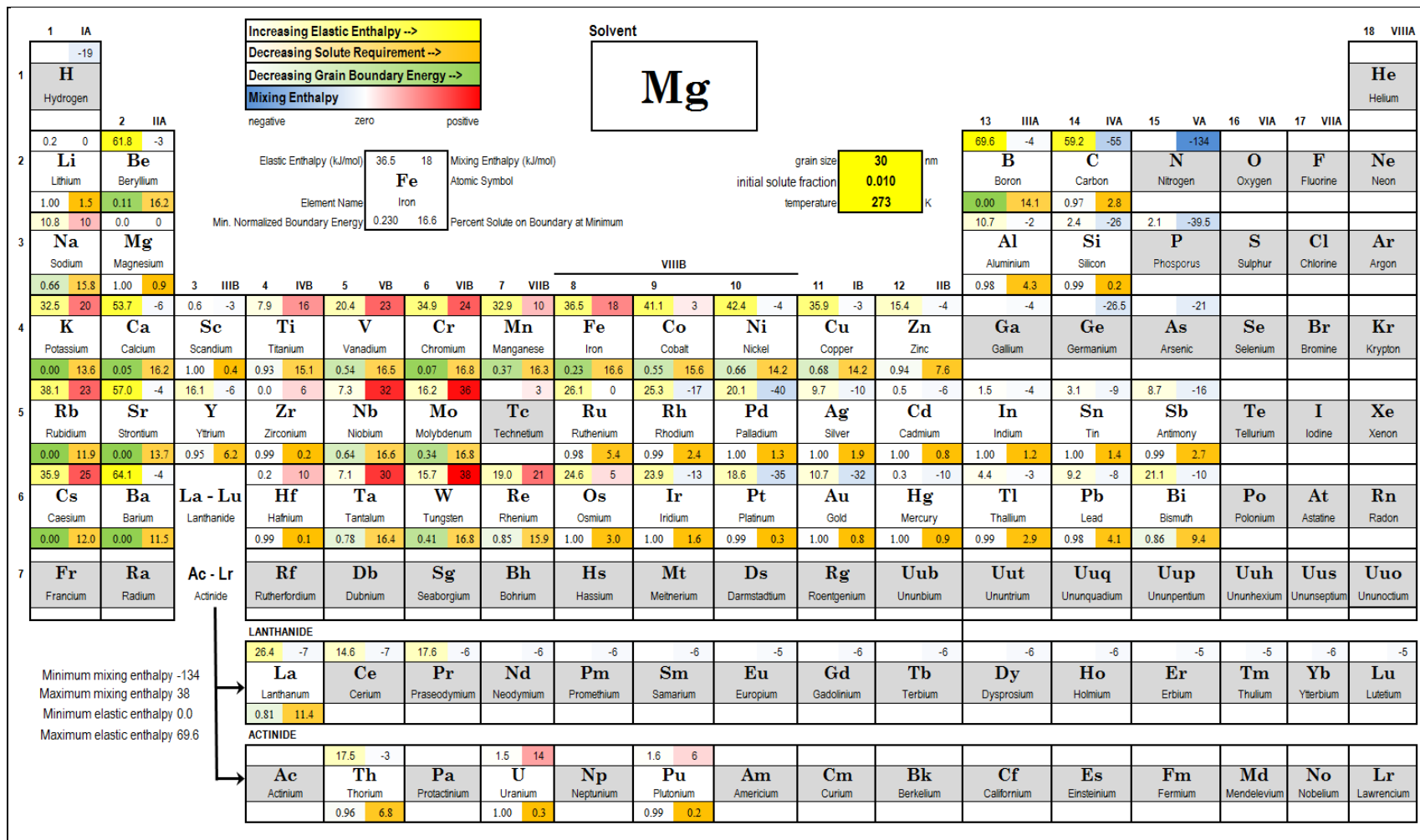


Figure A-5. Magnesium.

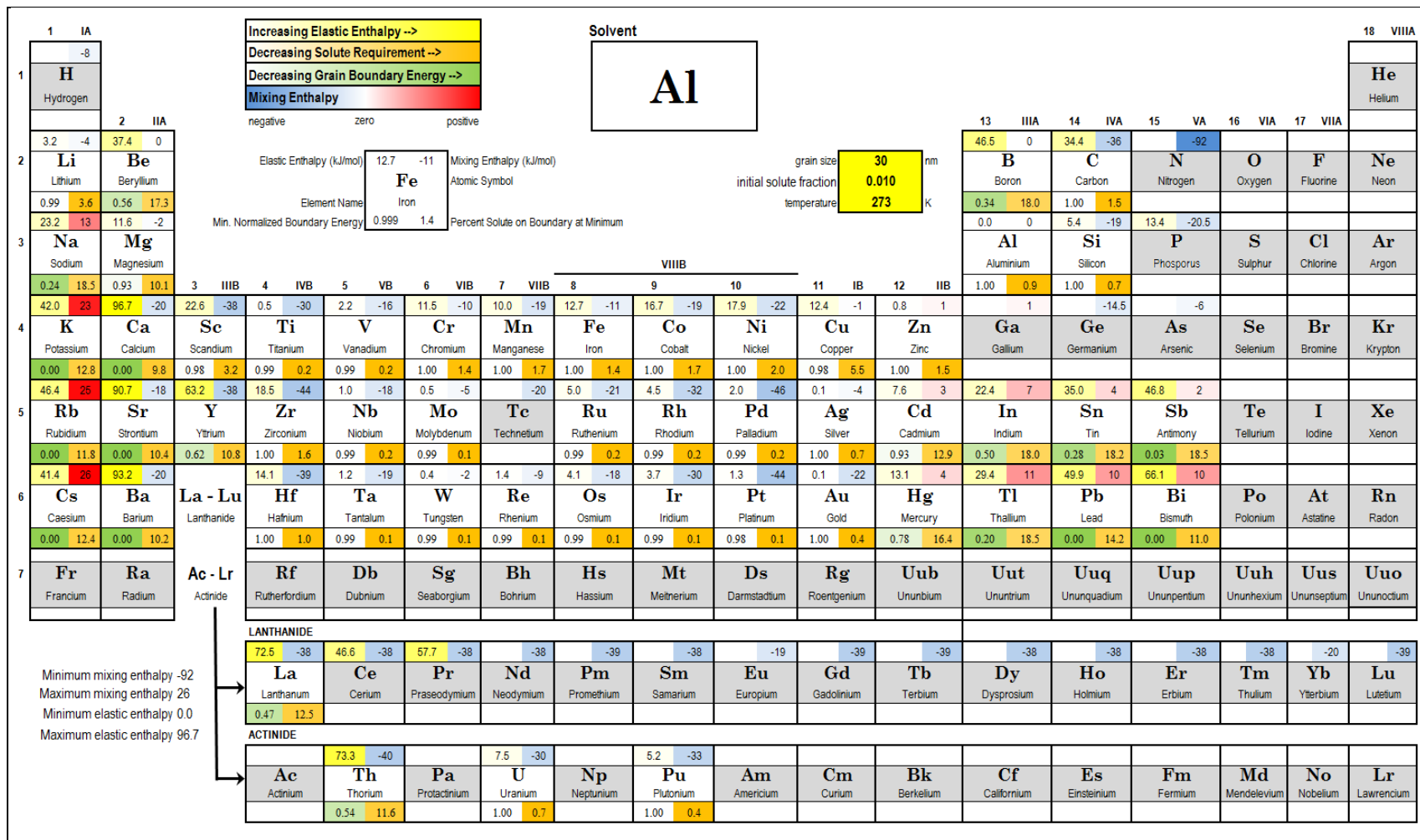


Figure A-6. Aluminum.

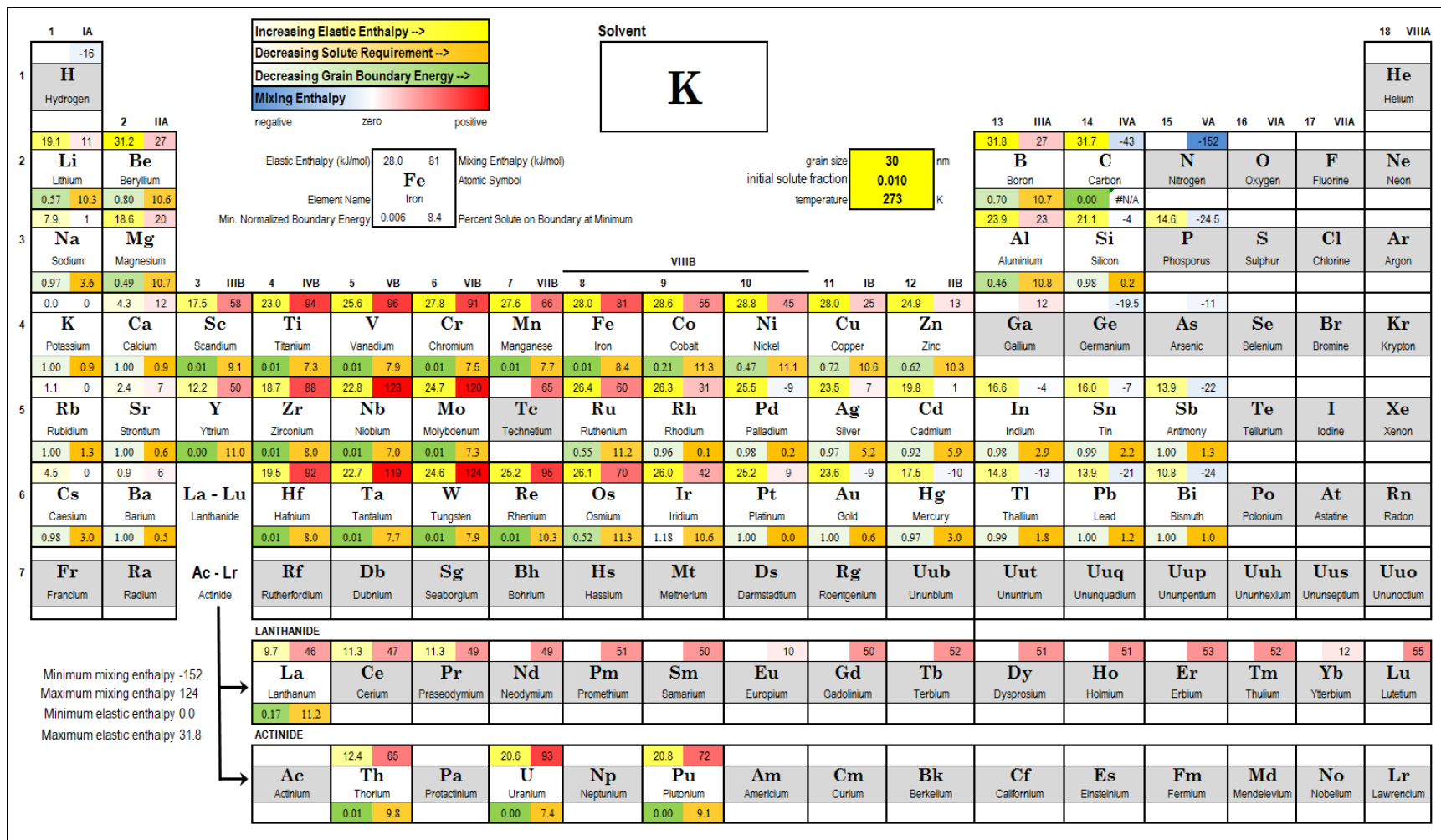


Figure A-7. Potassium.

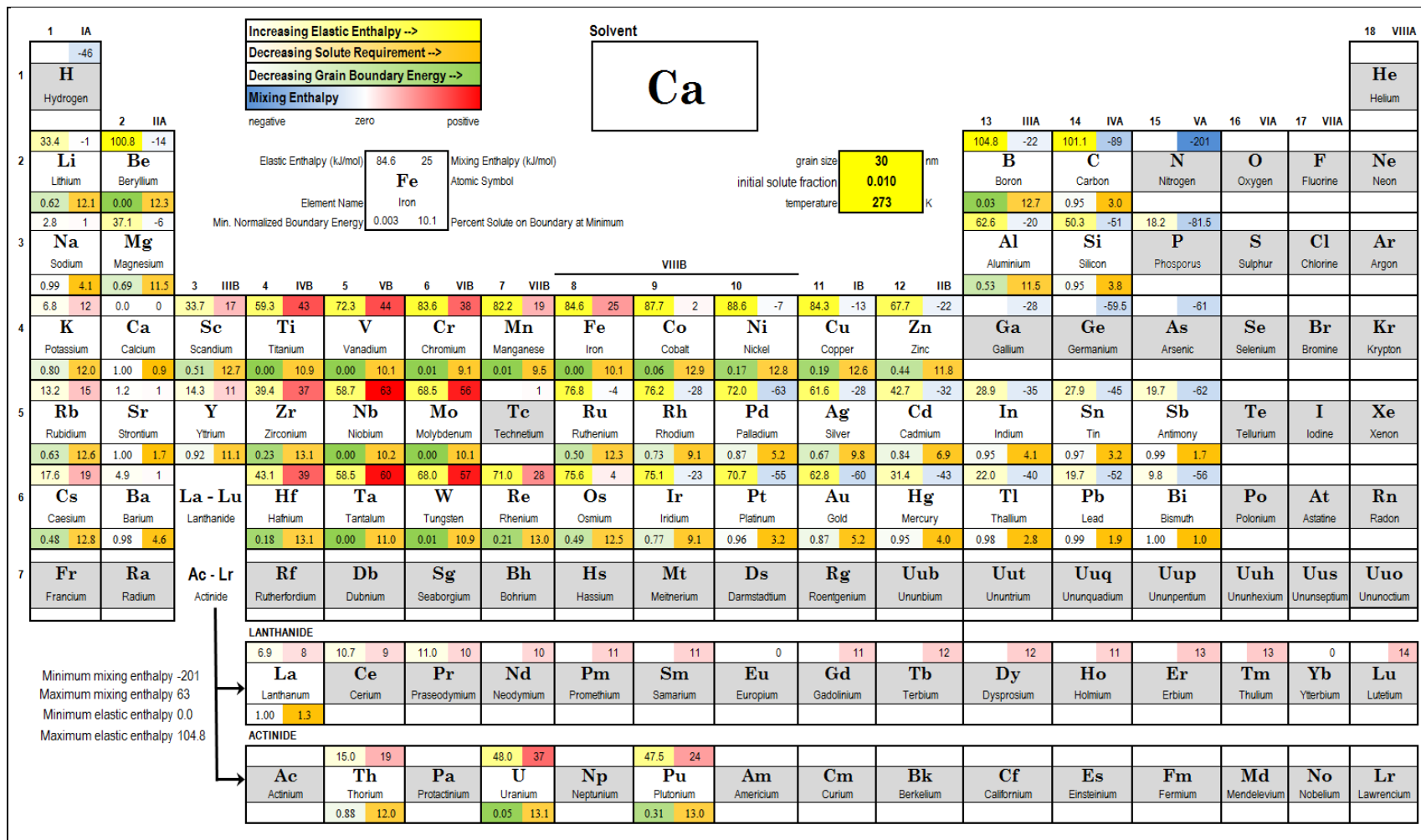
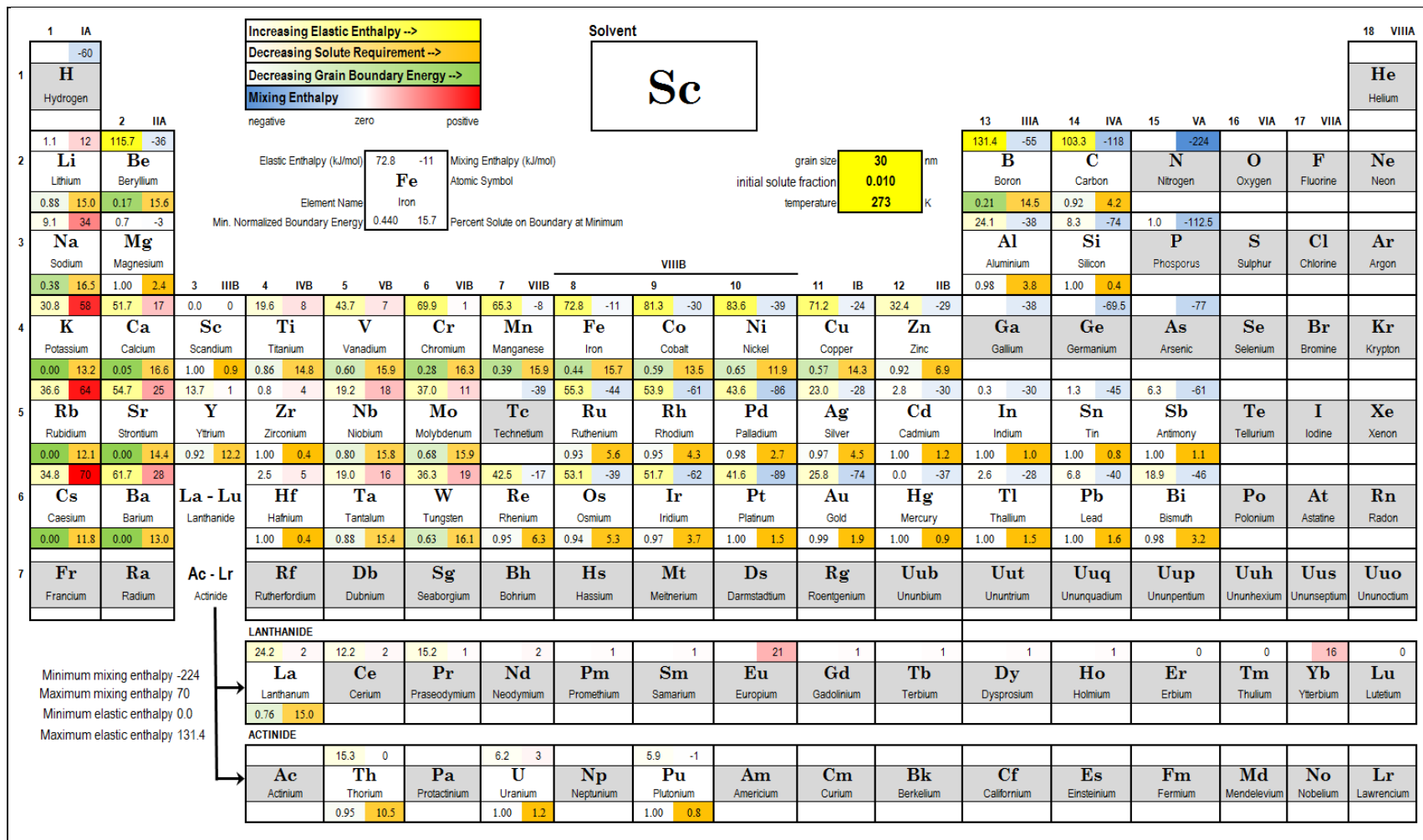


Figure A-8. Calcium.



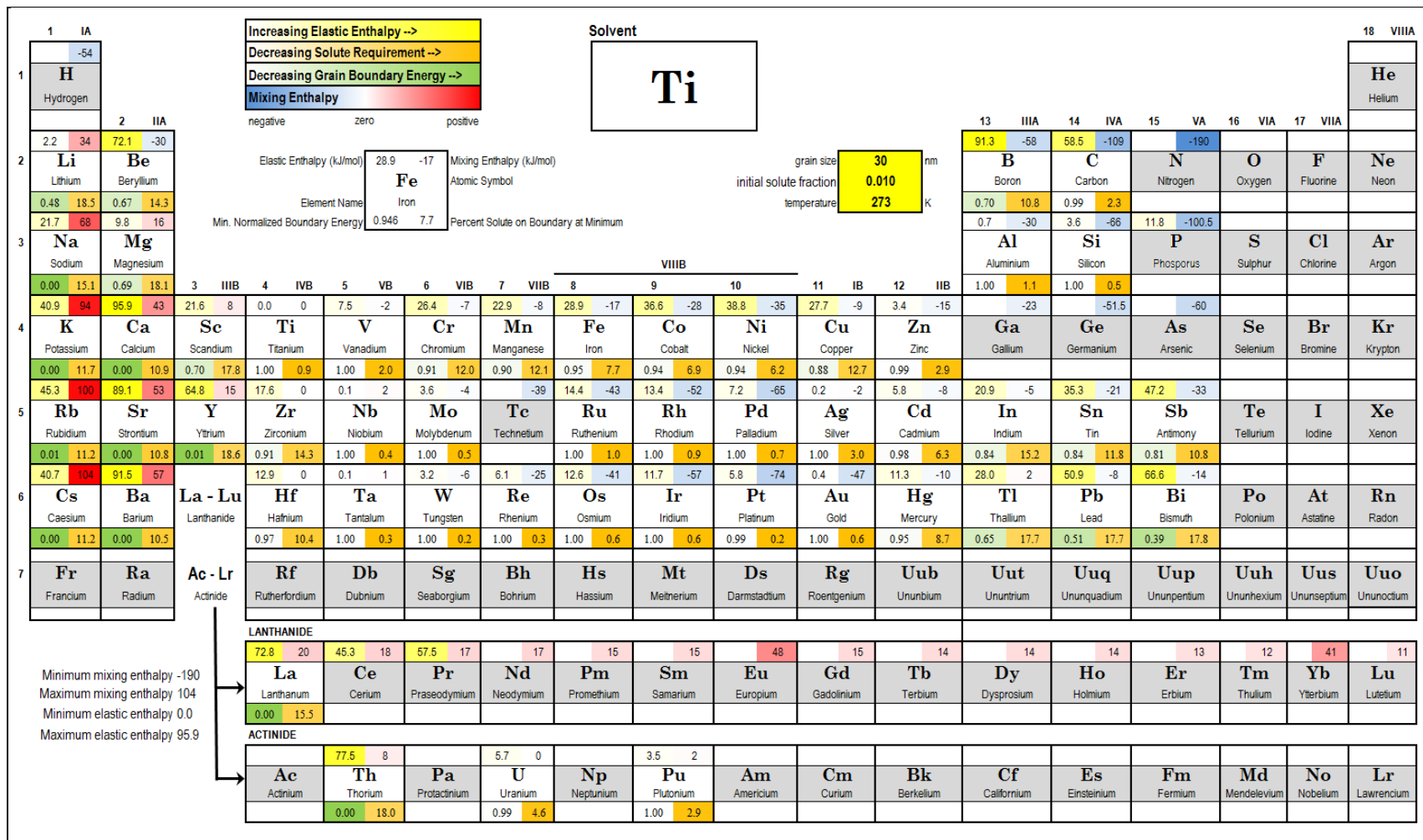


Figure A-10. Titanium.

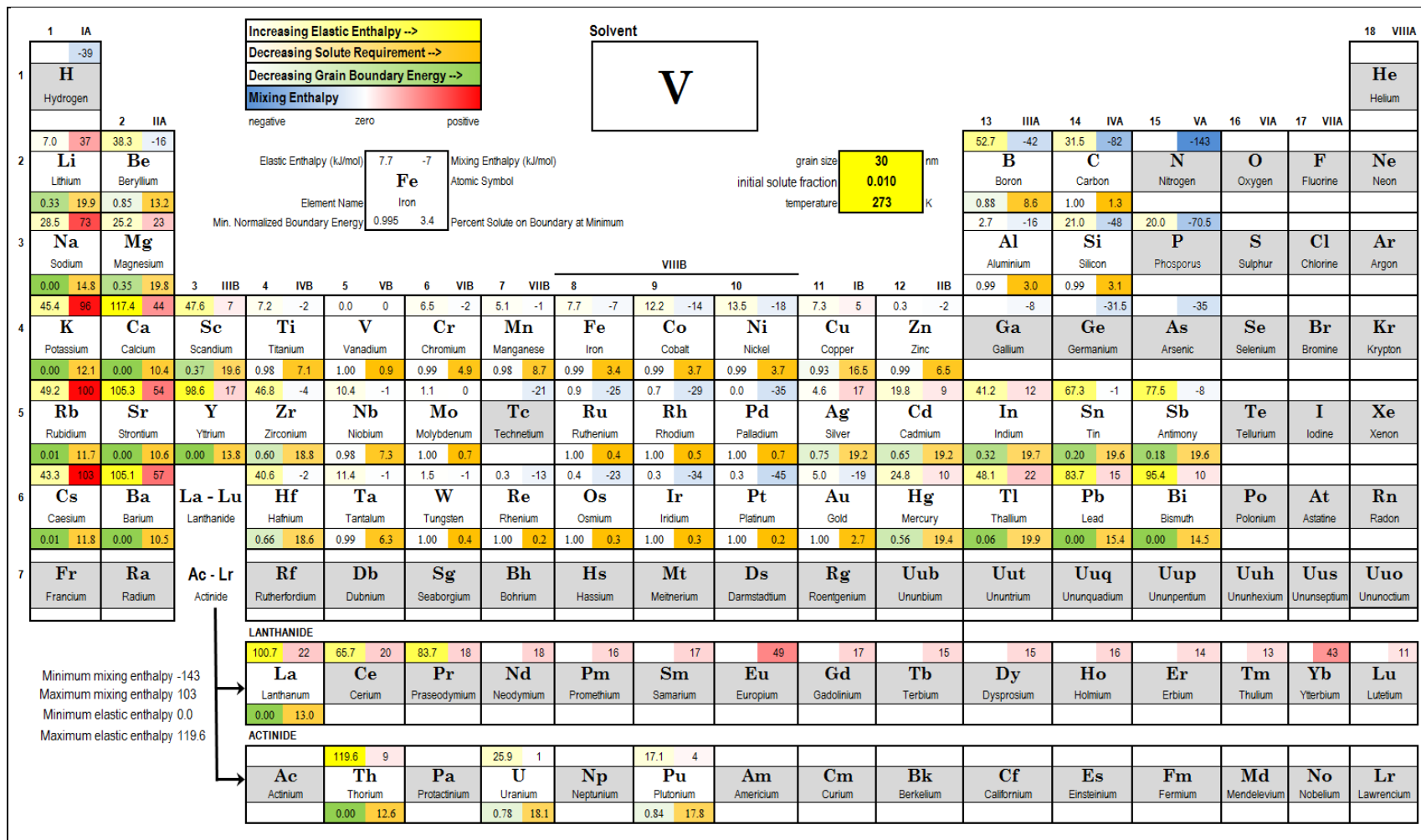


Figure A-11. Vanadium.

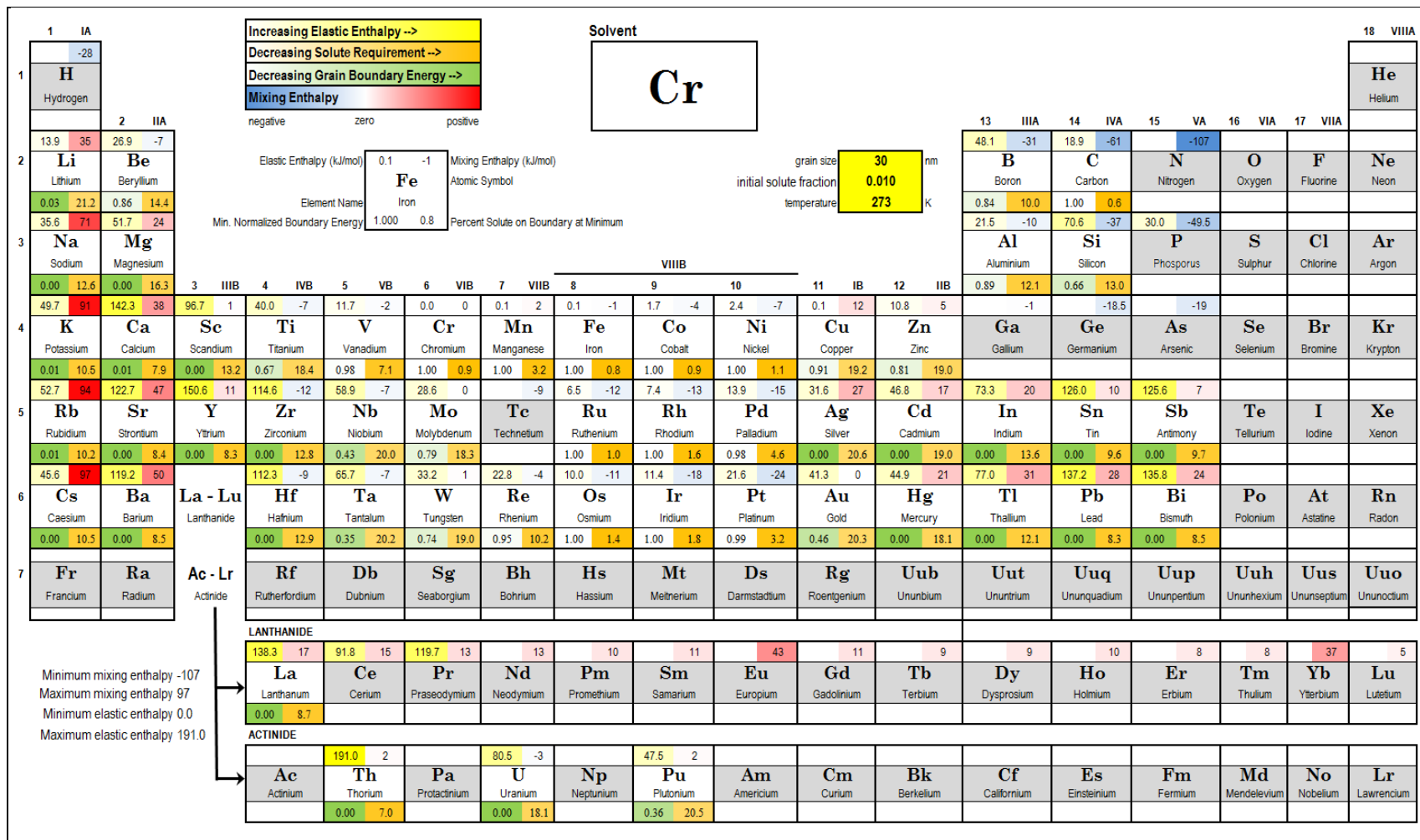


Figure A-12. Chromium.

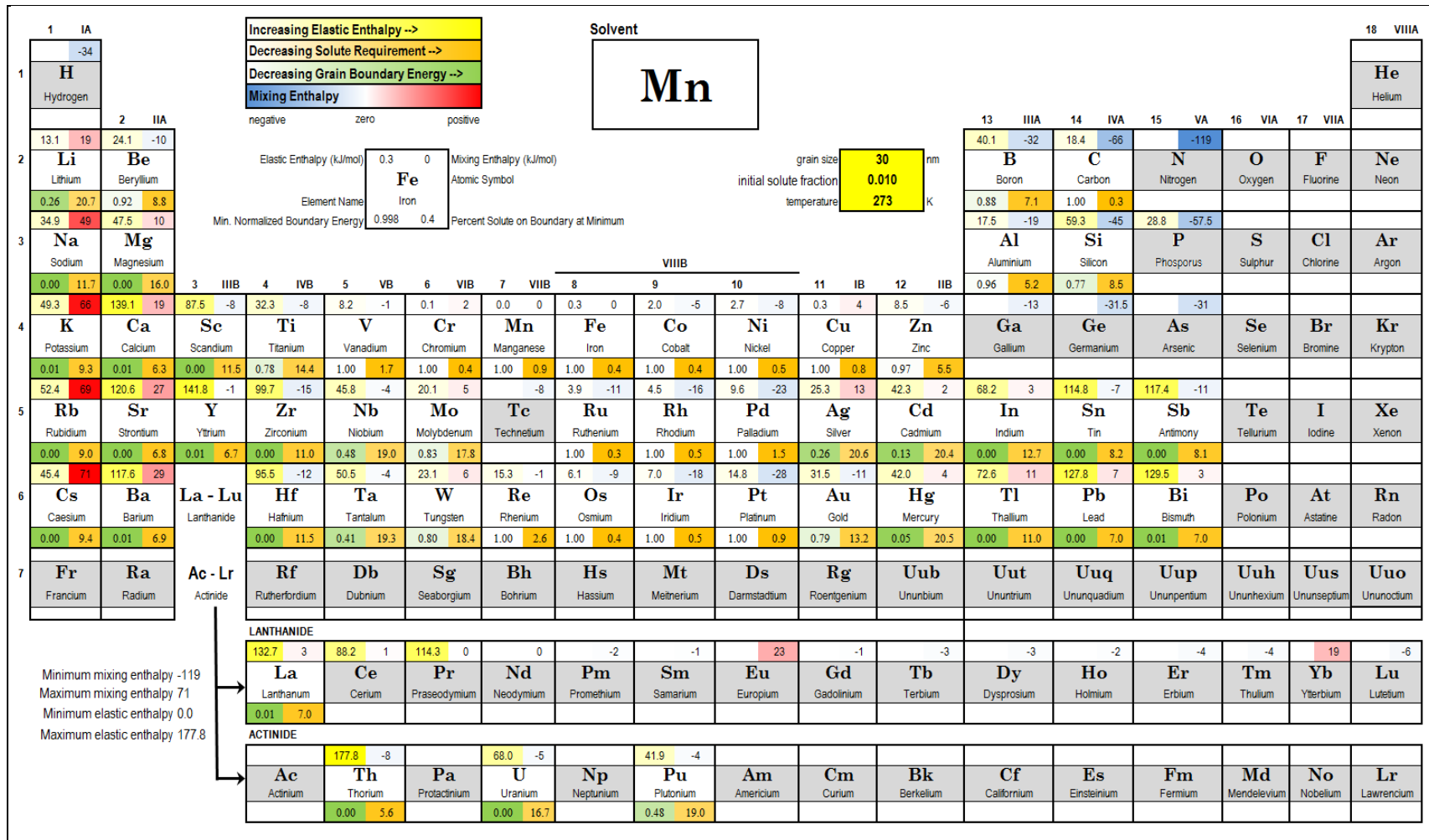


Figure A-13. Manganese.

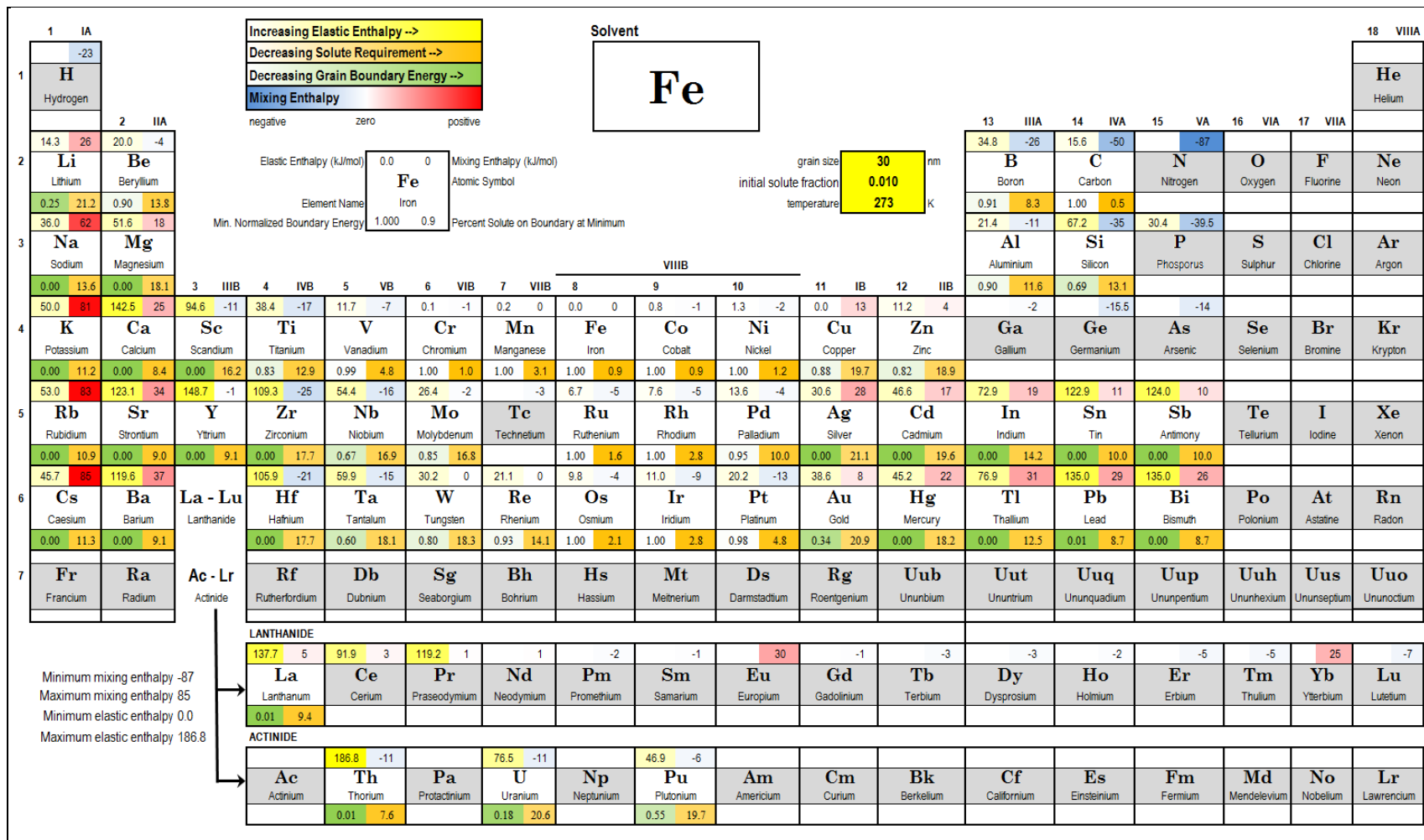


Figure A-14. Iron.

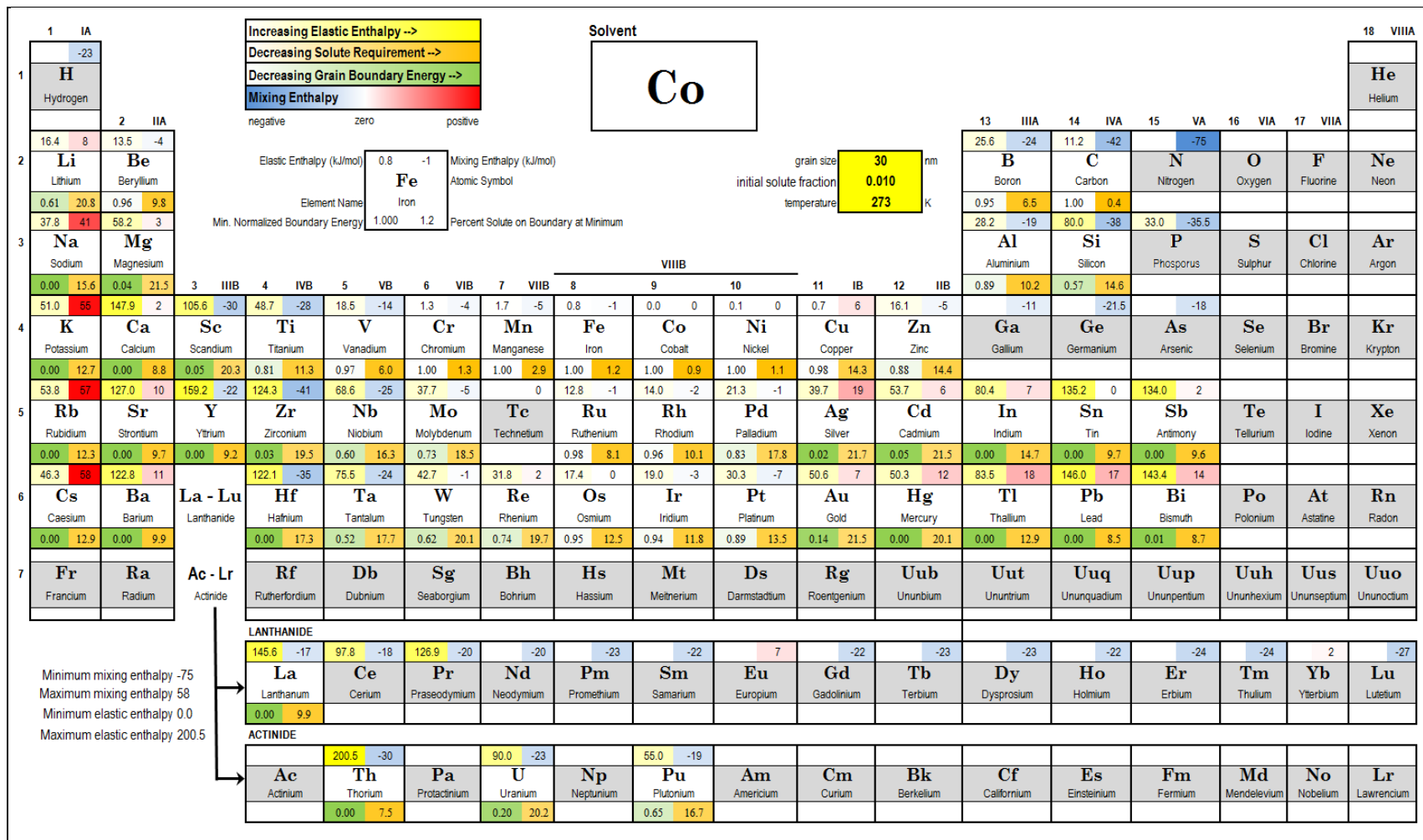


Figure A-15. Cobalt.

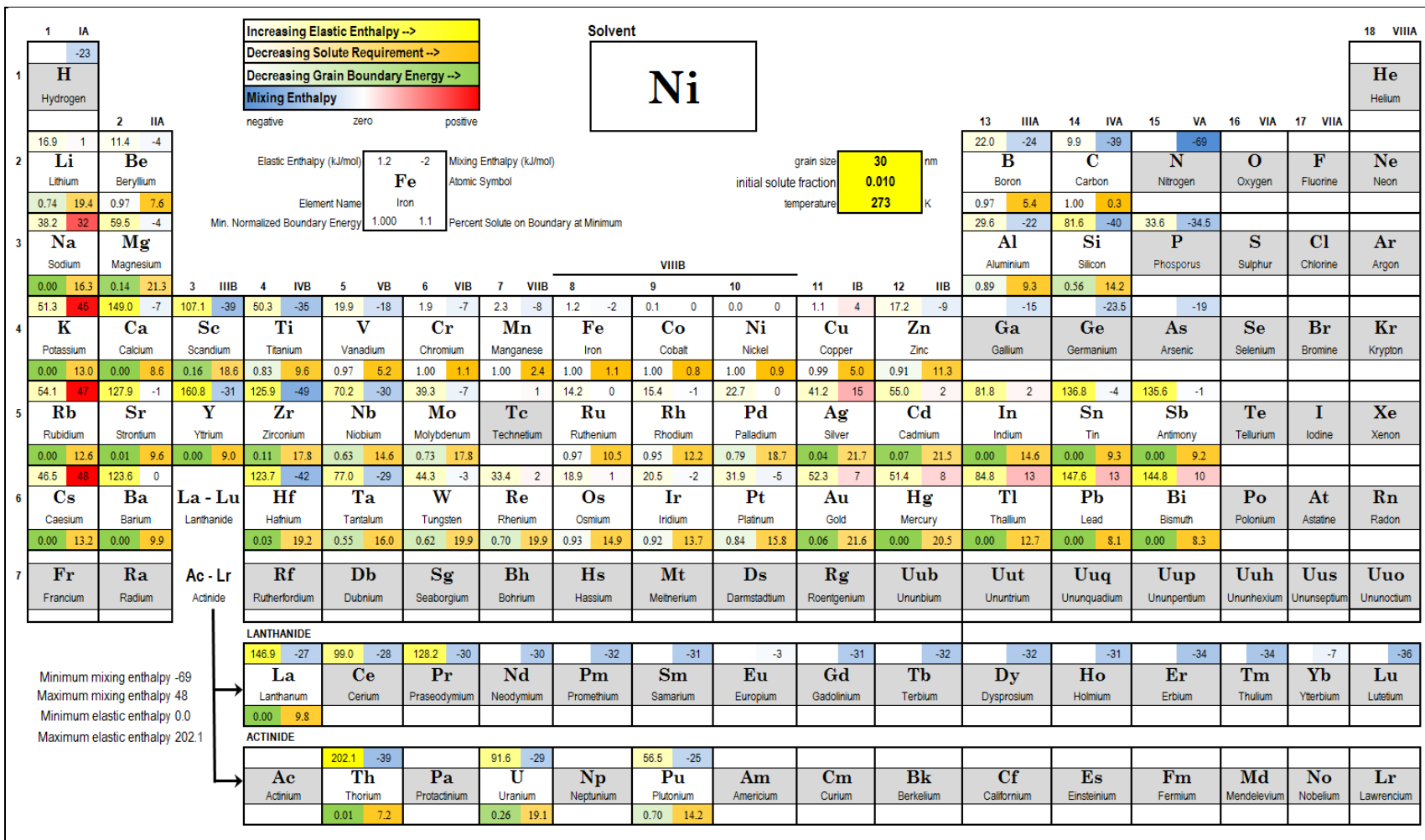


Figure A-16. Nickel.

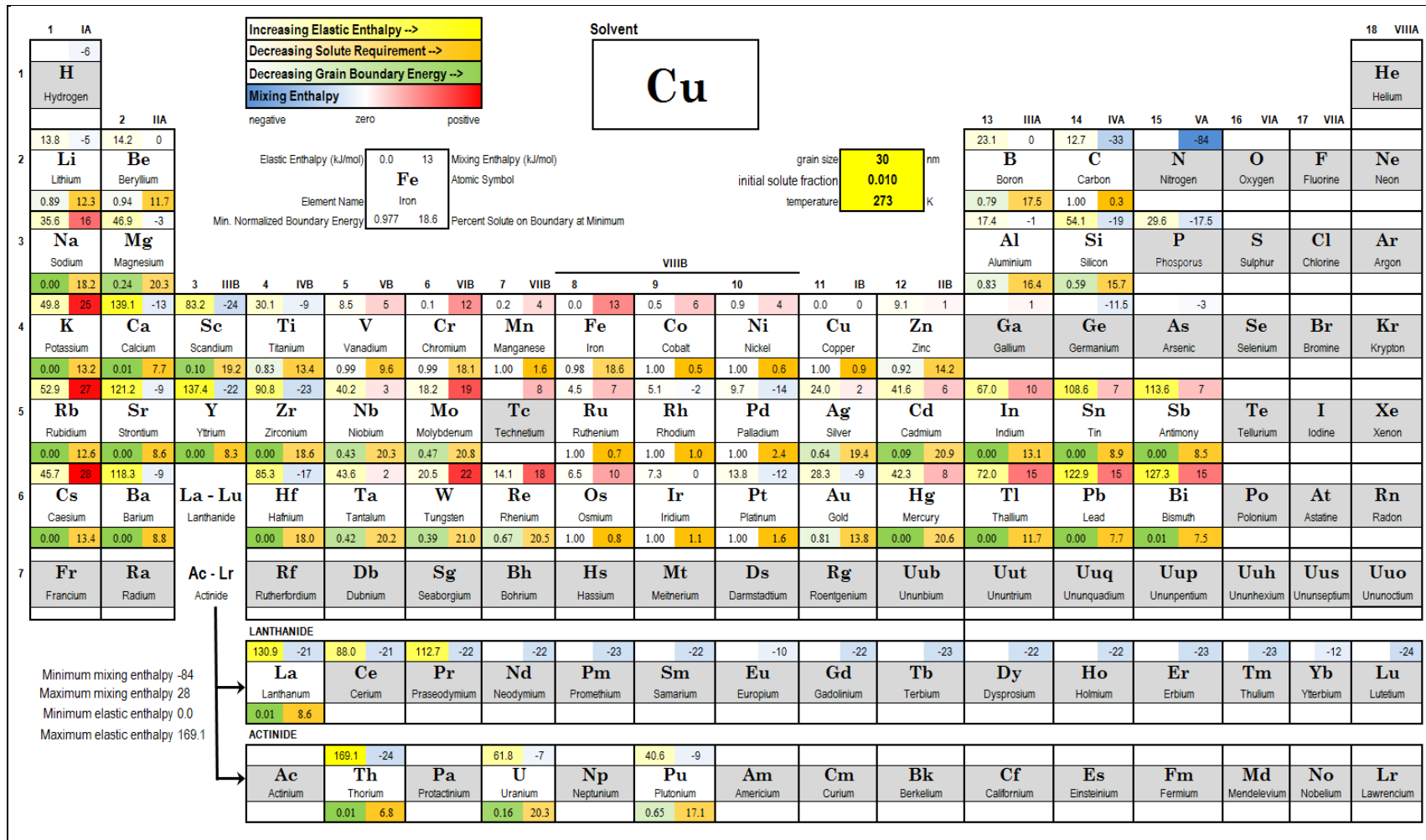


Figure A-17. Copper.

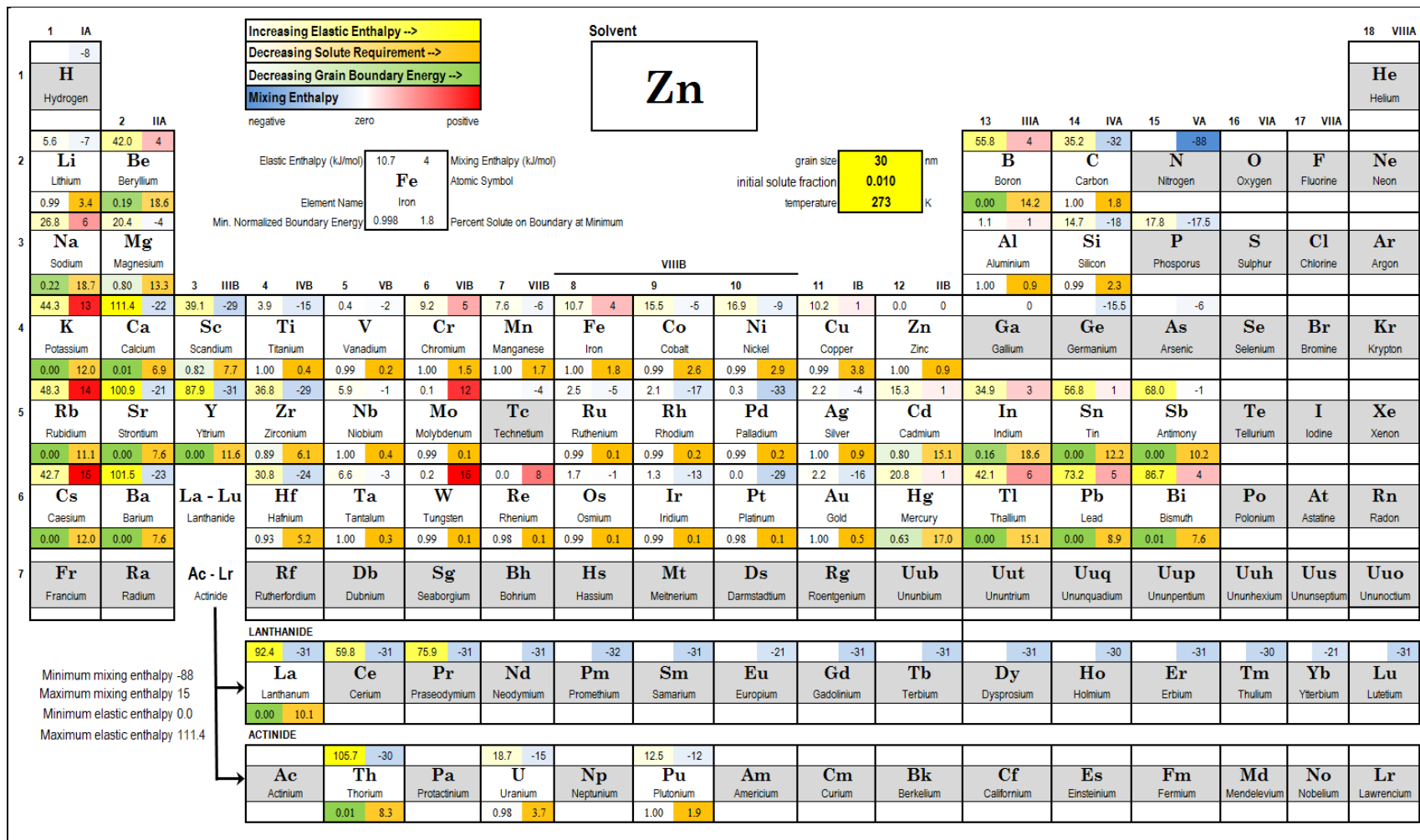


Figure A-18. Zinc.

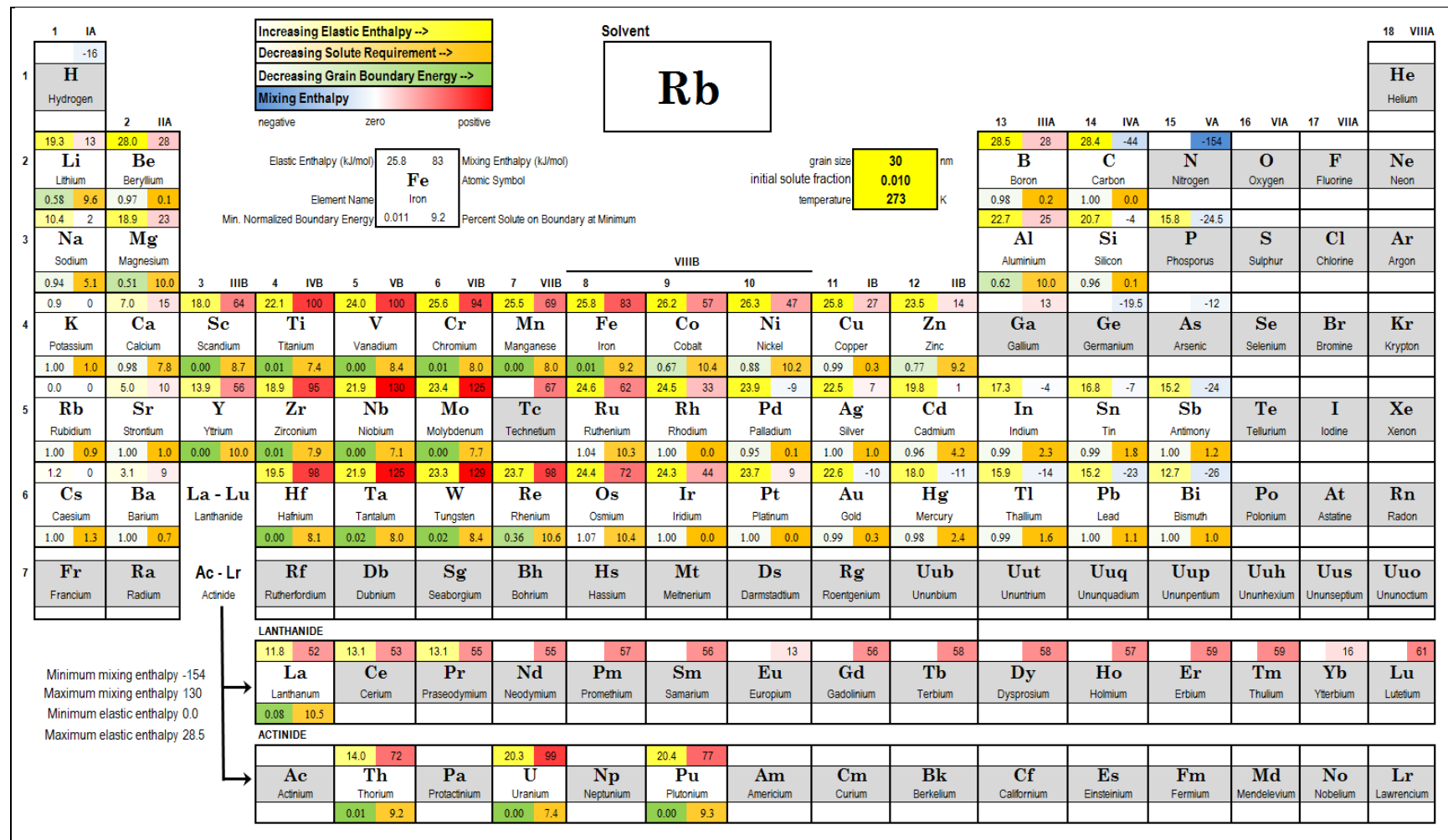


Figure A-19. Rubidium.

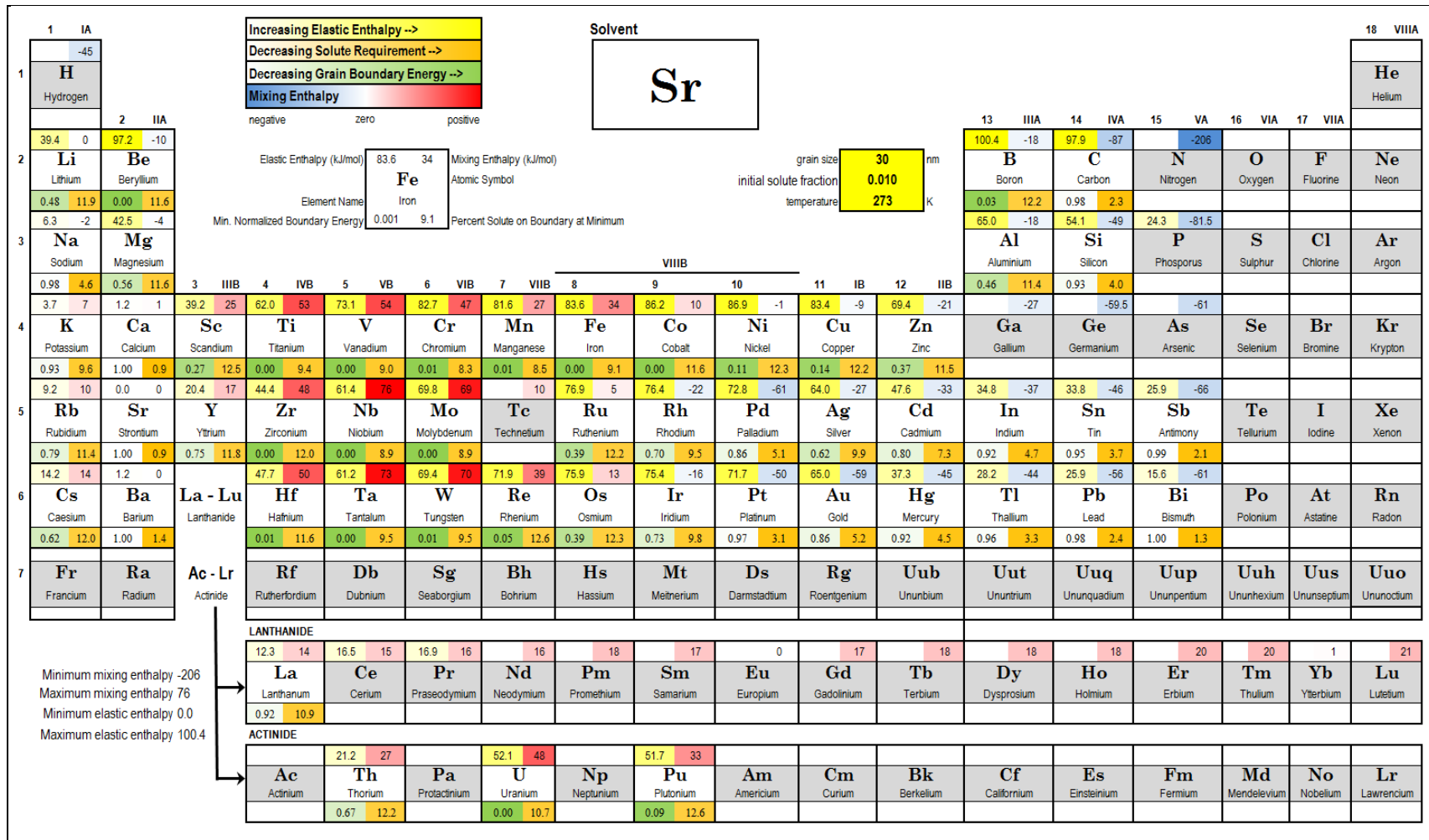


Figure A-20. Strontium.

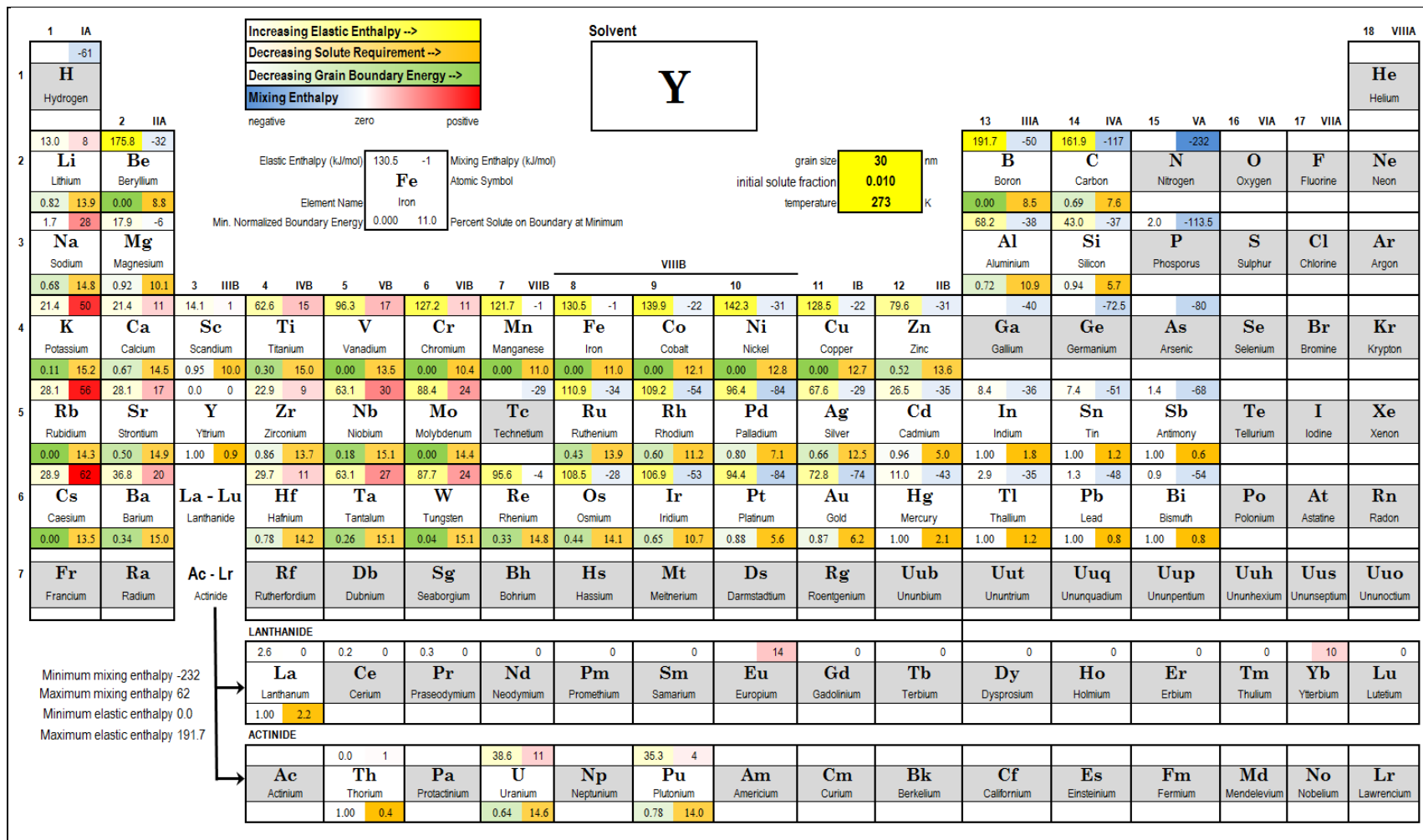


Figure A-21. Yttrium.

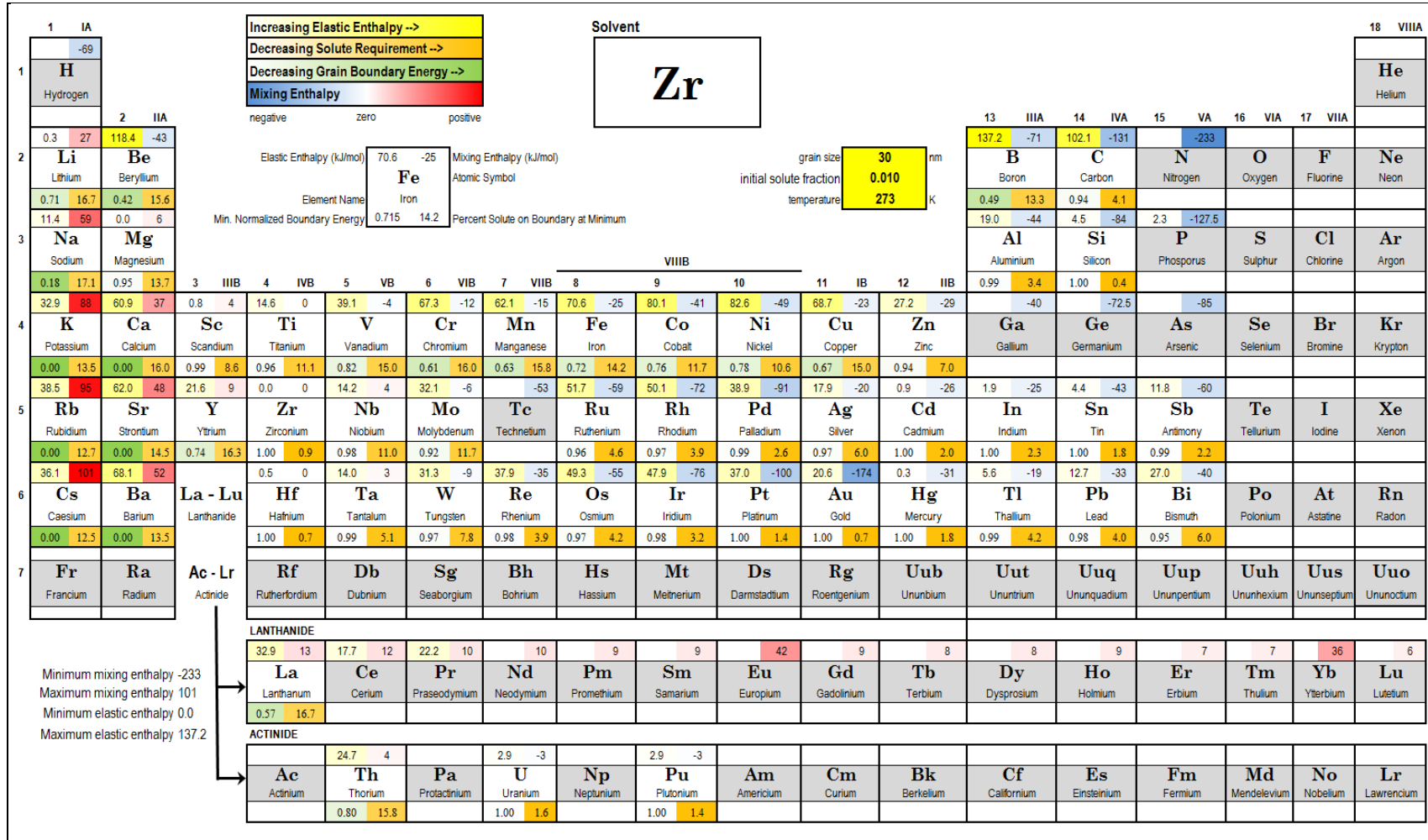


Figure A-22. Zirconium.

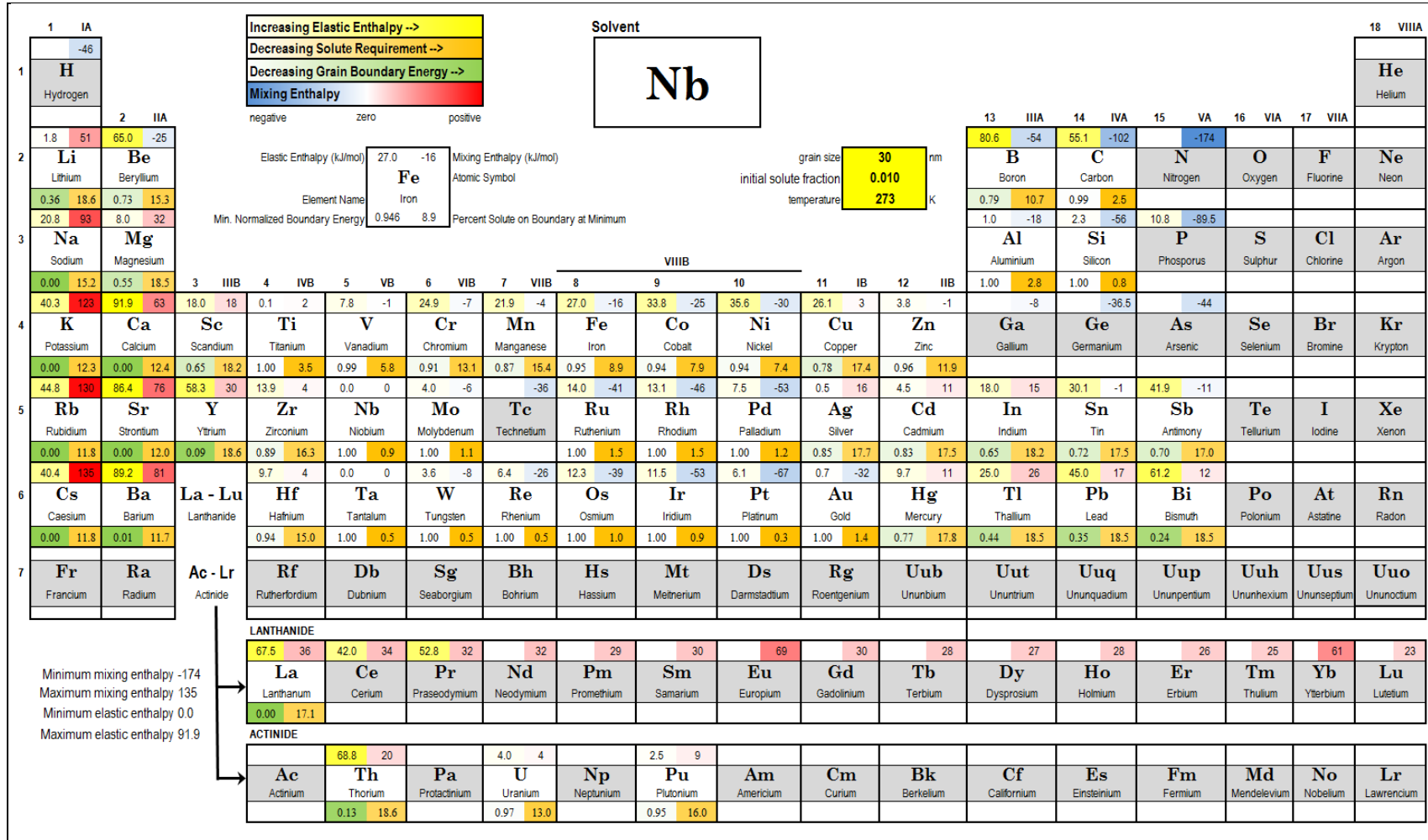


Figure A-23. Niobium.

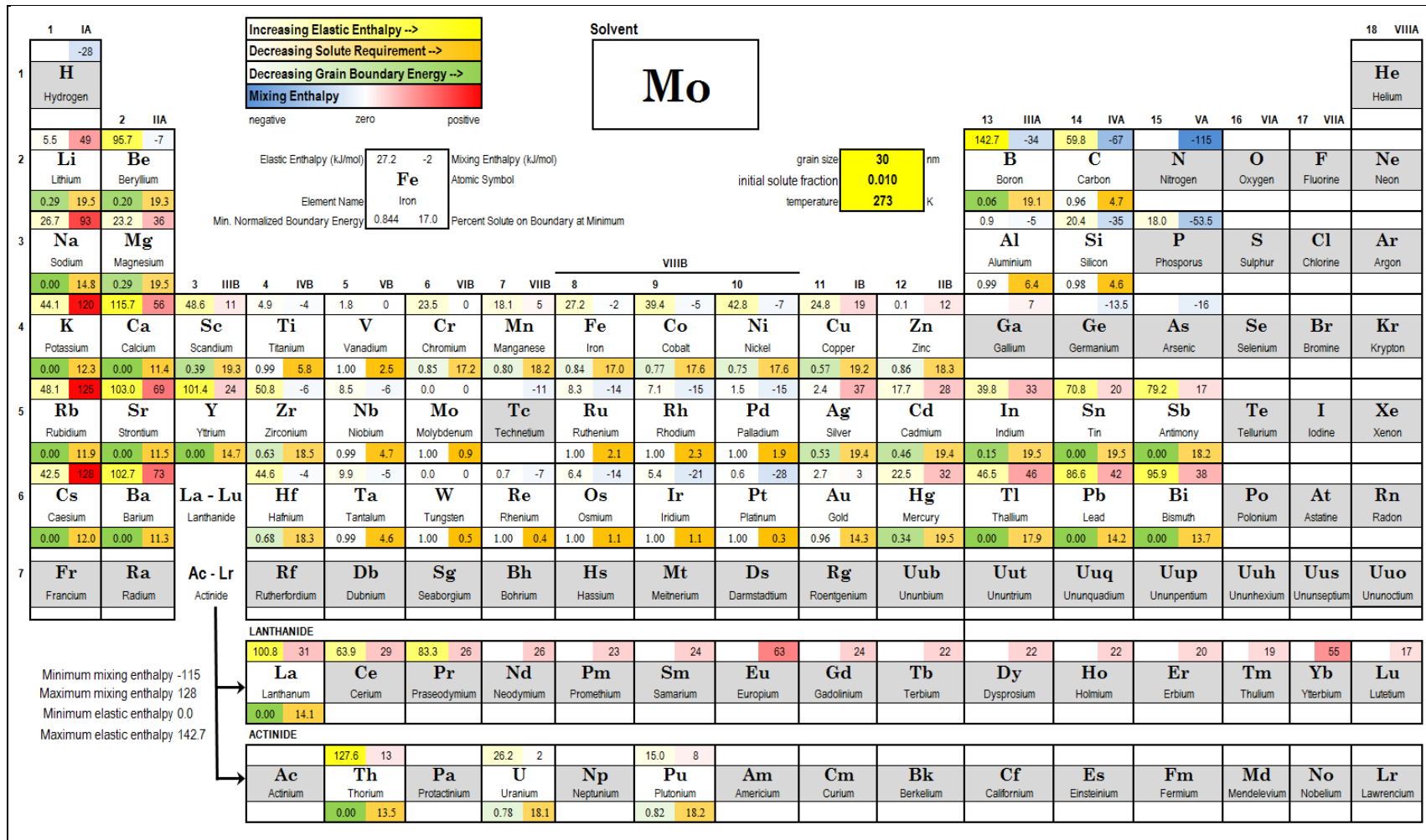


Figure A-24. Molybdenum.

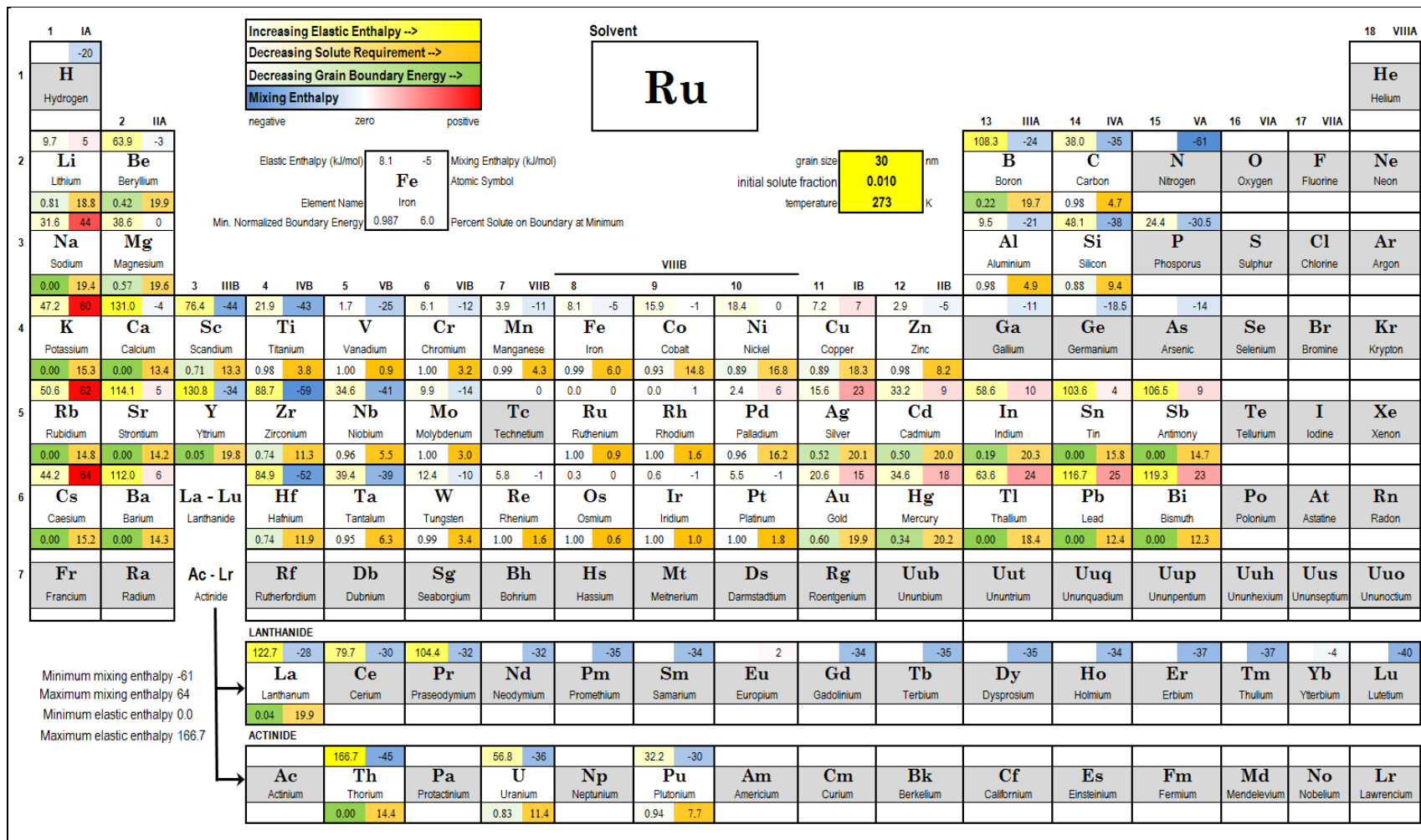


Figure A-25. Ruthenium.

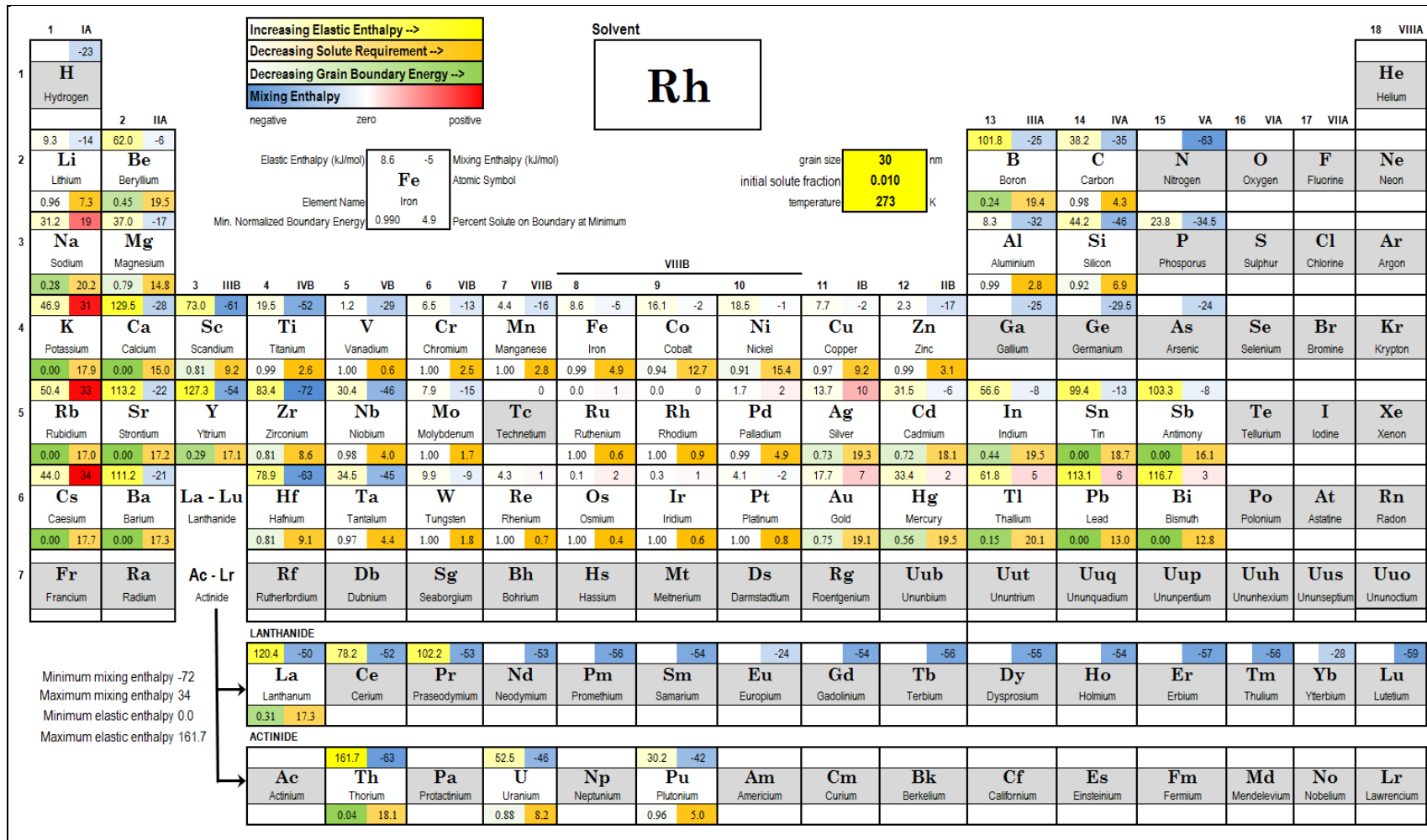
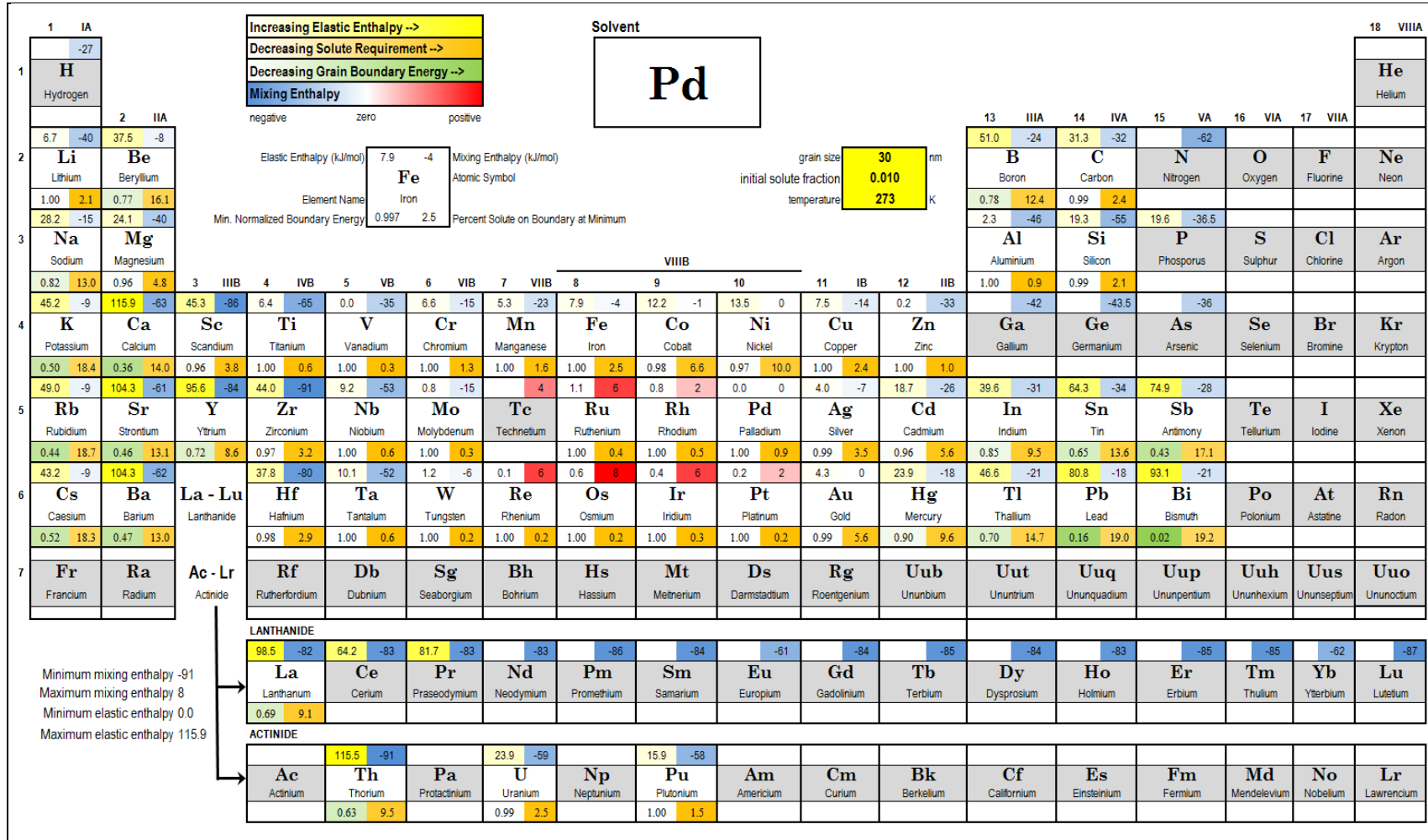


Figure A-26. Rhodium.



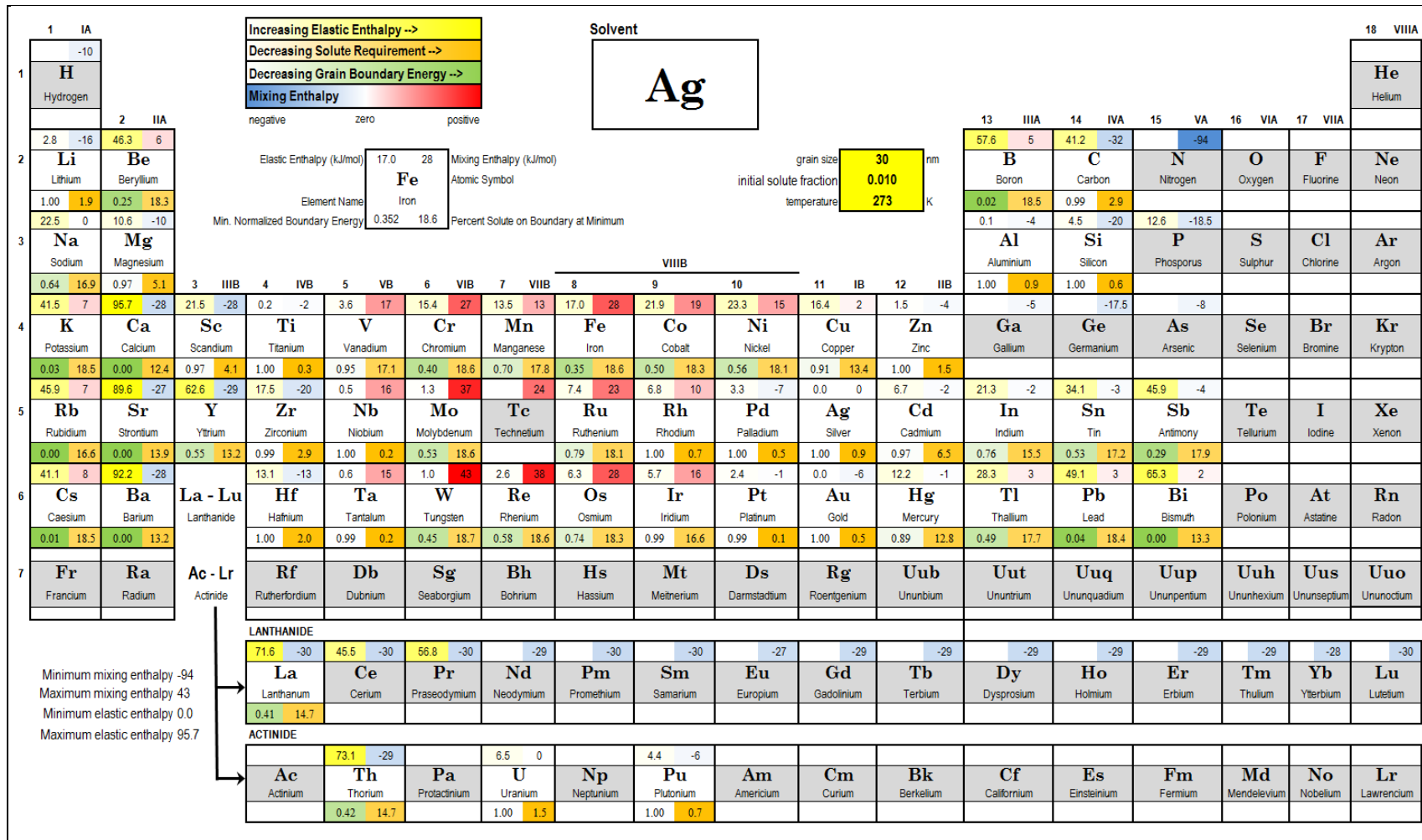


Figure A-28. Silver.

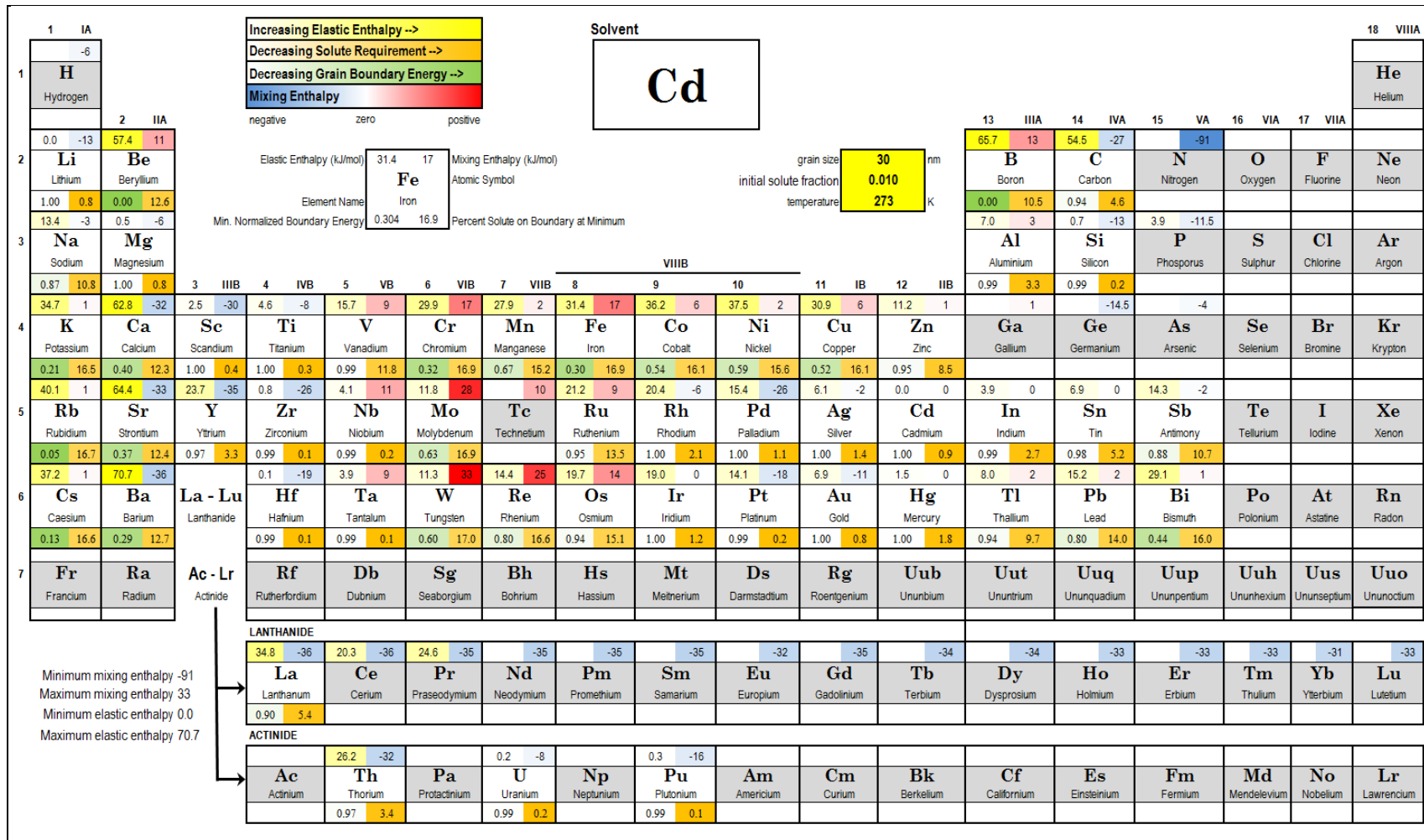


Figure A-29. Cadmium.

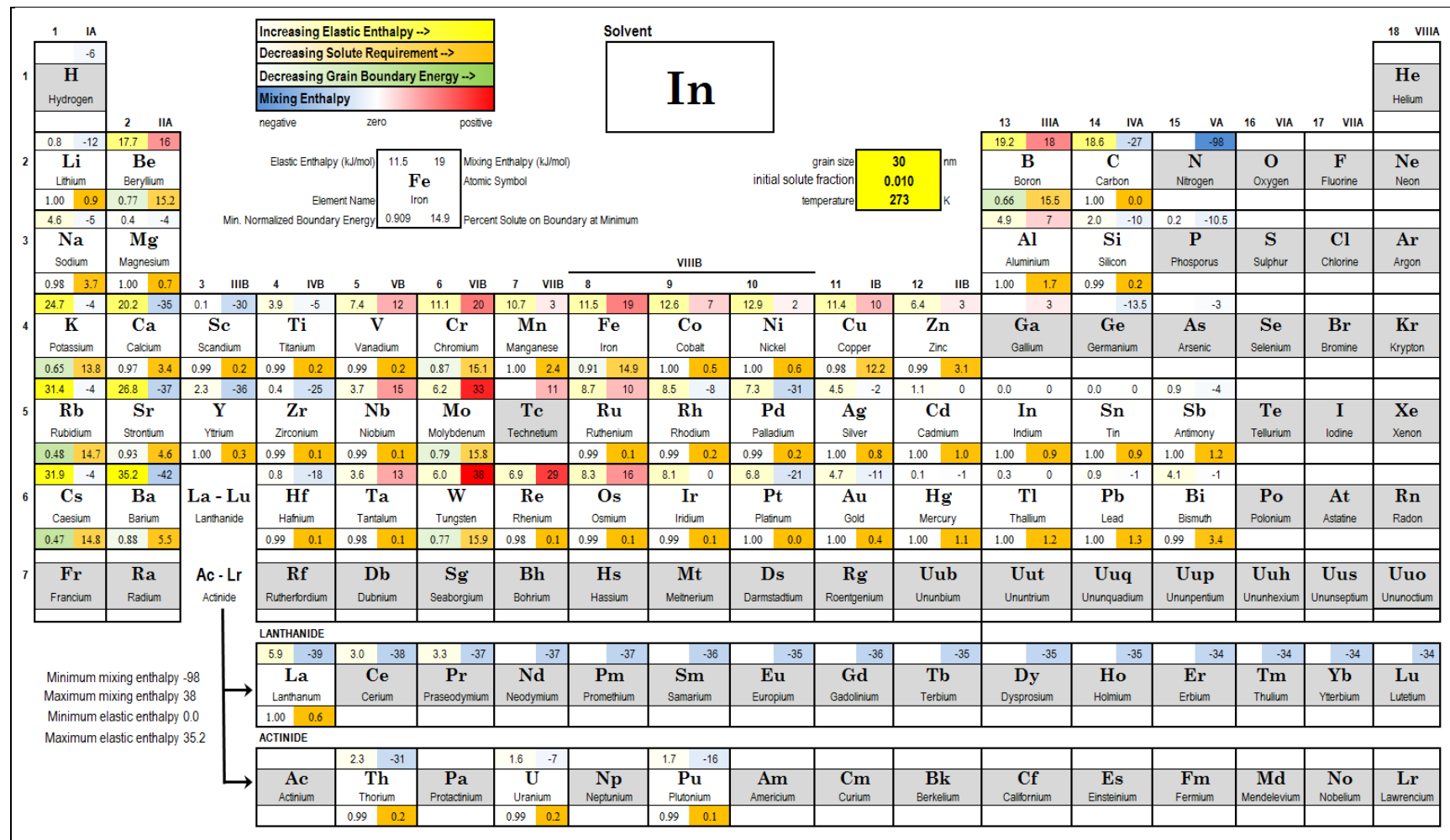


Figure A-30. Indium.

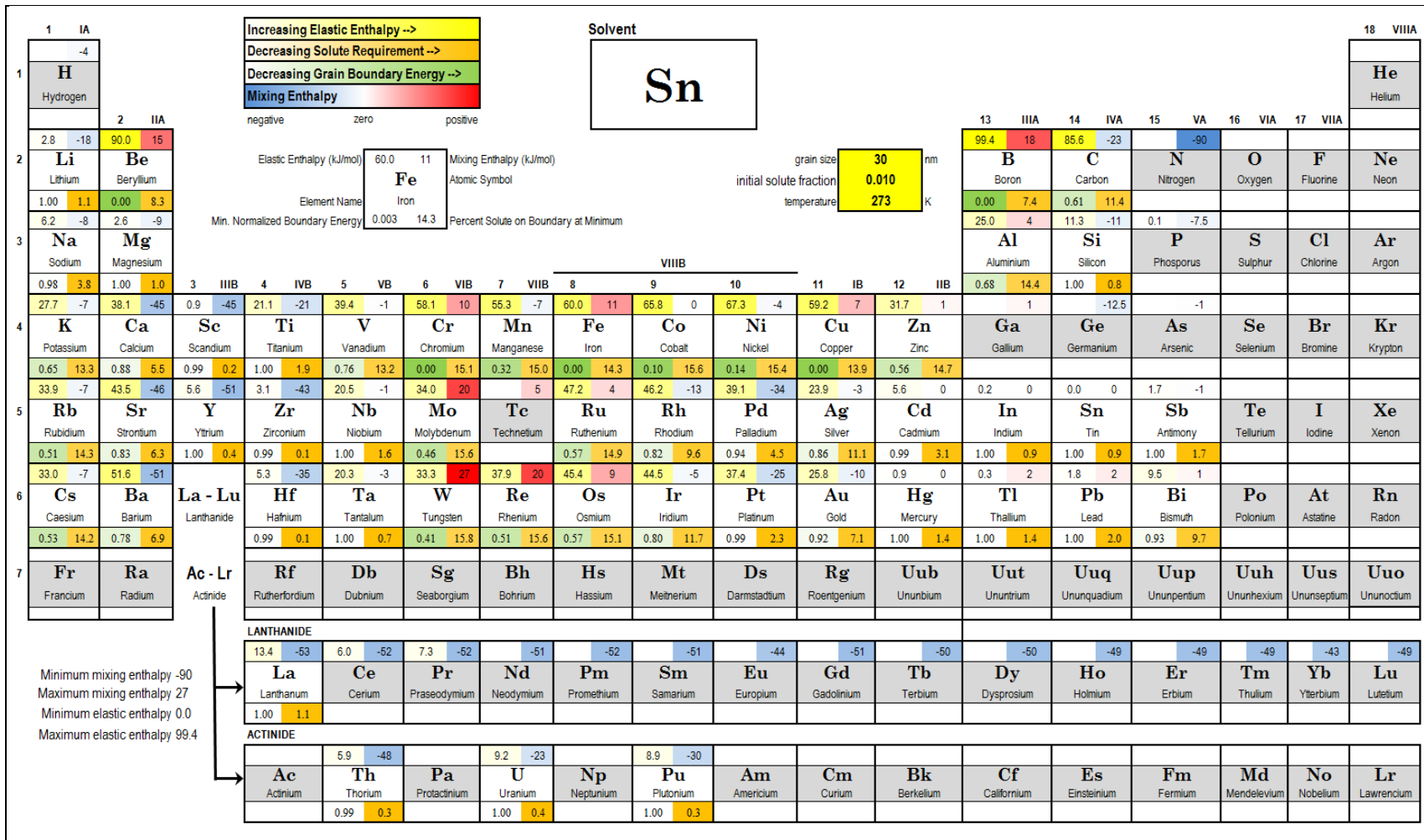


Figure A-31. Tin.

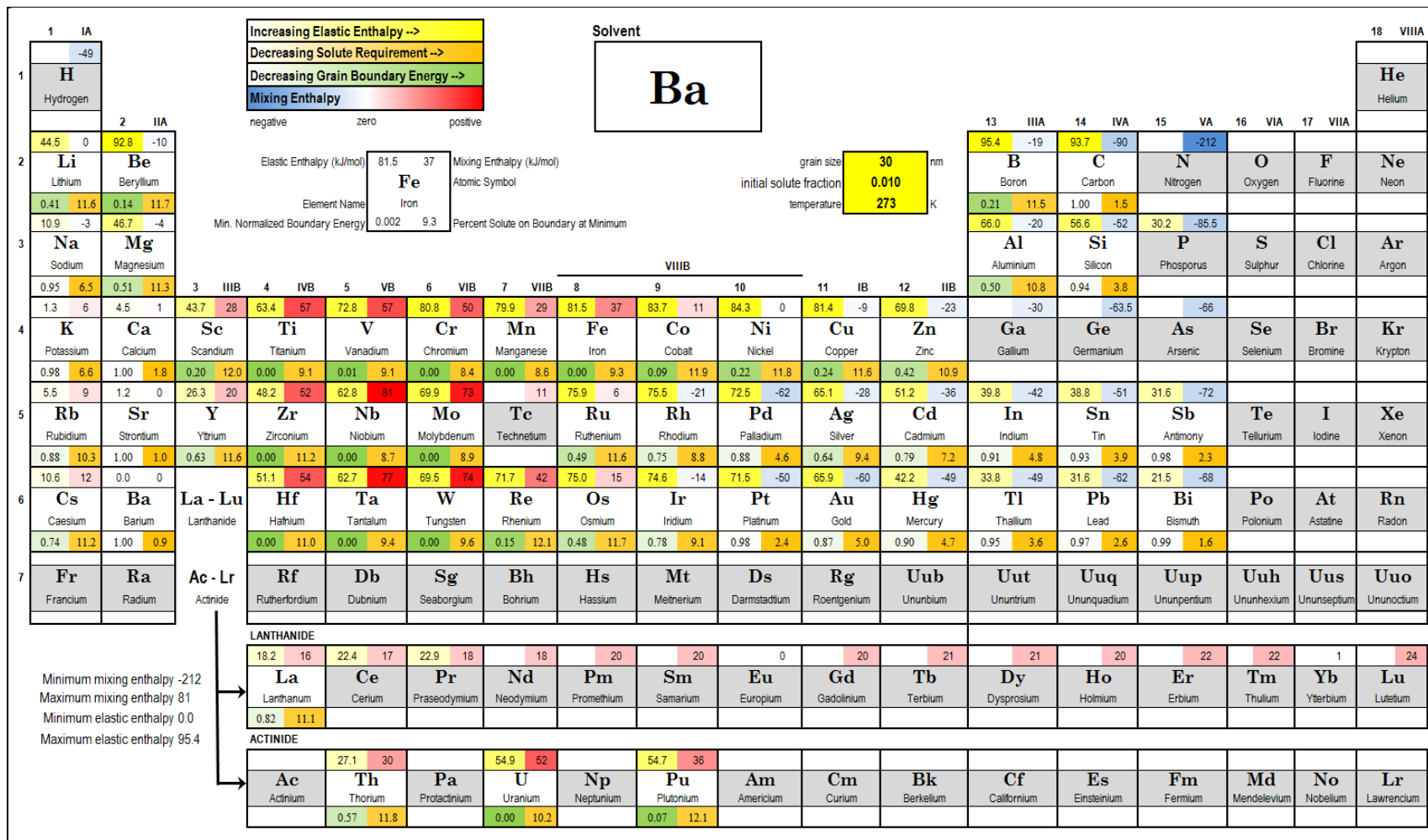


Figure A-32. Barium.

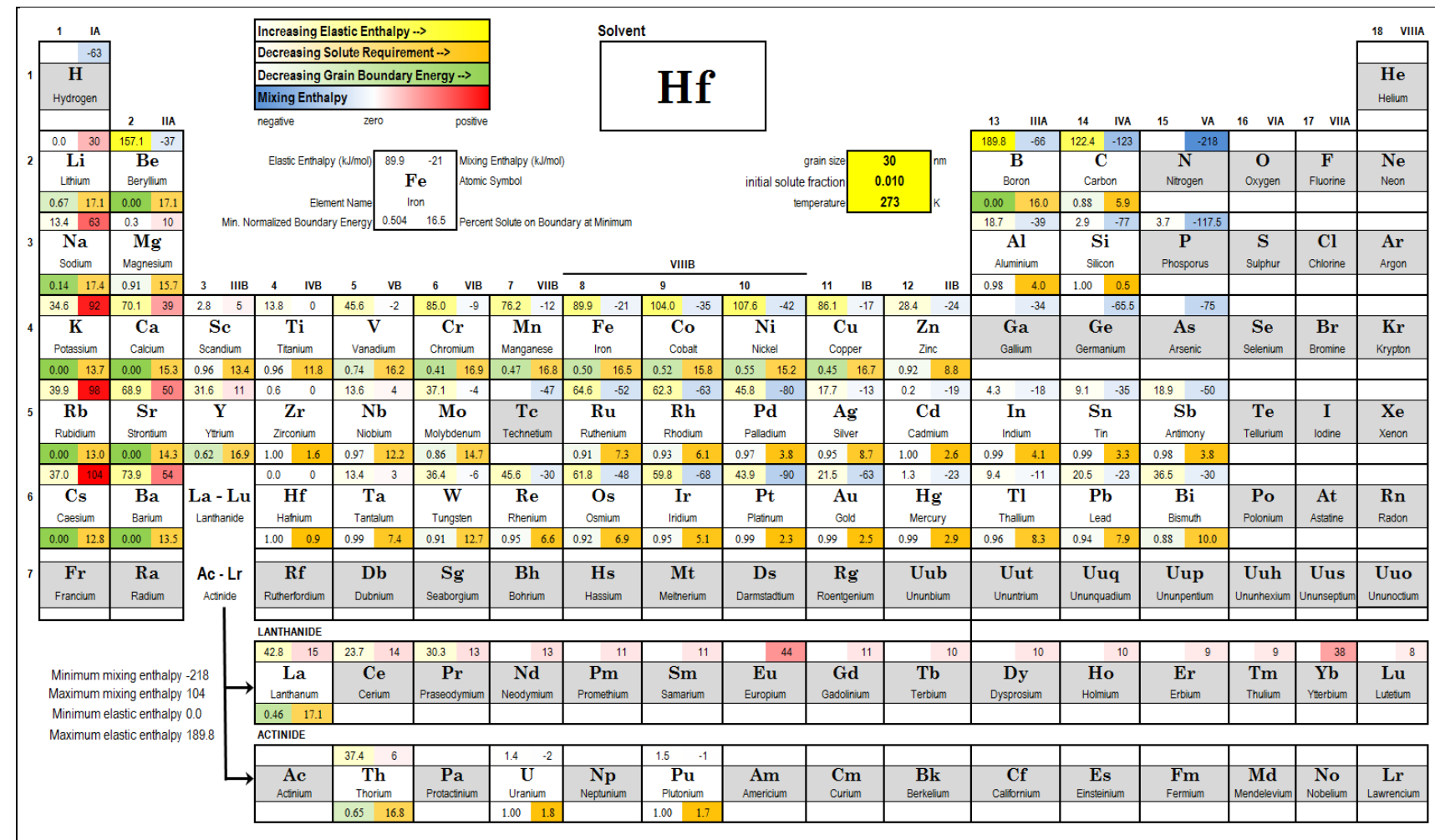


Figure A-33. Hafnium.

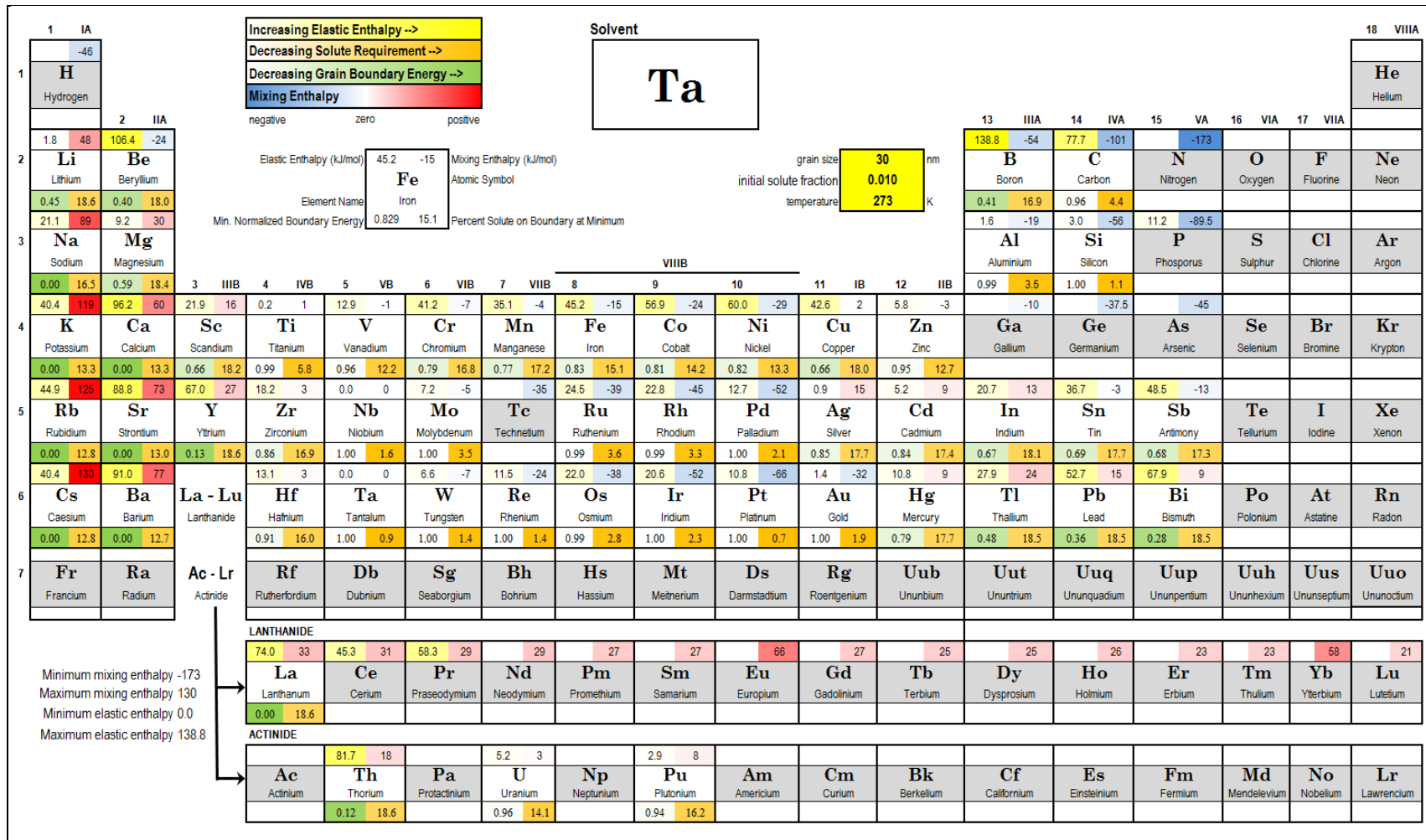


Figure A-34. Tantalum.

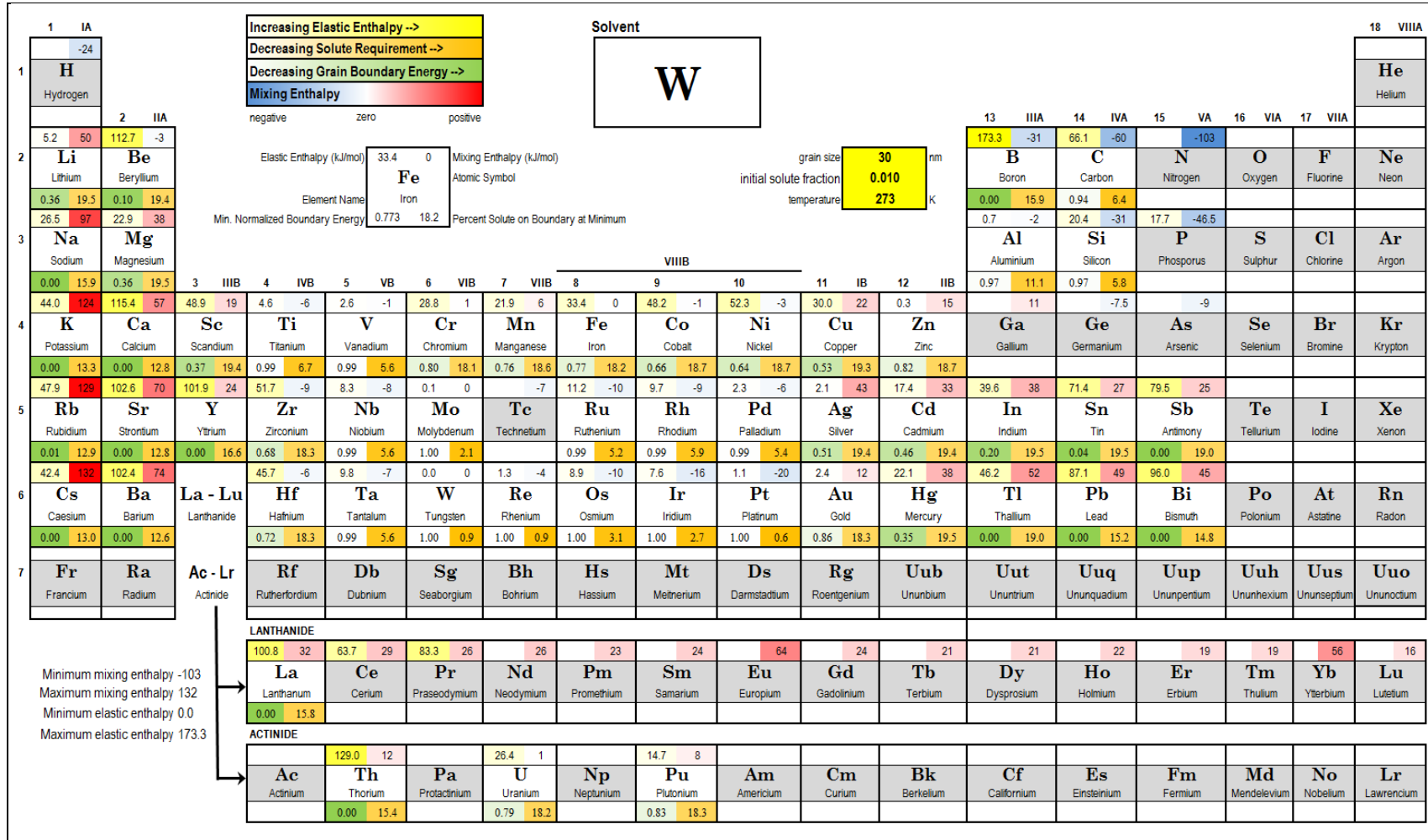


Figure A-35. Tungsten.

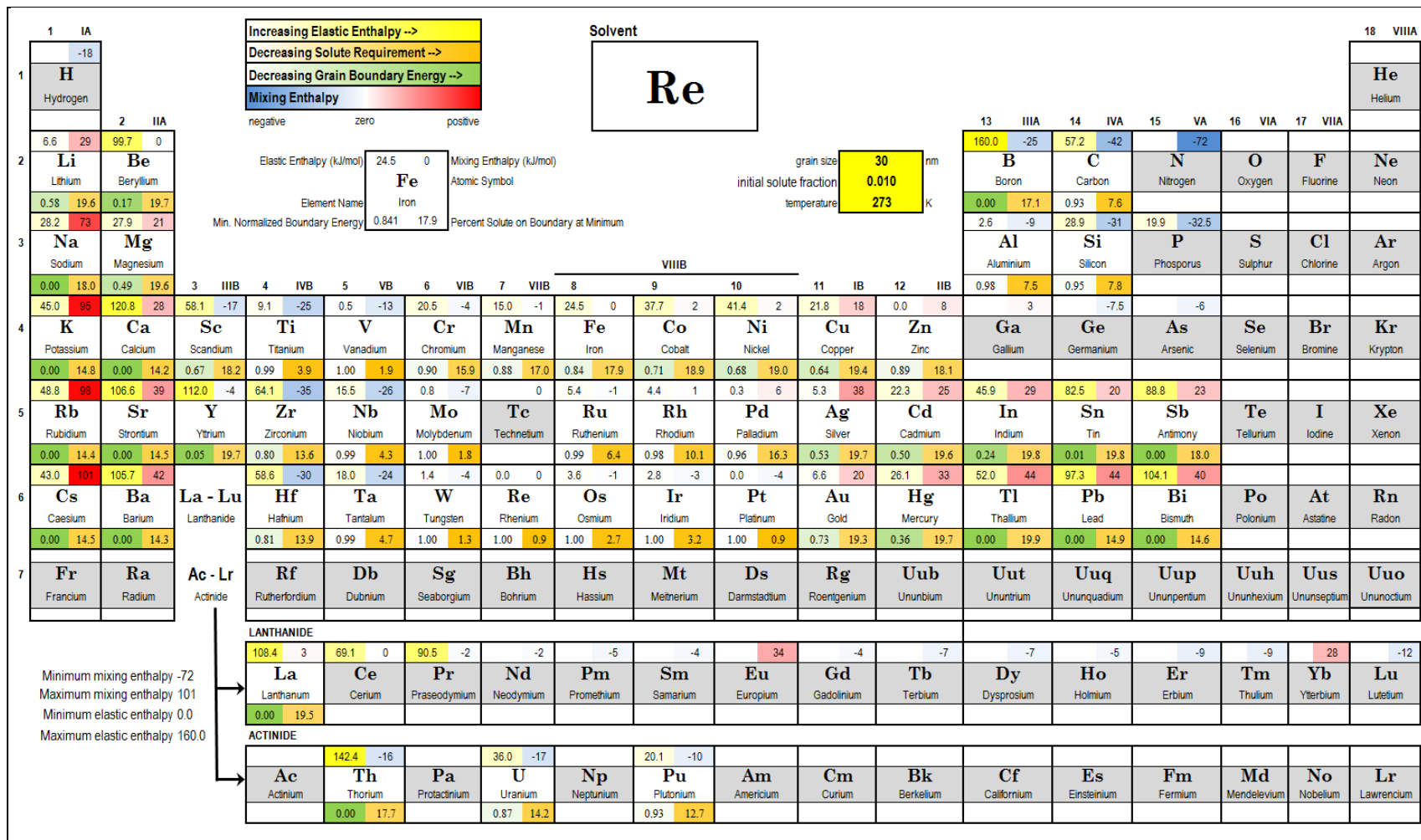


Figure A-36. Rhenium.

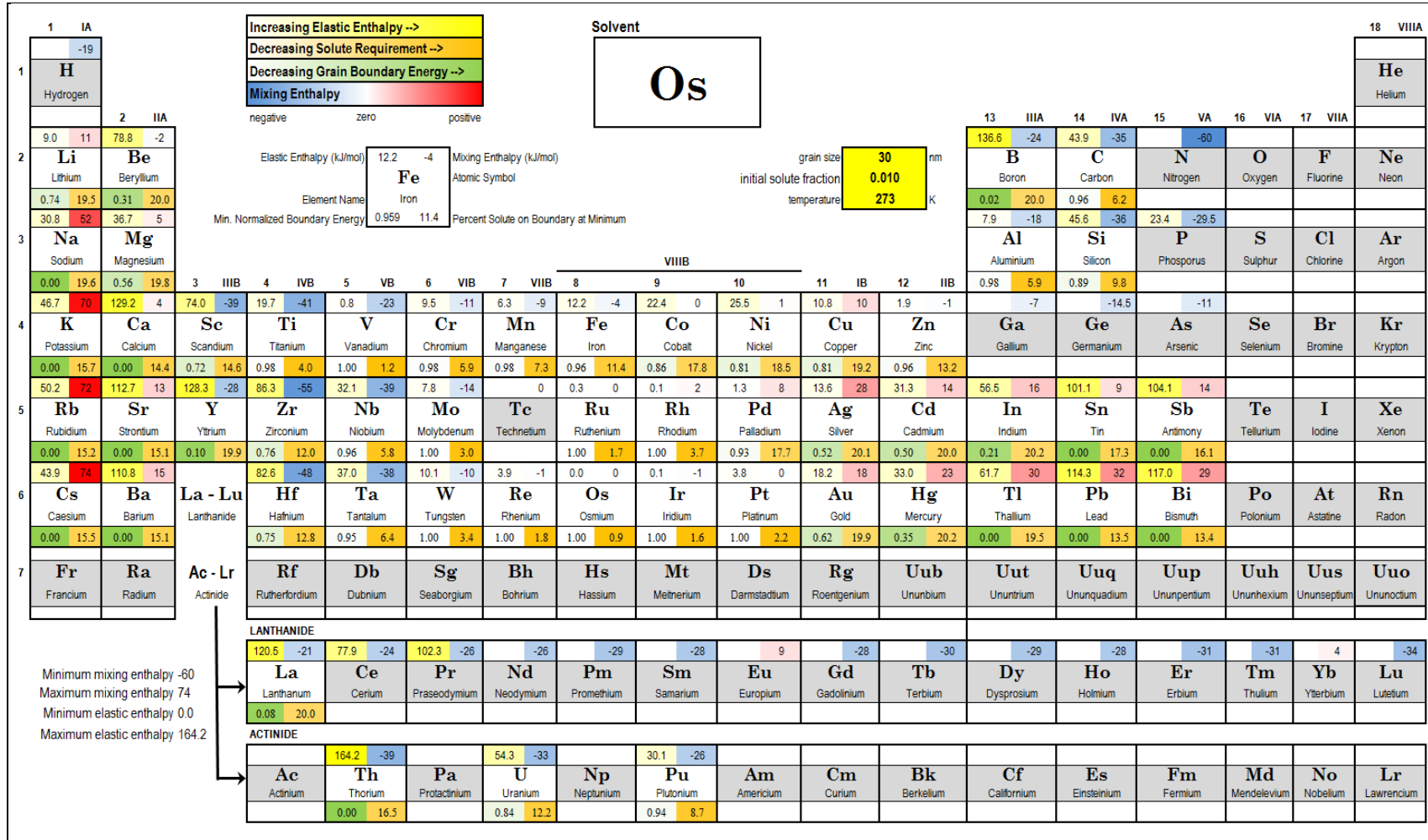


Figure A-37. Osmium.

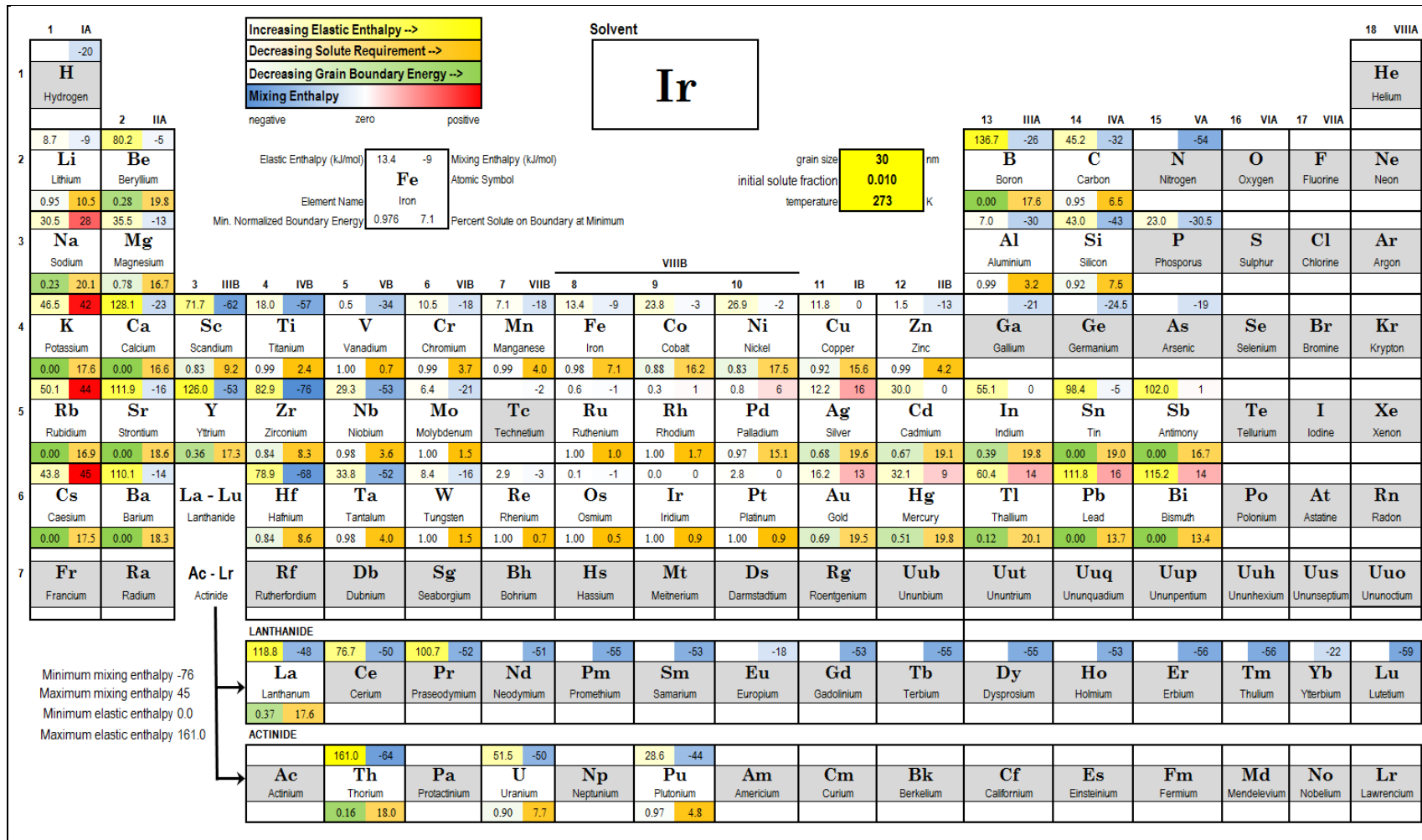


Figure A-38. Iridium.

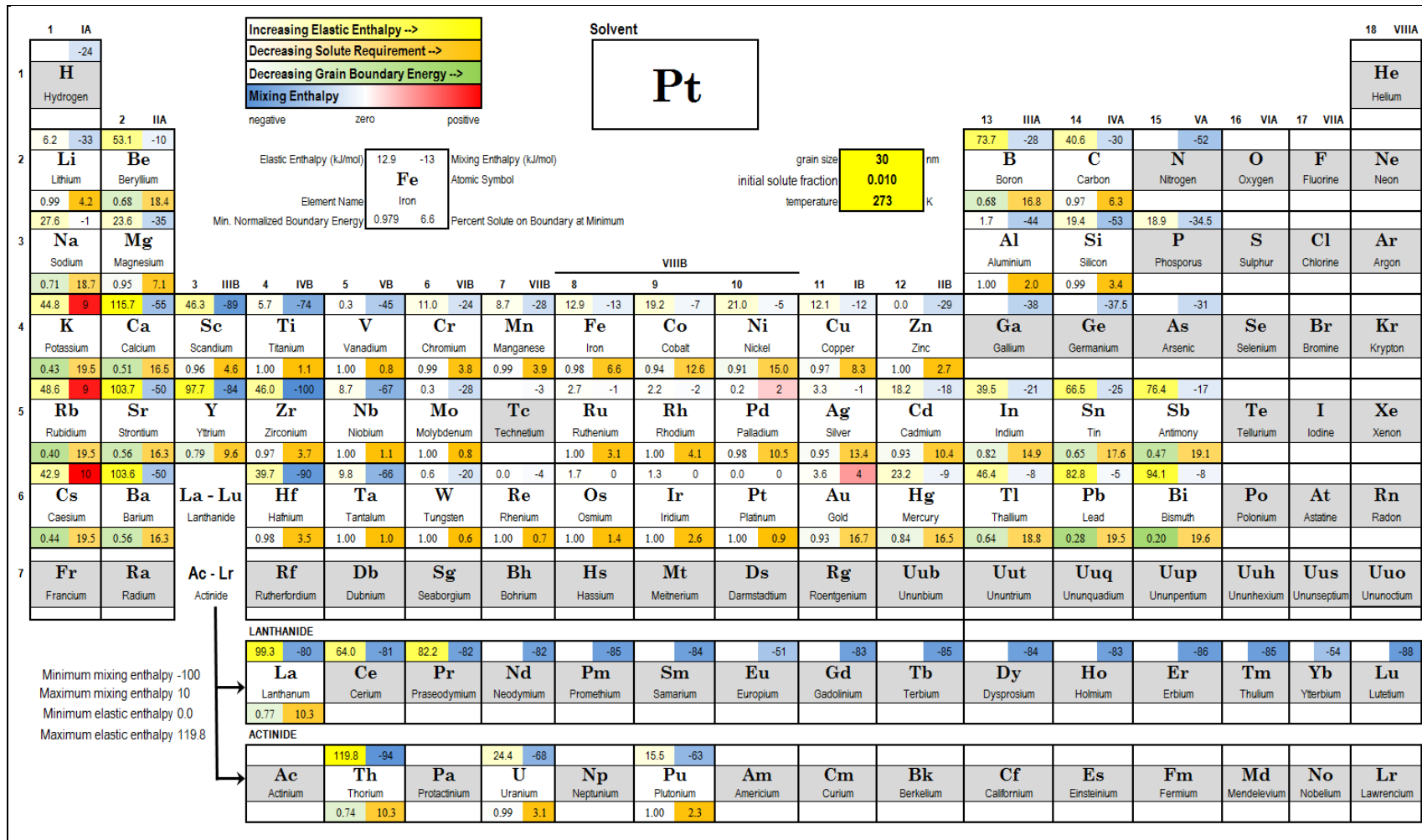


Figure A-39. Platinum.

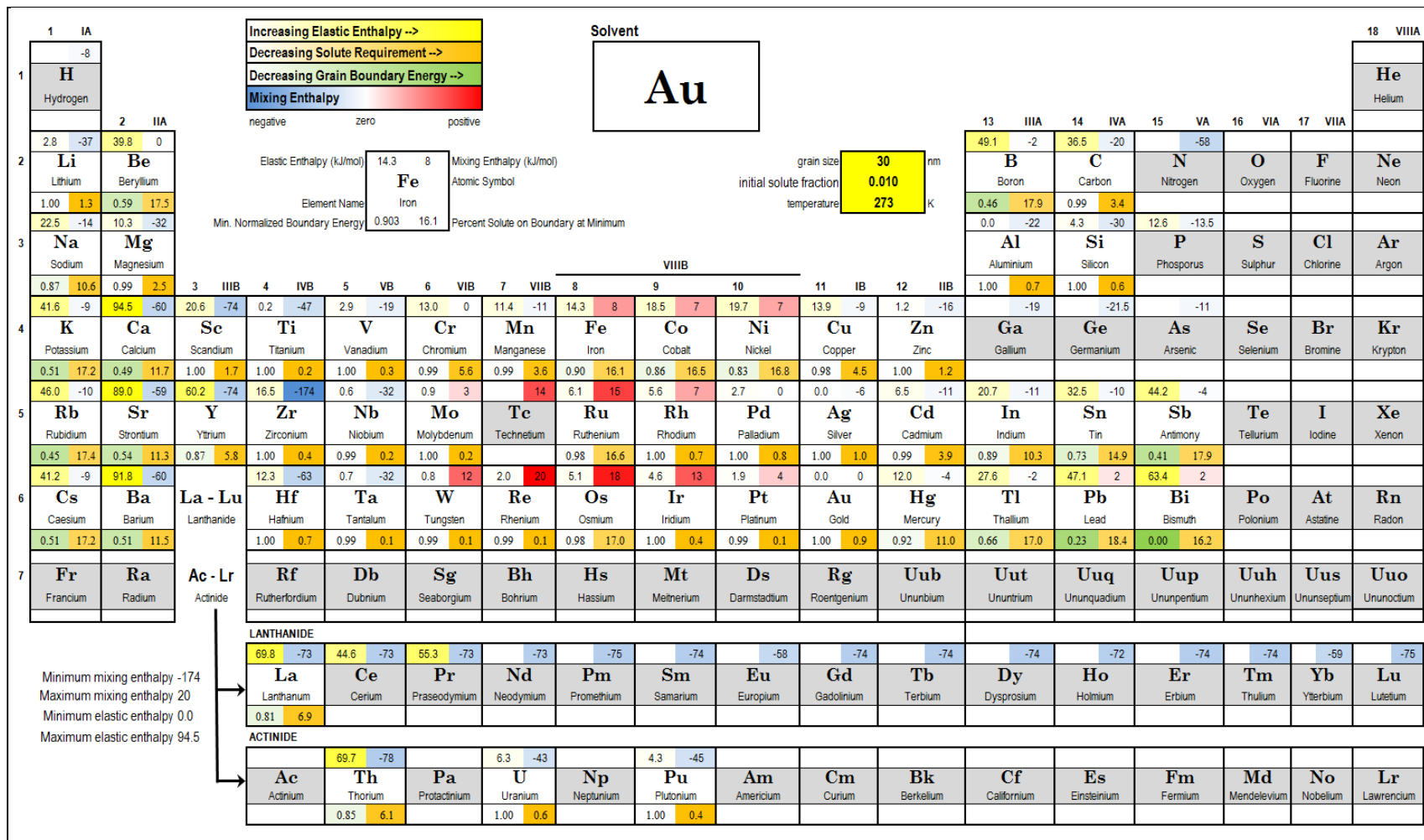


Figure A-40. Gold.

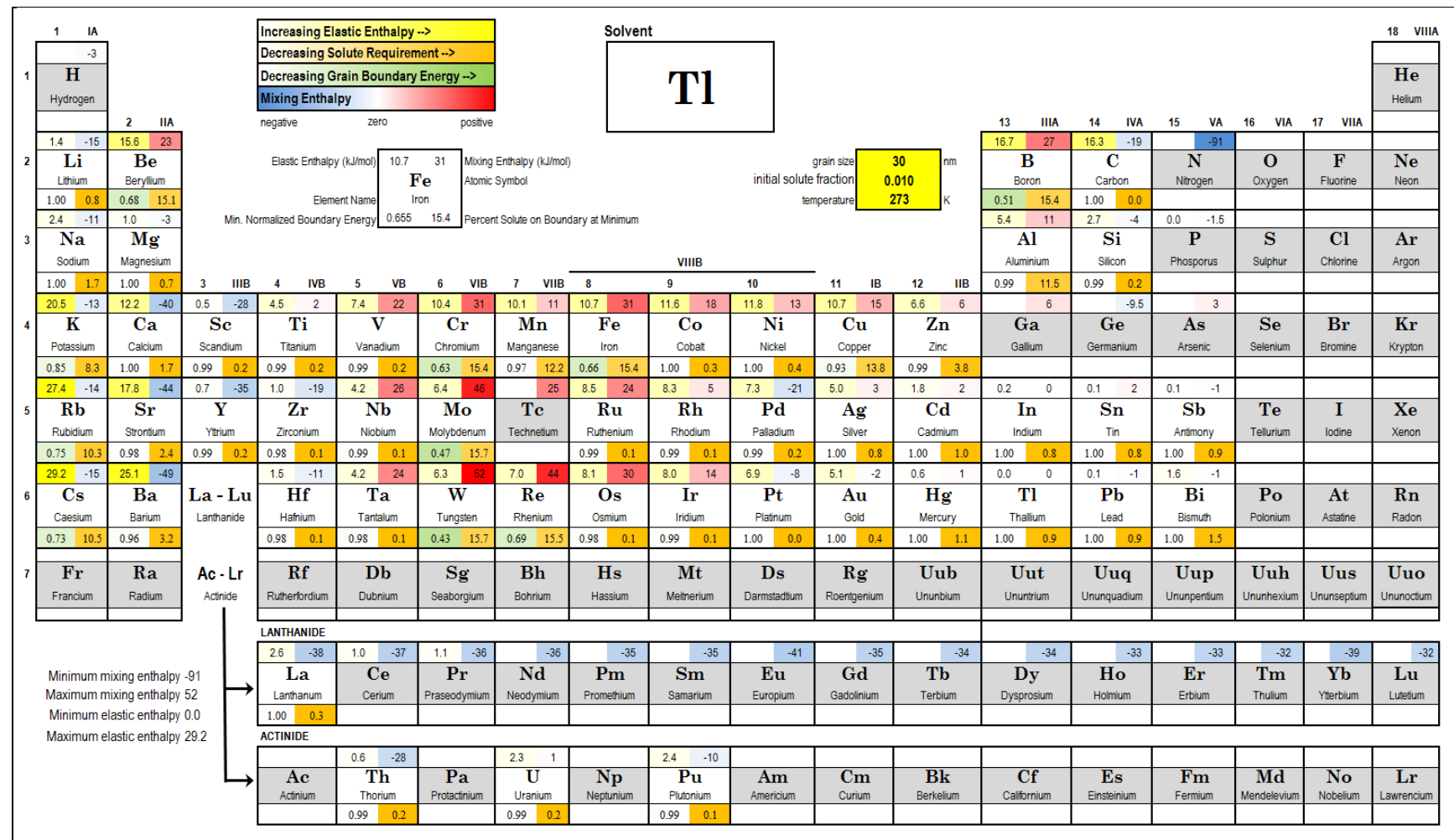


Figure A-41. Thallium.

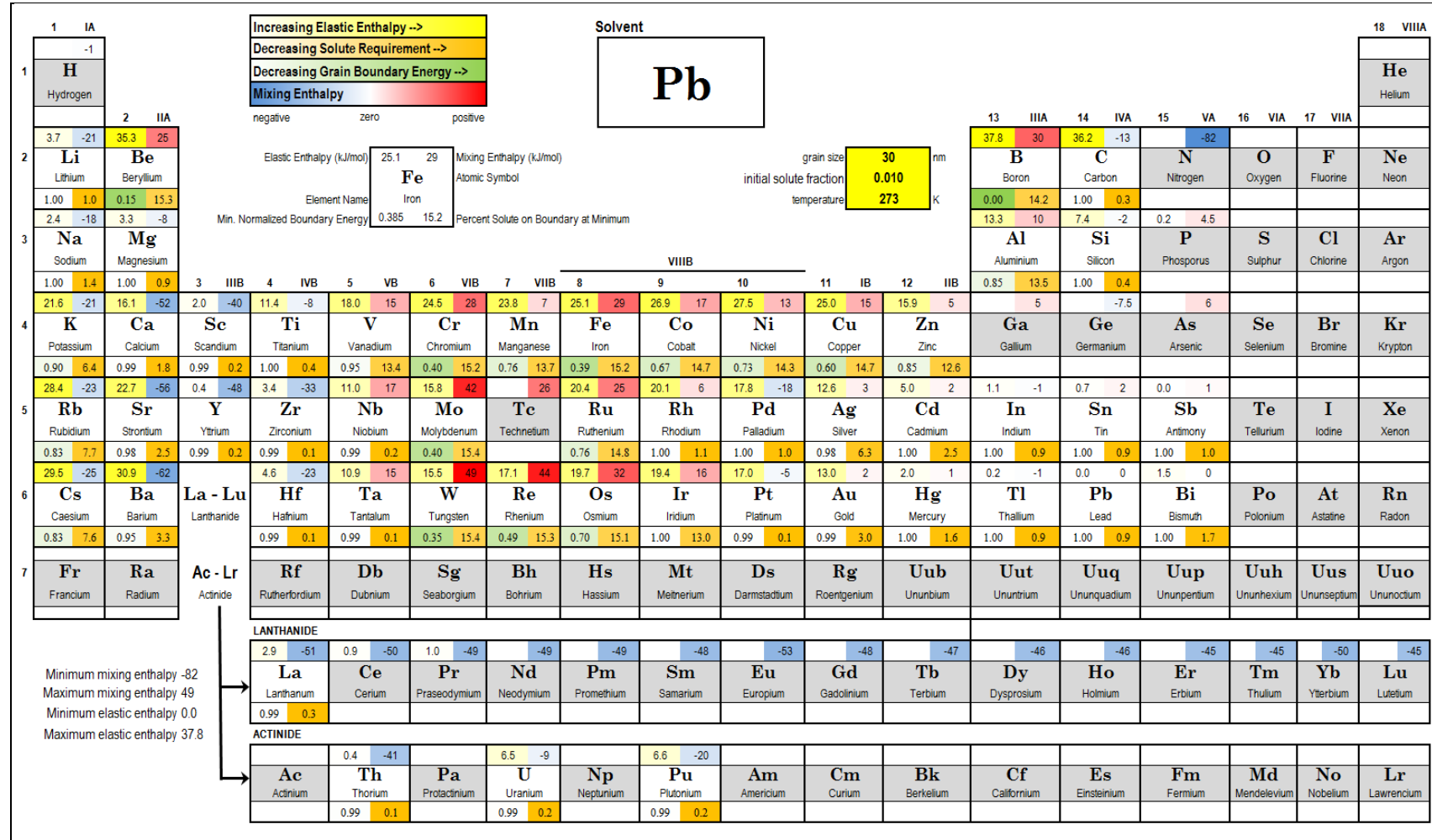
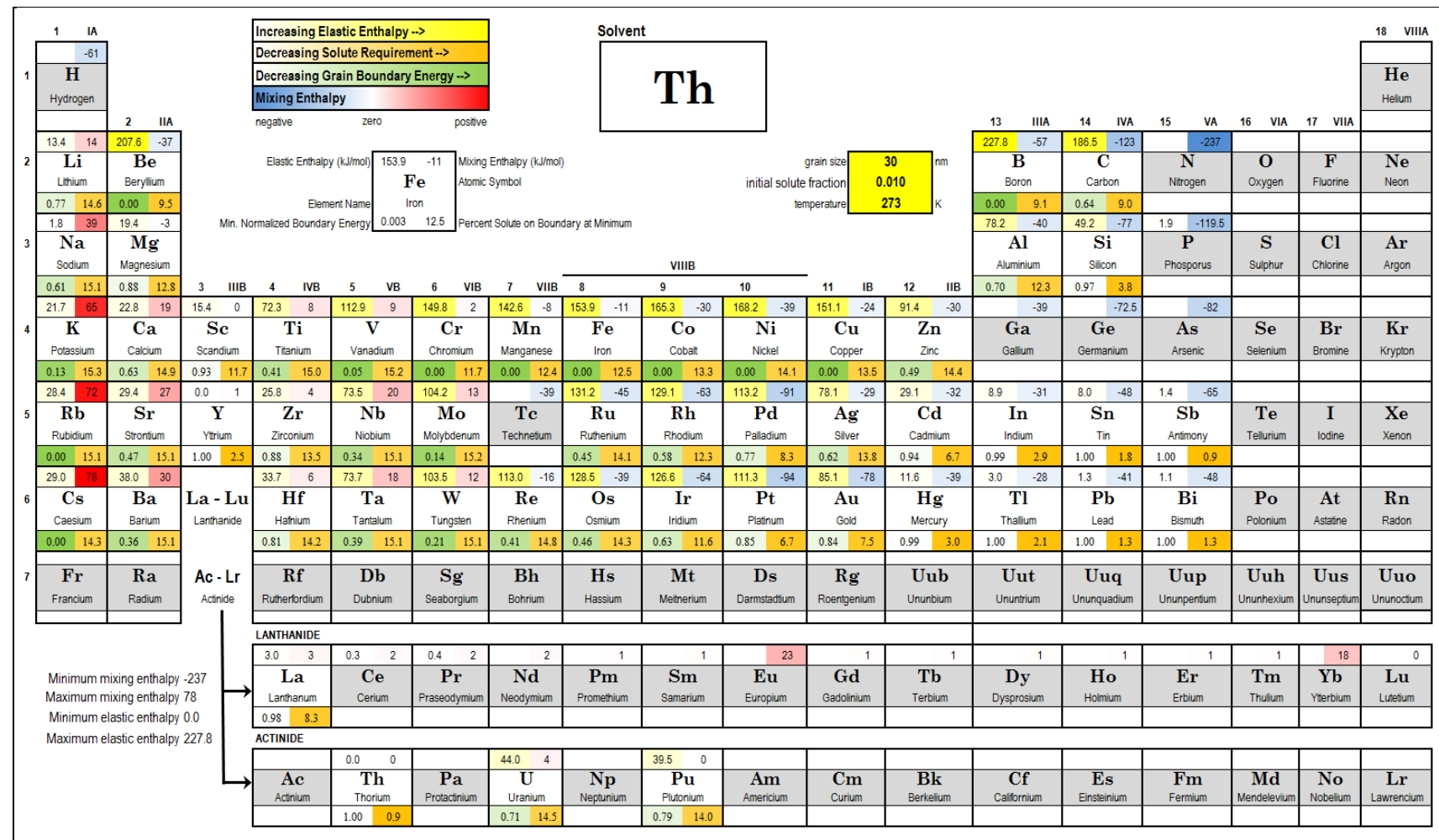


Figure A-42. Lead.



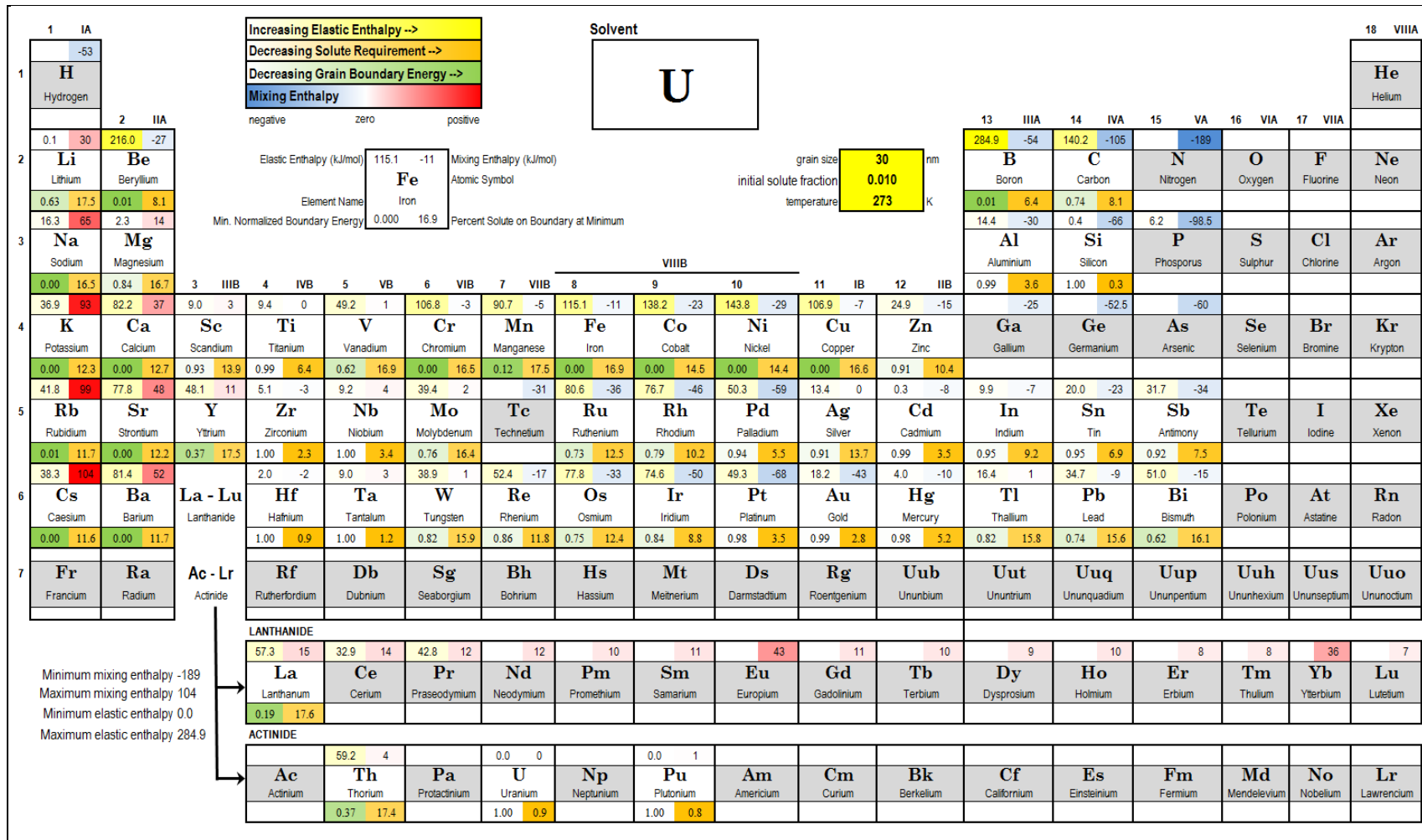


Figure A-44. Uranium.

List of Symbols, Abbreviations, and Acronyms

°C	degrees Celsius
Å	Angstrom
Al	aluminum
bcc	body-centered cubic
cm	centimeter
Co	cobalt
Cr	chromium
Cu	copper
fcc	face-centered cubic
Fe	iron
g	gram
GPa	gigapascal
hcp	hexagonal close-packed
Hf	hafnium
kJ	kilojoule
Mg	magnesium
mol	mole
Nb	niobium
Ni	nickel
Pb	lead
Pd	palladium
Sn	tin
Ta	tantalum
Ti	titanium

V vanadium

W tungsten

Zn zinc

Zr zirconium

NO. OF
COPIES ORGANIZATION

1 DEFENSE TECHNICAL
(PDF INFORMATION CTR
only) DTIC OCA
8725 JOHN J KINGMAN RD
STE 0944
FORT BELVOIR VA 22060-6218

1 DIRECTOR
US ARMY RESEARCH LAB
IMNE ALC HRR
2800 POWDER MILL RD
ADELPHI MD 20783-1197

1 DIRECTOR
US ARMY RESEARCH LAB
RDRL CIO LL
2800 POWDER MILL RD
ADELPHI MD 20783-1197

INTENTIONALLY LEFT BLANK.